

2013-04-04

Modular MRI Guided Device Development System: Development, Validation and Applications

Gregory Cole

Worcester Polytechnic Institute

Follow this and additional works at: <https://digitalcommons.wpi.edu/etd-dissertations>

Repository Citation

Cole, G. (2013). *Modular MRI Guided Device Development System: Development, Validation and Applications*. Retrieved from <https://digitalcommons.wpi.edu/etd-dissertations/91>

This dissertation is brought to you for free and open access by [Digital WPI](#). It has been accepted for inclusion in Doctoral Dissertations (All Dissertations, All Years) by an authorized administrator of Digital WPI. For more information, please contact wpi-etd@wpi.edu.

WORCESTER POLYTECHNIC INSTITUTE

DOCTORAL DISSERTATION

Modular MRI Guided Device Development System: Development, Validation and Applications

Author:

Gregory COLE

Supervisor:

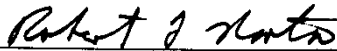
Dr. Gregory FISCHER

*A dissertation submitted in fulfillment of the requirements
for the degree of Doctor of Philosophy*

in the

Automation and Interventional Medicine Laboratory
Robotic Engineering Program

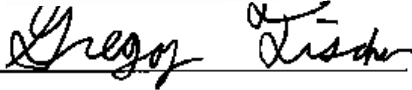
Dr. Robert Norton



Dr. Julie Pilitsis



Dr. Gregory Fischer



Dr. Michael Gennert

Dr. Michael Gennert, Program Head



Date:

4/4/2013

March 2013

“The best years of your life are the ones in which you decide your problems are your own. You do not blame them on your mother, the ecology, or the president. You realize that you control your own destiny.”

Albert Ellis

Abstract

Robotic Engineering Program

Doctor of Philosophy

by Gregory COLE

Since the first robotic surgical intervention was performed in 1985 using a PUMA industrial manipulator, development in the field of surgical robotics has been relatively fast paced, despite the tremendous costs involved in developing new robotic interventional devices. This is due to the clear advantages to augmented a clinicians skill and dexterity with the precision and reliability of computer controlled motion. A natural extension of robotic surgical intervention is the integration of image guided interventions, which give the promise of reduced trauma, procedure time and inaccuracies. Despite magnetic resonance imaging (MRI) being one of the most effective imaging modalities for visualizing soft tissue structures within the body, MRI guided surgical robotics has been frustrated by the high magnetic field in the MRI image space and the extreme sensitivity to electromagnetic interference.

The primary contributions of this dissertation relate to enabling the use of direct, live MR imaging to guide and assist interventional procedures. These are the two focus areas: creation both of an integrated MRI-guided development platform and of a stereotactic neural intervention system. The integrated series of modules of the development platform represent a significant advancement in the practice of creating MRI guided mechatronic devices, as well as an understanding of design requirements for creating actuated devices to operate within a diagnostic MRI. This knowledge was gained through a systematic approach to understanding, isolating, characterizing, and circumventing difficulties associated with developing MRI-guided interventional systems. These contributions have been validated on the levels of the individual modules, the total development system, and several deployed interventional devices. An overview of this work is presented with a summary of contributions and lessons learned along the way.

Acknowledgements

The dissertation presented here would have been neither valuable nor possible without the immense efforts of so many people, institutions and organizations. I am deeply indebted to many different individuals but also to Worcester Polytechnic Institute, the mechanical engineering department, and the A.I.M. lab specifically. Though schools are not generally mentioned in acknowledgements, the support, freedom, and understanding Worcester Polytechnic Institute has given me during the time I spent here has both exceeded what I could have ever expected, and been instrumental in my success.

I would like to thank first and foremost my advisor Dr. Gregory Fischer, for his continued support, faith and patience with my work. I appreciate the guiding wisdom of his experience and his thoughtful encouragement and insights. He has truly helped me shape my education and professional development into a career, and taught me about so much more than just engineering and science.

The mechanical engineering department at W.P.I. and A.I.M. lab has been a second home for me both figuratively and sometimes literally. I would like to thank the students and staff in the A.I.M. lab for being my colleagues, codevelopers, friends and sometimes family, including Hanlin Hong, Benzun Pious Wisely Babbou, Satyanarayana Janga, Yuangfang Gui, Yan Xiaoan, and Yi Wang. I would like to give a special thanks to my closest collaborators in the A.I.M. Lab without whom none of this work would have been possible, Weijian Shang, Gang Li, Kevin Harrington, Alex Camilo, and especially Dr. Hao Su.

I would also like to recognize Dr. Gretar Tryggvasson and Dr. Michael Gennert for the contributions they've made to my academic growth during my years at Worcester Polytechnic Institute. I would of course like to mention the exceptional support staff of the mechanical engineering department and robotics engineering program, including Pamela St. Louis, Barbara Furhman, Barbara Edilberti, and Tracey Coetzee. I would also like to thank Professor James Van De Ven for giving me my start in research. He provided me exceptional opportunities, even as an undergraduate, and was a constant source of guidance even after I left his laboratory.

I would also like to thank Dr. Julie Pilitsis, and Dr. Robert Norton for taking time out of their busy schedule to serve on my dissertation committee. I would also like to thank Dr. Pilitsis for working with us as our clinical consultant and co-author on many papers. Your input was invaluable for making these projects viable.

Of course, I could never have come this far without my family. I am blessed to have a family who encourages me to pursue my scholastic dreams. My parents never faltered in their unwavering support of my education and the pursuit of my passions. My grandparents were always there for me with love and support. Finally, I need to thank my wife, Andrea Sereny. Without her help I would never have gotten to where I am today both professionally and personally.

This work would not have been possible without the help and support of my family, friends, colleagues, school and advisor over the past seven years. I extend my deepest thanks to everyone who facilitated my pursuit of robotics engineering.

Abbreviations

DBS	D eep B rain S timulation
STN	S ub T halamic N ucleus
SNR	S ignal to N oise R atio
MRI	M agnetic R esonance I maging
fMRI	f unctional M agnetic R esonance I maging
ioMRI	i ntra o perative M agnetic R esonance I maging
AIM Lab	A utomation and I nterventional M edicine L aboratory
EMI	E lectro m agnetic I nterference
3T	3 T esla Field Strength
PZA	P iezoelectric A ctuator
COTS	C ommon O ff T he S helf
RAS	R ight A nterior S uperior
DOF	D egree O f F reedom
MER	M icro E lectrode R ecording
RCM	R emote C enter of M otion
CT	C omputed T omography
NEMA	N ational E lectronic M anufacturers A ssociation
RFA	R adio F requency A blation
RF	R adio F requency

OTS	O ptical T racking S ystem
PID	P roportional I ntegral D erivative
FPGA	F ield P rogrammable G ate A rray
MROI	M easurement R egion of I nterest

Contents

Abstract	ii
Acknowledgements	iii
Abbreviations	v
List of Figures	xi
List of Tables	xiv
1 Introduction	1
1.1 Dissertation Contributions	2
1.2 Literature Review	8
1.3 MRI Guided Interventional Robotics	12
1.4 MRI-Guided Neural Stereotaxy	14
2 MRI-Compatible Modular Architecture	16
2.1 Overview	16
2.2 Contributions	20
2.3 System Architecture	22
2.3.1 Initial System Architecture	22
2.3.2 Adaptation of Initial System	23
2.3.3 Current Expression of System Architecture	28
2.4 System Modules	32
2.4.1 Piezoelectric Actuator Driver	33
2.4.1.1 Evolution of Architecture and Designs	35

2.4.1.2	Final Embodiment Development . . .	40
	Needs Assessment	40
2.4.2	Integrated Infrastructure Enclosure	43
2.4.2.1	First Prototype Modular Enclosure . . .	45
2.4.2.2	Final Module Concept	48
2.4.3	Backplane & Signal Aggregator	54
2.4.4	Power Supply	55
2.4.4.1	Driving Design Parameters with EMI Properties	58
2.4.4.2	Synchronous Operating Principles and Analysis	62
2.4.4.3	Physical Construction and Testing . . .	65
2.4.4.4	Final Power Supply Implementation . . .	66
2.4.5	Console Room Interface Unit	68
2.5	Experimental Validation	70
2.5.1	MRI Compatibility Evaluation	70
2.5.1.1	Image Subtraction Analysis of Image Noise	73
2.5.1.2	Single Image Measure of Image Noise . . .	74
2.5.1.3	SNR Calculations and Results	75
2.5.2	Joint-Level Accuracy	76
2.6	Discussion	77
3	Characterization of Piezoelectric Actuation to Enable Advanced Control	80
3.1	Overview	80
3.2	Contributions	82
3.3	Principals of Operation	83
3.4	Modeling Approaches	85
3.5	Proposed Direct Force Control Method	88
3.6	Development of Force Testing Equipment	89
3.7	High Speed Microscopy	91
3.7.1	High Speed Camera Observation	92
3.7.2	Stroboscopic Microscopy	96
3.8	Experimental Protocol and Data Analysis	99
3.9	Discussion	101

4	MRI-Guided Stereotactic Neural Intervention System	103
4.1	Overview	103
4.2	Contributions	105
4.3	Design Requirements	107
4.3.1	Workspace Analysis and Specifications	107
4.3.2	Performance Requirements	109
4.3.3	System Architecture	110
4.4	Mechanism Design	111
4.4.1	RCM Mechanism	112
4.4.2	Prismatic Base	113
4.5	Application of Modular Device Development Platform	114
4.5.1	Robot Controller System	115
4.5.2	Interface Software	116
4.6	Validation	119
4.6.1	MRI Compatibility	119
4.6.2	Accuracy	121
4.6.2.1	Benchtop OTS Evaluation	121
4.6.2.2	MR Image-Guided Evaluation	122
4.7	Discussion	126
5	Conclusions	130
5.1	Summary of Work	131
5.1.1	Interventional Development System Architecture	131
5.1.1.1	Piezoelectric Actuator Driver	131
5.1.1.2	Switching Regulator Guidelines	133
5.1.1.3	E.M.I. Management Practices	133
5.1.2	Piezoelectric Actuator Analysis and Characterization Hardware and Methods	134
5.1.3	Stereotactic Neural Intervention System	135
5.2	Impact and Future Work	135
5.2.1	MRI-Guided Development System	135
5.2.2	Neural Intervention System	136
5.3	Dissertation Contributions	137
5.4	Lessons Learned	138

Appendix	139
A Characteristics of Electrical Requirements for Driving Piezoelectric Actuators	140
A.1 Quasistatic Actuators	140
A.2 Harmonic Actuators	141
Bibliography	144
Curriculum Vitae	159

List of Figures

1.1	Image of deployed system components in their final form	6
1.2	Original architecture adapted for use by this system .	7
1.3	Adapted software architecture	8
1.4	Stereotactic Neural Intervention Devices	10
2.1	Image distortion caused by stainless steel needle . . .	18
2.2	Initial system architecture	23
2.3	First control system prototype installed	25
2.4	Biological analogy of system application	29
2.5	Current system architecture	30
2.6	Interior of in-room controller and module placement .	34
2.7	Example of noise sources from COTS PZA drivers . .	36
2.8	Schematic and simulation results of discrete piezoelectric driving amplifier	37
2.9	First prototype of piezoelectric actuator driver	39
2.10	Current architecture of piezoelectric actuator board .	43
2.11	Image of current piezoelectric driver board	44
2.12	Prototype progression of Faraday enclosures	45
2.13	First modular Faraday enclosure	46
2.14	Final Faraday enclosure	49
2.15	Implementation of shielding lip	51
2.16	Diagram of serpentine enclosure penetration and results of EMI blocking calculations	54
2.17	Backplane Signal Aggregator	56
2.18	Sawtooth Wave Components	60
2.19	Architecture of synchronous buck converter	62
2.20	LTSpice model of switching regulator	64

2.21	Simulated startup transient of MRI-compatible switching regulator	65
2.22	Prototype MRI-compatible power supply	67
2.23	Implementation of modified COTS switching regulator	68
2.24	Comparison of outputs of modified and unmodified switching regulators	69
2.25	Interface unit	70
2.26	NEMA Definition of Measurement Region of Interest	75
2.27	MRI Compatibility results of the modular system	76
2.28	Joint-level accuracy analysis	77
3.1	Quasistatic actuator architecture presented by Szufnarowski <i>et. al</i>	84
3.2	Quasistatic actuator modeling results presented by Szufnarowski <i>et. al</i>	86
3.3	Effects of loading on quasistatic PZA performance presented by Arafa <i>et. al</i>	87
3.4	Relationship between step size and load of a quasistatic PZA	88
3.5	Diagram of force analysis device	91
3.6	Interaction of driving legs and drive strip of PiezoLEGS PZA	93
3.7	Experimental setup for high speed camera study of PZAs	94
3.8	Sample image of PZA driving crystal taken with high speed camera	95
3.9	Timing diagram of stroboscopic illumination trigger	97
3.10	Experimental setup for stroboscopic microscopy video capture of crystal leg motion	98
3.11	Sample image of PZA driving crystal taken with high speed camera	99
3.12	Representative plot of force control data	100
4.1	Comparison of current DBS placement procedure and proposed procedure	105
4.2	Neural Intervention System Setup	106
4.3	Ergonomics of neural intervention armature	108

4.4	Kinematic definition of neural intervention system . .	110
4.5	Initial design of the RCM mechanism	113
4.6	Ergonomics and workspace of neural stereotaxy mechanism	114
4.7	Diagram of prismatic base for neural intervention system	115
4.8	Deployment of control system of neural intervention system	116
4.9	Frame transformations for registration of neural intervention manipulator within RAS coordinates	118
4.10	Qualitative demonstration of MRI compatibility of neural intervention system	120
4.11	Experimental setup for accuracy analysis of neural intervention system	123
4.12	Accuracy analysis plot	125
4.13	Sheeps head experimental setup	126
4.14	Sheeps head experiment result	127
5.1	Examples of projects build with modular system . . .	132
A.1	PiezoLEGS driving waveform: Rhombus S Wave . . .	141
A.2	PiezoLEGS driving waveform: Rhombus F Wave . . .	142
A.3	PiezoLEGS driving waveform: Omega Waveform . . .	142
A.4	PiezoLEGS driving waveform: Modified Sine	143
A.5	Harmonic Actuator Driving Waves	143

List of Tables

2.1	Functional specification of final piezoelectric actuator driver	41
2.2	Experimental Results of MRI Compatibility Evaluation showing SNR and percentage change	72
4.1	Experimental Results of MRI Compatibility Evaluation showing SNR and percentage change	121
4.2	Results of neural intervention system accuracy analysis	125

This work is dedicated to my parents, Russell and Susan Cole, my grandparents Bernard and Roberta Cole, and my wife Andrea Sereny.

Chapter 1

Introduction

The work presented here intends to be a step forward in the advancement of image guided surgery through the creation of a modular development platform to streamline the creation of MRI-guided robotic surgical assistant devices. Construction of MRI-guided robotic devices is often frustrated by the strong magnetic fields within the scanner room and high sensitivity to electromagnetic interference (EMI). Though many off the shelf MRI safe electromechanical devices exist, these often cause unacceptable image degradation when operated during imaging, preventing systems constructed with them from motion during live imaging. To overcome these difficulties a modular, MRI-compatible set of devices, components, and software was constructed that would allow a user to focus on the functionality of a device under development rather than construction of supporting infrastructure that would preserve image quality. This modular development platform was then applied to the creation of a neurosurgical device.

A neurosurgical device was created to improve upon one of the most commonly utilized neurosurgical approaches, neural stereotaxy, by making direct, *in situ* MRI guidance available to reduce targeting

errors, procedure cost, and patient trauma. *This dissertation describes the design of a novel computer-integrated robotic mechanism capable of operating within the bore of a diagnostic 3T closed-bore MRI, shown in Fig. 1.1, completely reshaping the clinical workflow of the procedure to improve patient outcomes through reduction of cost, risk and procedure time.* The mechanism presented in this paper will allow for precise, automated positioning of a cannula guide, while maintaining a workspace similar to a commonly used Leksell stereotactic surgical frame (Elekta AB, Stockholm, Sweden). The device will serve to improve patient outcomes through the reduction of targeting errors and procedure time by eliminating image fusion procedures and allowing for *in situ* live guidance of the procedure by high resolution MRI. Other groups have utilized methods to avoid electromechanical actuation during live imaging, such as interleaving actuation with imaging as demonstrated by Krieger *et al.* [1], or utilizing less precise but reliable pneumatic actuation methods as demonstrated by Fischer *et al.* [2]. In contrast to these approaches, this project utilizes precision piezoelectric actuators *during* live imaging through the application of the modular MRI-guided device development platform also presented here.

1.1 Dissertation Contributions

As described previously, the number of groups currently developing MRI-guided interventional robotic systems with electromechanical actuation is rapidly expanding. In addition to this, while there are resources available detailing components, actuators, and subsystems that are MRI-compatible, there is currently no pathway to the

creation of an MRI-guided actuated system that does not require professional development and integration of these subsystems and components. This dramatically increases both financial and temporal costs associated with bringing an interventional device from concept to reality. Compounding these frustrations is the difficulty associated with producing an electronic processing and driving system which can be operated within the scanner bore without causing signal interference that degrades image quality. The ease with which a possible pathway for electromagnetic interference leakage can be overlooked, thus ruining an entire day of experimentation, can wind up being quite costly with scanner time typically exceeding \$250 an hour, at a discounted academic rate.

This dissertation describes a refined, pre-integrated, modular system which can be used “out of the box” to rapidly develop new interventional devices and which requires only the time needed to develop procedural and kinematic designs of new devices.

The development of this system has been guided by the parallel development of a novel system for stereotactic neural interventions which leverages direct MR imaging to decrease the procedural time, costs, placement error, and trauma of deep brain stimulation electrode placement.

The major contributions of this dissertation are as follows:

1. Development of a hardware system architecture for development of MRI-guided devices which maximizes modularity through functional isolation.
2. Development of an integrated, modular, scanner-independent electronics hardware infrastructure capable of supporting a plurality of modular actuation and sensing devices, with interfaces

designed to streamline development of new modules. This system currently supports the piezoelectric actuator (PZA) driving module described below, as well as a variety of new modules developed by others.

3. Characterization of design and construction methods to develop high efficiency MRI-compatible switching regulator power supplies. Though ubiquitous in modern electrical design, these devices needed to be fundamentally redesigned such that they could be operated within the scanner room during live imaging without destroying image integrity.
4. Characterization of methods for driving PZAs within the bore of diagnostic MRI scanners, and refinement of a multimodal PZA driving module capable of supporting a variety of PZAs with a range of driving signal requirements. This driver has been validated to achieve precision control far exceeding that of the supported encoding systems.
5. Development of equipment and methods to enable the characterization of PZAs for the development of advanced control algorithms and motor driving optimization.
6. Development of a manipulator enabling MRI-guided, actuated stereotactic neural intervention which leverages *in situ* imaging to dramatically reduce procedure time, cost, placement error, and trauma. While the basic manipulator design is for stereotactic interventions generally, the presented linkage has been specifically developed for placement of deep brain stimulation (DBS) electrodes.
7. Analysis of neural stereotaxy manipulator. The neural intervention system was analyzed from many perspectives leading

to a multitude of system iterations. The system was analyzed in terms of its positioning accuracy, image compatibility, targeting accuracy, ergonomics, and workflow. An optical tracking system was used to determine the performance of the mechanical system, independent of the imaging system, while phantom studies were used to determine the total targeting accuracy of the image guided system.

The products of these contributions are physically expressed as four major hardware components:

1. Robotic manipulator
2. Scanner room controller
3. Interface unit
4. User workstation

The hardware components comprise a complete, modular surgical system development platform shown in Fig. 1.1, and were developed based on the methods and understanding described above. As can be seen, the user workstation, which connects to the interface unit, is deployed in the scanner control room. This interface unit communicates via fiber optics passed through the scanner room patch panel wave guide to the MRI robot controller located close to the scanner bore. This unit operates the interventional device within the scanner isocenter. Though the interventional device presented below is a stereotactic neural system, the strength of the modular system is the ability of any user to rapidly develop a new surgical manipulator without modifying the remaining components of the system in any

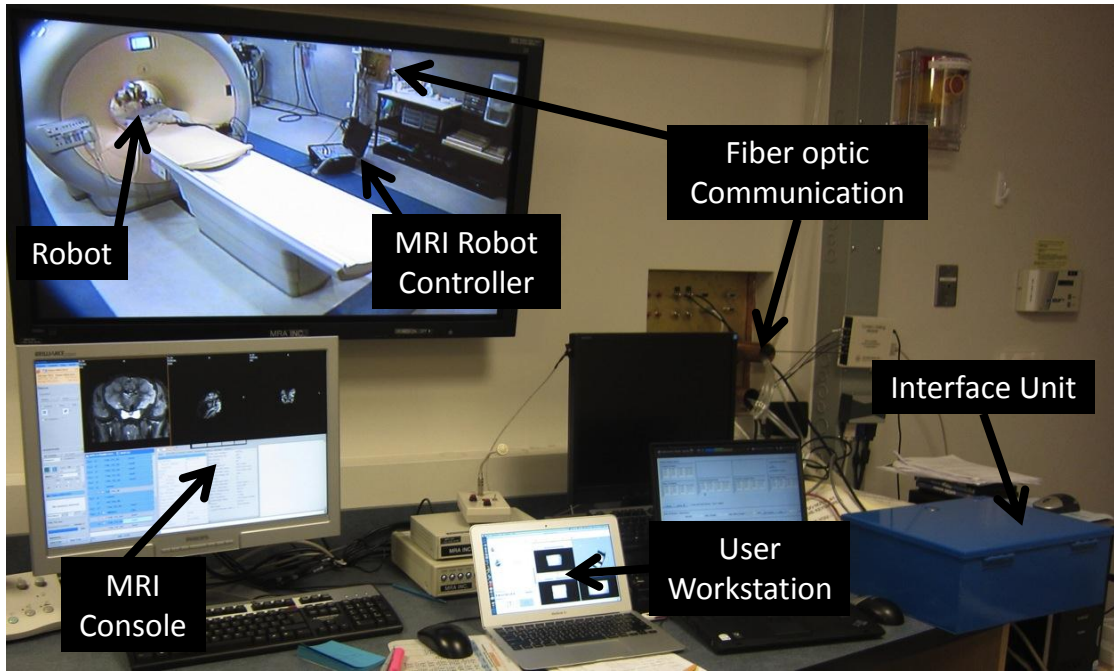


FIGURE 1.1: Image taken from the scanner control room displaying all major system components. A manipulator is placed within the scanner bore, the scanner room robot controller is adjacent to the scanner, and fiber optic communication is passed through the patch panel to the interface unit, which resides in the control room. The interface unit manages communication between the user workstation and the rest of the system.

significant way.

Background of Supporting Technology

The system upon which this dissertation is based is a collaborative effort, particularly the higher level interface software architecture. The general architecture for MRI-guided interventional devices shown in Fig. 1.2 served as the starting point for this system, and indeed much of the work on acquisition of scanner images and integration with navigation software and registration fiducials is adapted from Tokuda *et al.* [3].

Upon restructuring of the hardware architecture to distribute functional allocation, Su *et al.* greatly refined the kinematic processing,

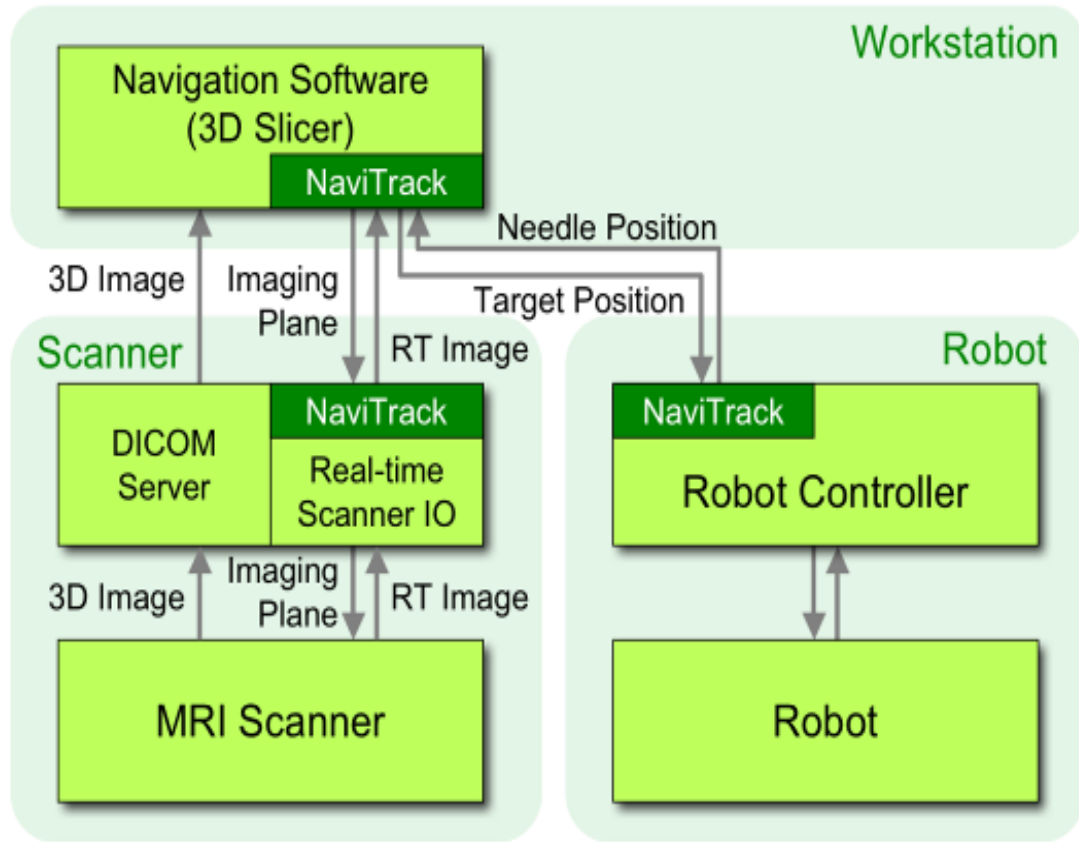


FIGURE 1.2: Original system architecture developed by Tokuda *et al.* on which this system was based [4]. This system utilized a control computer integrated with the scanner room controller and was not based on distributed processing of DOF control. This figure taken from Su *et al.* [5]

software structure, and workflow of the system, as shown in Fig. 1.3 [5]. Calculation of forward kinematics, inverse kinematics, and registration are isolated within the control PC, allowing the navigation software located on the user workstation to communicate with the modular system entirely in terms of patient coordinates and registration information. In addition to this software and command structure, the multi-image registration processes detailed by Shang *et al.* were used to locate the manipulator in right-anterior-superior (RAS) coordinates [6]. Note that this is patient/scanner coordinates.

As part of this work, a neural intervention system was developed comprising several modules, including a 3 DOF prismatic motion base developed by Shang *et al.* While the work presented is shown to

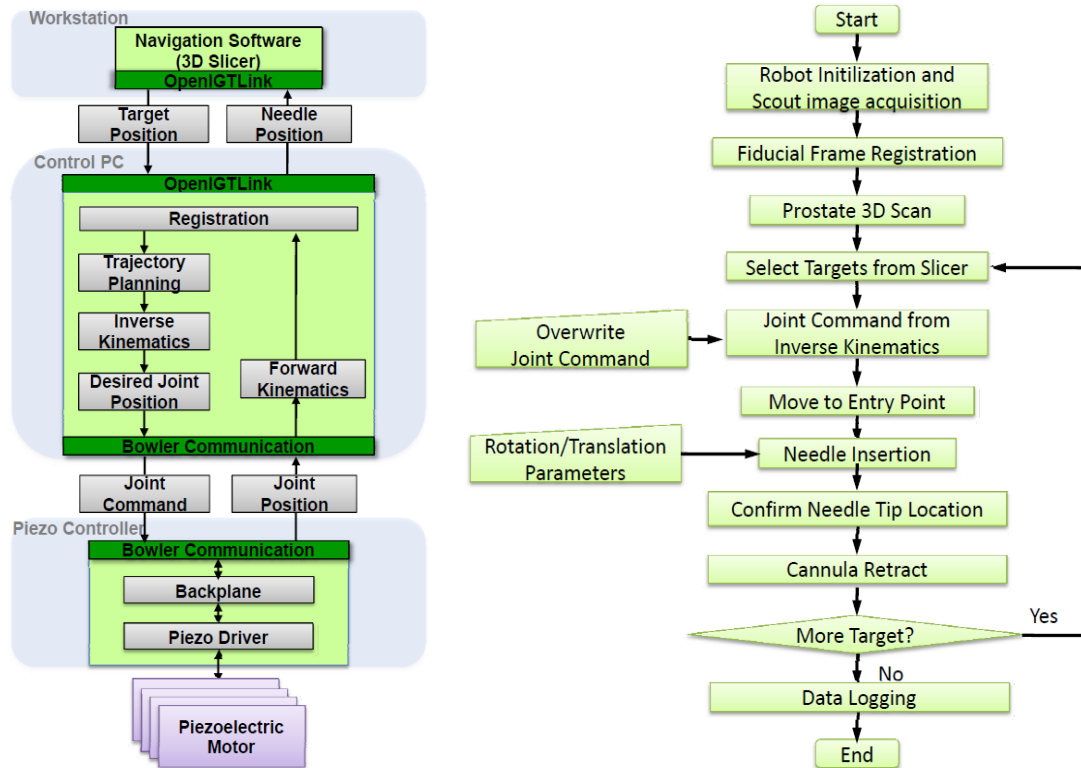


FIGURE 1.3: Software architecture and MRI-guided needle placement workflow refined by Su *et al.* that supports the present work [5]. These two figures taken from Su *et al.* [5]

be independent of specific registration methods, navigation software, communication software, and prismatic translation devices, these devices and methods were used during the integration, validation, and testing of the presented contributions.

1.2 Literature Review

Image-guided surgical technology is a rapidly expanding field which seeks to compliment a surgeon's skills with advanced computational, visual and mechanical augmentation [7]. The earliest presentation of an image-guided intervention is the stereotactic neural system

described by Horsley *et al.* in 1908, shown in Fig. 1.4[8]. Stereotactic surgery is a method of minimally invasive surgery where a 3-dimensional coordinate system is used to localize interventional targets within the body. The cartesian coordinate system used by the Horsley-Clarke device made application to humans difficult due to the inability to use X-Ray imaging to visualize details of the anatomical structure of the human brain. Later, in 1949, a Swedish neurosurgeon by the name of Lars Leksell developed a new stereotactic frame for brain surgery based on polar coordinates, rather than cartesian coordinates, to ease calibration in the operating room [9]. Since this initial polar coordinate based device was invented, a variety of additional stereotaxy devices based on a polar coordinate system have been created including the Sandstrom Stereoguide (Sandstrom Trade and Technology Inc, Ontario Canada), and the Integra CRW (Integra LifeSciences Corporation, Plainsboro, New Jersey) (Fig. 1.4). Many of the currently used stereotactic neural systems use some form of radiological imaging, *i.e.* CT or X-Ray, to register the position of the frame to preoperative imaging. However this registration procedure is susceptible to error, and often necessitates secondary forms of physiological confirmation such as micro electrode recording. A logical extension for image-guided intervention is the addition of precise, computer-controlled motion coupled with *in-situ* image guidance in the form of interventional robotics.

While many researchers have made the case for the benefits of adding real-time direct MRI guidance to neural interventions, efforts toward this end have been frustrated by difficulties associated with creating MRI-compatible robotic systems [10, 11]. Diagnostic magnetic resonance imaging is one of the most effective imaging modalities available to the medical professional for viewing internal soft tissue

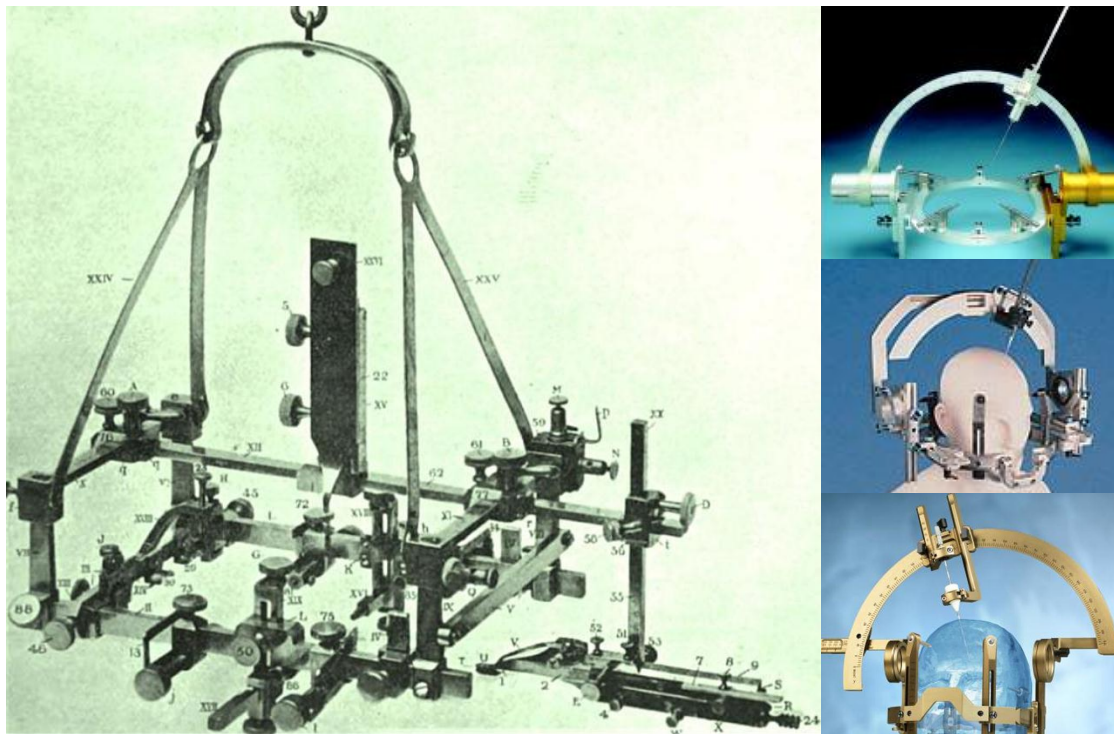


FIGURE 1.4: Left: The first image-guided interventional device used to localize internal structures of the brain based on bony structures of the skull and cartesian coordinates[8]. Right Top: Sandstrom Stereoguide polar stereotactic system. Right Middle: Radionics CRW polar stereotactic system. Right Bottom: Current version of the Leksell polar stereotactic system.

structures. The ability to use this modality for live guidance during surgical procedures would prove invaluable for targeting or manipulating internal structures that are difficult to reach. Procedures such as deep brain stimulation (DBS) and percutaneous prostatic intervention, inspiring Masamune, *et al.* [12] and Chinzei, *et al.* [13] to begin development of MR guided robotics. Tsekos *et el.* [14] has published a recent review of MRI-compatible systems developed for image-guided interventions. In addition, a comprehensive review of the challenges facing the development of MRI robotics prepared by Gassert *et al.* can be found in [11].

Due to the highly sensitive and unforgiving electromechanical environment within the scanner, one of the primary challenges to creating

electromechanical MRI guided robotics is the development of an actuation system. Using pneumatic technology — including pneumatically actuated robotic devices such as the MrBot driven by PneuStep pneumatic stepping motors [15] and pneumatic stepping motors currently being developed in the AIM Lab — can achieve a very low level of image interference. However, electromechanical systems offer clear advantages in scalability, simplicity, size, and inherent robustness over pneumatically actuated systems. A recent piezoelectric approach to prostatic interventions is described by Krieger *et al.* [16], but, as with other published devices based on PZAs, this system causes unacceptable image quality loss under motion and must interleave motion with imaging. *While these devices and others discussed in [17, 18] do not depict the entire state of the art, they do highlight one of the two main problems being addressed: the current inability to generate and control precision electromechanical motion during live high-field (greater than 1.5T) MR imaging without affecting image quality.*

The contributions presented here fall into two groups. The first set of contributions address this issue through the creation of a modular, integrated device development platform designed to streamline the creation of new MRI-guided robotic intervention systems. The second set of contributions leverages the benefits of this system to create and validate a stereotactic neural intervention system targeted at reducing procedure time, placement error, patient trauma, and cost by making direct MRI guidance available in real time.

1.3 MRI Guided Interventional Robotics

Though image guided interventional robotics dates back to 1985 when a PUMA 560 robot was used to place a needle for brain biopsy via CT guidance, MRI guidance of interventional robotics was not attempted until nearly a decade later [19]. Robotic assistance for instrument placement under MRI has been investigated beginning with neurosurgery [12] and later for percutaneous interventions [20–22]. Many early systems were targeted at low field strength MRI such as those developed by Chinzei *et al.* [23] and were eventually adapted for transperineal intraprostatic needle placement [24]. Krieger *et al.* presented a 2-degree of freedom (DOF), passive, un-encoded, and manually manipulated mechanical linkage to aim a needle guide for transrectal prostate biopsy with MRI guidance [25], similar to that developed by Beyersdorff *et al.* [26]. In addition to this passive system, a piezoelectrically actuated version was developed, though image degradation caused by the electromechanical actuation system has frustrated attempts at motion under live imaging [1]. Another MRI-guided robotic system for prostate biopsy and intervention based on pneumatic actuation was presented by Fischer *et al.* [2] and further refined by Song *et al.*, replacing a single vertical DOF with a base platform capable of a variety of insertion angles [27]. Other efforts have focused on MRI-guided prostate interventions [28, 29], MRI-compatible haptics [30], a spinal intervention system utilizing both pneumatic and piezoelectric actuators presented by Hemple *et al.* [21], and a system for biopsy and radiofrequency ablation (RFA) of breast tumors presented by Kokes *et al.* [31].

Actuation Techniques

Various methods to create and control motion within an MRI environment have been utilized, such as piezoelectric and pneumatic methods outlined by Fischer *et al.* [32]. These motor technologies include the pneumatic stepping motor PneuStep actuator presented by Stoianovici *et al.* [33], an air motor for limb localization described by Elhawary *et al.* in [34], and a method for coupling motor driver timing with excitation pulse timing to reduce interference with imaging described by Suzuki *et al.* [35]. The last method has demonstrated an effective reduction of image interference; however, system integration is cumbersome and scanner-dependent. Other recent developments in MRI-compatible mechanisms include pneumatic stepping motors on a light needle puncture robot [36], the Innomotion commercial pneumatic robot for percutaneous interventions (Innomedic GmbH, Herxheim, Germany) [37], and haptic interfaces for functional MRI (fMRI) [38]. Further efforts have been made to place actuators distant from the scanner bore by using transmission systems such as the hydrostatic system presented by Ganesh *et al.* [39].

The feasibility of using piezoelectric motors as compared to other actuation technologies under MR image guidance is presented by Fischer and Krieger *et al.* in [32]. In addition to piezoelectric actuation methodologies, hydrostatic and hybrid hydrostatic-pneumatic systems — such as those described by Yu *et al.* in [40] and Gassert *et al.* in [38] — have been developed, leveraging their inherent compatibility. While these actuation systems are being adapted to use in the scanner bore, entirely new methods of actuation are being developed, including the scanner-driven actuation of micro-manipulators described by Vartholomeos *et al.* [41] and shape-memory alloy-driven

devices such as those presented by Ho *et al.* in [42]. These technologies show promise; however, they are early in their development and do not have the benefit of years of industrial use.

Gassert *et al.* describe MRI-compatible robotics as essential to both image-guided interventions and neuroscience, claiming that not only will the technology benefit interventional medicine, but neuroscience research as well [43]. Nathoo *et al.* describe differing levels of control of robotic systems with which neurosurgeons will eventually need to become familiar [44], while Haidegger *et al.* provide a comprehensive review of the most recent developments in robot-assisted neurosurgery [45].

1.4 MRI-Guided Neural Stereotaxy

Stereotactic surgery was first developed to enable neurosurgeons to target and treat diseases affecting deep structures of the brain, such as the basal ganglia [46]. Traditional stereotaxy is very time consuming, as it requires the completion of hundreds of steps with millimetric precision in order to properly plan and execute a procedure. Inaccuracies may arise from errors in one or more steps in the procedure, or may be secondary to brain shift that occurs intra-operatively. Traditional stereotactic guidance derived from CT or MR images that are obtained before the procedure does not accommodate brain shift that is unavoidable once the cranium is opened and cerebrospinal fluid is lost. Intra-operative MRI (ioMRI) affords neurosurgeons the opportunity to accommodate brain shift during surgery [47]. According to [48], the surface of the brain is deformed

by up to 20mm after the skull is opened during neurosurgery, and not necessarily in the direction of gravity.

A means of physiological real-time feedback such as microelectrode recording (MER) has classically been used for *in situ* feedback for certain procedures such as deep brain stimulation (DBS) electrode placement in the subthalamic nucleus (STN) [49, 50]. While MER has been used very effectively for DBS electrode implantation, there are many other procedures where MER may be less useful. In addition to this, it has been shown that improvements in implantation accuracy have been achieved through direct MRI guidance of the implantation in conjunction with an MRI-compatible manual frame such as the Medtronic (Medtronic Corporation, Minneapolis, MN) NexFrame and the Surgivision (MRI Interventions, Memphis, TN) ClearPoint system [51]. While STN DBS is one example of a clinical procedure performed with neural stereotaxy, others include biopsy, drug delivery, gene therapy, and tumor ablation. In 2001, Hadani *et al.* postulated that the time requirements and difficulty associated with creating MRI-compatible robotic systems for neurosurgery were too great to generate significant motivation to produce one [52]; however, since that time, great advances in MRI-compatible robotic technology have been made.

Chapter 2

MRI-Compatible Modular Architecture

2.1 Overview

The development of any image guided robotic system faces a variety of technological challenges and tasks, including component selection, architecture definition and ultimately, integration, testing, and validation. When attempting to create such a system to operate within the bore of and be guided by a diagnostic MRI, a host of additional constraints are introduced. These constraints are largely driven by two properties of MR scanners inherent to their principle of operation:

1. **High strength, alternating magnetic field:** Prohibits the use of all magnetic materials, as well as significantly limits the use of conductive material. These materials can cause image degradation, inductive heating, dangerous forces.
2. **Extreme sensitivity to EMI:** The scanner constructs images through the interpretation of a narrow bandwidth of radio

waves. Many common electronic devices produce EMI which contain subcomponents and harmonics that can interfere with scanner image generation.

Fischer *et. al* discuss how one of the greatest challenges to creating a device of this nature is achieving the required compatibility in terms of patient and operator safety and image quality when constructing actuation systems [32]. Bennet *et. al* also describe the difficulties involved in using conductive and magnetic materials such as metals and certain ceramics in the design of MRI-compatible devices, as they can pose serious risk to patient safety and image quality if their geometry is not carefully selected [53]. In addition, conductive materials can have currents induced in them which can pose both a safety hazard in terms of localized heating and image interference by altering field inhomogeneity, as can be seen in Fig. 2.1. The strength of these currents are dictated by the geometry, orientation, and material properties of the conductive object, however currents large enough to cause extremely rapid heating of conductive objects has been observed. Because these safety and image compatibility issues can be detrimental, methods to characterize and circumvent these problems have been documented, and methods to quantitatively predict their effects are being researched as presented by Chinzei *et. al* [54].

While the safety and compatibility issues discussed earlier are significant and require attention, EMI emitted by electronic control and communications hardware as described by Su *et. al* and Stoianovici *et. al* [33, 56] are a much more difficult to ameliorate source of image degradation from MRI guided robotics. Most common forms of electronics, especially those containing oscillators and switching

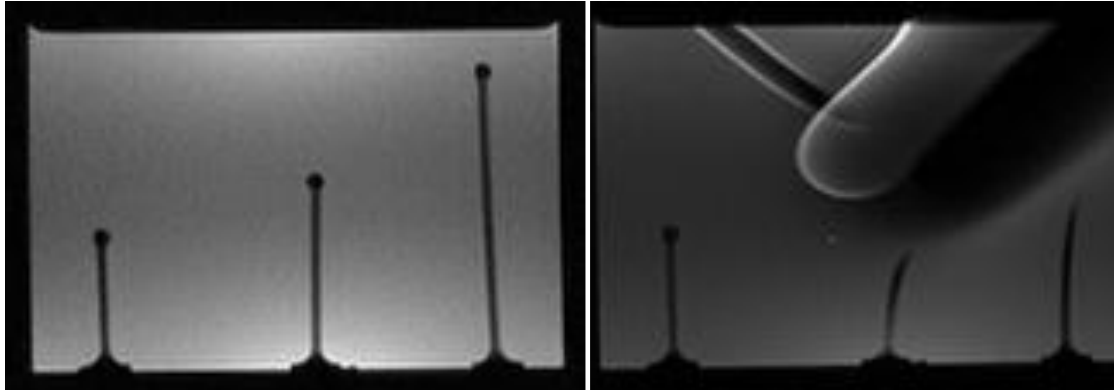


FIGURE 2.1: Left: MR image of a phantom with vertical posts as targets. Right: MR image of the same phantom with a stainless steel needle inserted; note how the distortion of the image makes the vertical posts seem curved. This figure taken from Fischer [55].

power regulation, will radiate EMI which is interpreted by the scanner as noise in the generated images. The most common method for analyzing this interference is through measuring the change of the signal-to-noise ratio (SNR) caused by the additional devices. SNR is a common metric when analyzing the quality of MR images. Interference with a scanner is often discussed in terms of the *change* in SNR caused by the presence of external equipment as a quantitative measure of the equipments effect on the operation of the scanner. Avoiding high frequency electrical noise is difficult when constructing an MRI-compatible system with active motion due to the lack of commercial off-the-shelf (COTS) electronic devices designed to prevent or limit EMI.

To minimize the effects of this electrical interference, many have used pneumatic actuation methods. However many pneumatic actuators require complicated control algorithms in order to maintain the accuracy required for surgical intervention, as presented by Bone *et. al*, Acarman *et. al*, Comber *et. al*. [57] and Wang *et. al* [58–60]. While these are several examples of pneumatically actuated MRI guided

devices, it is by no means an inclusive list. Though piezoelectric actuators (PZAs) can cause a great deal of image degradation during operation in the scanner bore, they nevertheless have been used to create a variety of MRI-compatible interventional robotics. In applications where live motion during imaging is not required, PZAs micrometer precision and high holding force made them an attractive choice, because when they're not energized they generally have holding force which exceeds their driving force. These applications almost exclusively interleave motion with imaging, such as those described by Sutherland *et. al* and Krieger *et. al* [1, 61]. Suzuki *et al.* demonstrated a method to detect when the scanner was reading images, such that the actuators can be disabled during the scanner's receive phase, thus eliminating scanner imaging noise caused by motors. But this also prevents truly live imaging during motion [35]. This interleaved motion method — as well as signal filtering, placing motors remote from the scanner bore, using RF shielding drapes over the actuator, and others — serve to define the boundaries of the problem of MRI compatibility of oscillating electronics and their role in operating MRI-compatible electromechanical actuation rather than solving it. By understanding the sources of image degradation caused by electronic and electromechanical systems operating within the scanner room, new equipment can be designed to create no interference, rather than attempting to suppress the interference after the fact. If enough modular components to construct a complete image guided, PZA-driven robotic system are redesigned to be inherently MR-compatible, developers of further MR-compatible mechatronic technologies could devote a much larger portion of their resources to their specific areas of interest rather than the infrastructure to support their research. *The work presented in this chapter*

is the development of a modular, pre-integrated MR-compatible development platform. The system includes communication, registration, actuation, and sensing modules such that the user can design a mechanism using any of the supported components and materials, insert the mechanism kinematics into the control system, and immediately have a functioning MR-guided mechatronic system, registered to patient coordinates, operating under live imaging with near-zero SNR change. This system has been validated in terms of its image compatibility, component-level-accuracy, and system-level-accuracy, all of which have exceeded desired specifications. In addition, the system has been shown to support rapid device development by ourselves, our collaborators, and an external group.

2.2 Contributions

Currently, the lack of MRI-compatible infrastructure for the development of MRI guided devices forces researchers and developers to expend a great deal of time and money constructing supporting equipment for the technologies intended to be their main contributions, detracting from their overall effectiveness. To alleviate this burden, a modular MRI-compatible device development platform was created. Presented is the development and integration of a series of hardware and software modules that comprise this platform, which have been created to preserve quality of scanner images during operation. The final architecture was created with a focus on functional isolation and interface design to improve modularity and extensibility. The products of these efforts form the contributions of this chapter and can be summarized as follows:

1. Developed device development platform hardware and architecture design.
2. Characterized sources of EMI from PZAs and common electronic infrastructure devices.
3. Developed and refined versatile, MRI-compatible PZA driving electronics capable of operating a variety of COTS actuators .
4. Developed electronic infrastructure and enclosure system to support the operation of the development platform modules within the scanner room.
5. Validated systems compatibility.
6. Validated systems mechanical performance.

Experimental results are presented demonstrating that the system is capable of operating a wide variety of off-the-shelf PZA's within a diagnostic scanner bore while maintaining lower levels of interference and SNR change than any other published results using similar actuators and imaging studies in addition to serving as a complete robotic motion control systems underlying infrastructure. While the modules presented and validated in this dissertation are primarily intended to support piezoelectric actuation, the architectural model is further validated by the work of other researchers who have created additional system modules extending the capabilities of this system to support the operation of pneumatic actuation, fiber optic force sensing, and reflective encoding. Furthermore, additional modules are currently being developed to support both shaped ablation therapy and controlled resistance devices for fMRI-based rehabilitation.

2.3 System Architecture

2.3.1 Initial System Architecture

Work previously undertaken by Fischer *et al.* in the development of a pneumatically actuated, MRI-guided prostate intervention system yielded a functional control system architecture that was initially targeted for adaptation to use with PZAs rather than pneumatic cylinders, as presented in [2, 62, 63]. This architecture, shown in Fig. 2.2, is comprised of three major components: a user workstation, an in-room controller, and an interventional device. The user workstation operated navigational software and communicated with the in-room controller via NaviTrak, a predecessor to OpenIGTLink [64]. The in-room controller used a single central computing and intelligence platform that processed sensor information to execute control loops, simplifying the device's design and construction but limiting the expansibility and reconfigurability of the system as a whole. This centralized processing approach used direct analog voltage outputs to operate piezoelectrically driven pneumatic control valves. One of the major advantages of this system is that it has no specific scanner requirements and requires no interaction with scanner equipment other than image acquisition. While the system does require a penetration pathway between the scanner room and the control station, almost all scanners have a penetration panel with a waveguide suitable for passing a fiber optic cable into the scanner room.

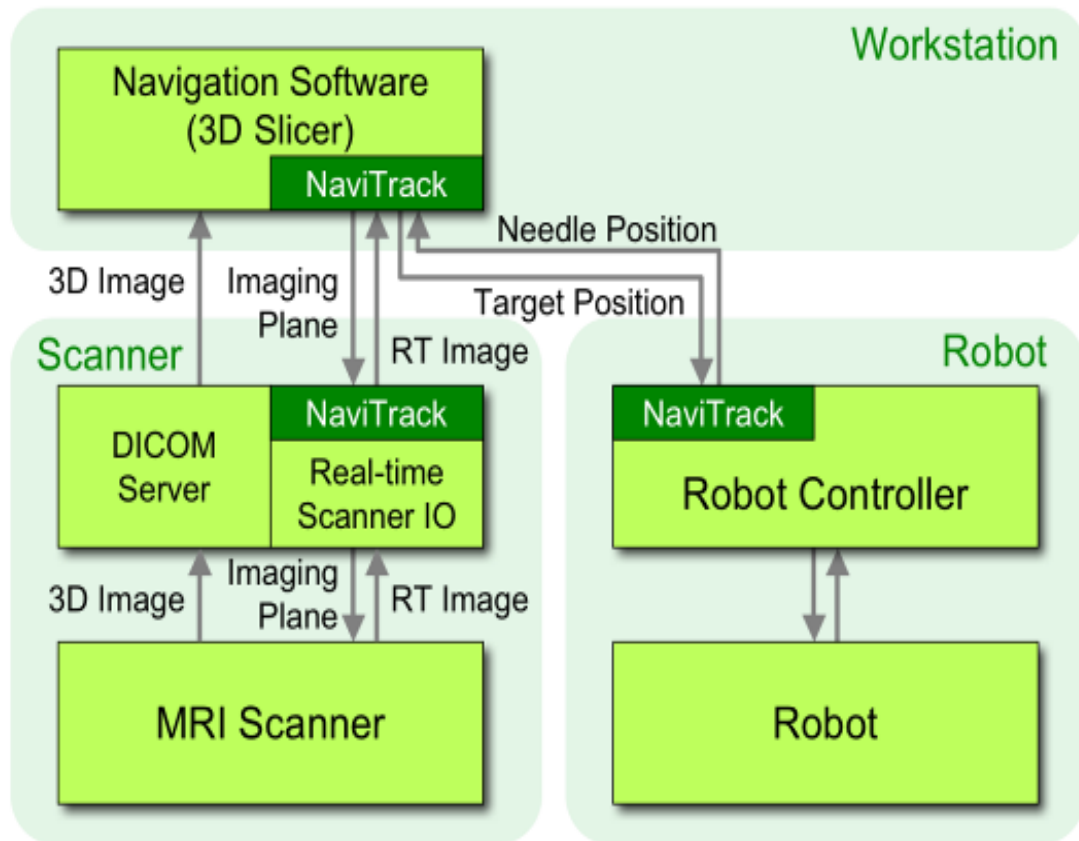


FIGURE 2.2: Architecture of original pneumatic control system initially adapted for control of electromechanical actuation. Note how the user workstation processes only navigation and high-level commands, while the processing unit within the in-room controller handles all kinematics and real-time operations.[65]

2.3.2 Adaptation of Initial System

Selection of Piezoelectric Actuation:

When considering actuation methods an MRI guided mechatronic system, a primary concern must always be safety, especially considering the proportion of controllable actuators constructed with ferromagnetic materials. Because of this, the two most commonly used methods of actuation for devices whose motion is to be computer controlled within the scanner are pneumatic and piezoelectric. Pneumatic systems offer high force, design simplicity and inherent MR compatibility, while PZAs innately offer much higher degrees of

precision, scalability, and simplicity of implementation. The main drawback to PZA's, however, is the inability to operate them during imaging without causing unacceptable levels of image degradation. Wang *et al.* presents an attempt to prevent interference caused by the quasi-static Piezo LEGS motor (Piezomotor, Uppsala, Sweden) through modification of its driving electronics with the application of electronic filtration[66]. While the results were promising enough to indicate the possibility of operating piezoelectric actuators within the scanner bore without causing image interference, they were by no means complete, as the scan protocols utilized were designed to improve SNR through the use of very long scan times with a large number of averages. Because the high speed of image creation necessitates a much shorter scan time with a low number of averages, live imaging protocols for MRI are inherently much more susceptible to electrical interference. This type of imaging protocol is both the most useful for image guided intervention, as well as being one of the most susceptible to being degraded by EMI so it was chosen to be used as the benchmark for MR compatibility of the system.

The final decision to utilize piezoelectric actuation as the primary actuation modality instead of pneumatic actuation for the new system was based on leveraging the following possible advantages:

1. Greatly increased robustness of position control methods
2. Ability to utilize a single energy source (eliminating requirement for compressed air)
3. Physical size advantages
4. Inherent force-speed-torque properties allowing motors to be utilized without drivetrains or gearing

5. The current lack of ability to operate these actuators within the scanner bore without image degradation represented a technological opportunity.

Since the first mechanisms targeted for development by the lab could operate interleaving motion with imaging, the initial control system was constructed using off the shelf PZAs and driving electronics as can be seen in Fig. 2.3. This was done with the intention of improving the systems image compatibility through further investigation and refinement.

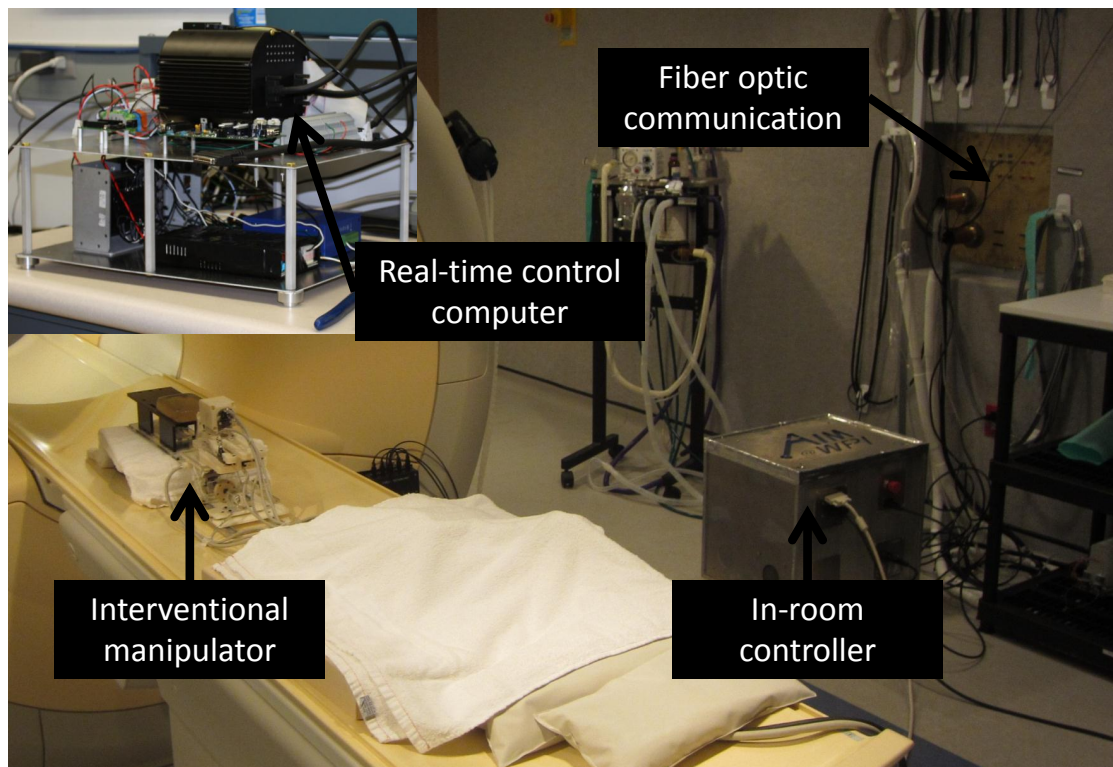


FIGURE 2.3: First functional system deployed, with manipulator in scanner bore and controller adjacent. Note the fiber optic connection passing through the scanner room patch panel. Inset: Construction of equipment within the in-room controller.

Difficulties Leading to New Architecture: Leveraging the previous system’s design for the in-scanner controller, a real-time control PC monitored all encoding devices to operate all control loops and

output motion commands to the actuator drivers with no inherent processing. This was essentially identical to the one shown in Fig. 2.2, with the exception of the piezoelectric control valves being replaced with piezoelectric motor drivers. At this point, the real gap in knowledge was apparent. While researching methods for driving PZAs within the scanner bore to integrate with this system, it was determined that a large portion of the image interference caused by PZAs could be circumvented through the use of precision arbitrary signal generators to create driving waveforms, as described in Section 2.4.1. Once the new methodologies proposed for low-noise operation of PZAs were experimentally shown to offer a near-zero SNR change [67], the impracticality of containing all digital processing within a centralized processing unit became apparent. At this point the most important decision of this project was made: *to redistribute the functional allocation of the control system from a centralized processing architecture to a distributed processing architecture*. This would effectively move all real-time processing to the level of the individual driver modules. To accommodate this the redesigned PZA drivers were developed with on-board embedded processing that would receive discrete commands, rather than constant analog control, as well as pave the way for a much more extensible, reconfigurable modular system.

New Architecture Requirements: The primary motivation for creating a new, refined system is allowing the user to significantly narrow the focus of efforts towards developing MRI-compatible actuated technologies by leveraging the robust functionality and compatibility of the complete development platform. The new architecture system sought to improve modularity of the proposed system over

the original system by isolating the interpretation of joint level commands and control loop operation from the central processing units through the application of distributed processing. By creating intelligent actuator driving modules that receive DOF level *commands*, which are then interpreted and used to operate control loops within the driver itself, a more effective functional isolation is created. By creating a defined hardware and software interface between the centralized processing and communication system, new actuators and components can easily and reliably be integrated into the central system by creating a new driving *module* supporting those interfaces. The development of an isolated *module* is more complicated with a distributed processing system than a centralized system. However once the development of the module is complete, its application is more straightforward, versatile and robust. As the system is designed to ease the development of new technologies by others, robustness was a priority. The summation of these requirements yielded the following list of needs:

1. All system modules must maintain acceptable levels of image interference when used as intended.
2. They must support the operation of actuation and sensing components determined to represent a cross section of those currently being used by the industry.
3. Hardware and software interfaces must be designed and defined such that new system hardware modules can be rapidly developed.
4. Preference will be given to COTS devices, however any modification to a COTS device must be in the form of an externally

manufacturable, additional component such as a filter or conductive shield.

5. The system structure must enable a developer with a focused background to deploy functional, actuated devices quickly and easily.

By creating an extensible, modular platform constructed of hardware and software *modules* which can be altered or replaced without affecting the remainder of the system, the user can easily reconfigure any number of the system elements to create a desired final project. If an analogy between a robotic system can be drawn, the work presented in this chapter represents all of the flesh of an animal, including muscles, sensory organs, brain matter etc., with all the complicated subsystems supporting life already working together. The user can then give form to the creature simply by developing a skeleton that defines the structure of the final being, and the way that it moves, as depicted in Fig. 2.4.

2.3.3 Current Expression of System Architecture

As can be seen in the architectural diagram presented by Su *et. al* in Fig. 2.5, the main difference between the current system architecture and the previous one is the separation of the central processing unit and the actuator drivers[5]. While the change in the architectural diagram is small, the effect on the implementation of the system is dramatic. The previous architecture required a monolithic, in-room control unit to process commands from the user workstation, encoder and sensor information, operate control loops and generate real time actuator control signals. The new distributed processing

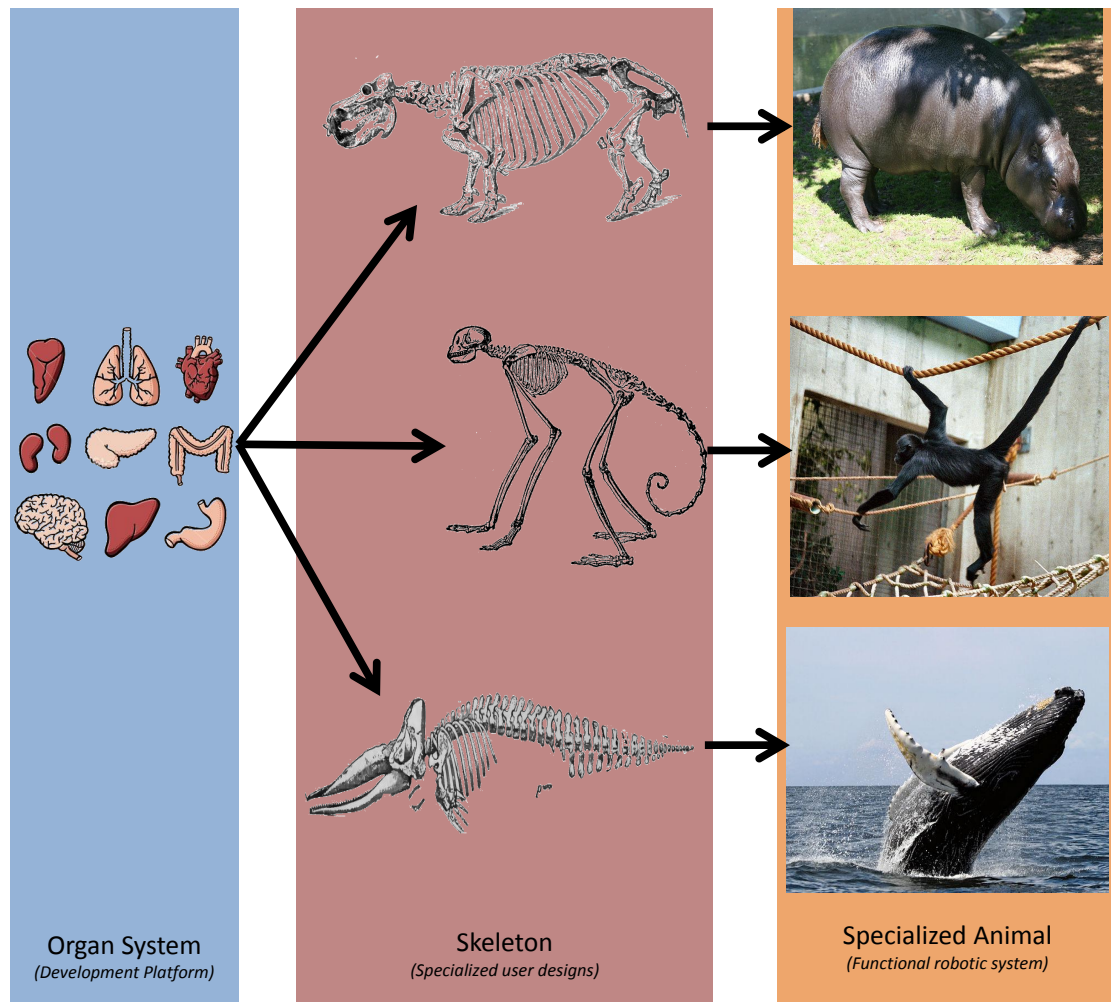


FIGURE 2.4: Biological analogy of the development platform. Left: The system represents a series of connected and balanced tissues and organs ready to support the life of a creature. Middle: The user development represents a focused mechanical design which serves to specialize the generalized infrastructure to an adapted task, represented by a series of animal skeletons. Right: The final system implementation is represented by several incredibly diverse and specialized animals adapted to unique ways of life, yet based on the same core biological principles.

architecture leverages the hardware separation of low-level and high-level processing to move the majority of computing equipment to an interface unit which resides in the scanner control room. Being located external to the scanner room allows the interface unit to be constructed without concern for its MR compatibility, as the scanner is shielded from it.

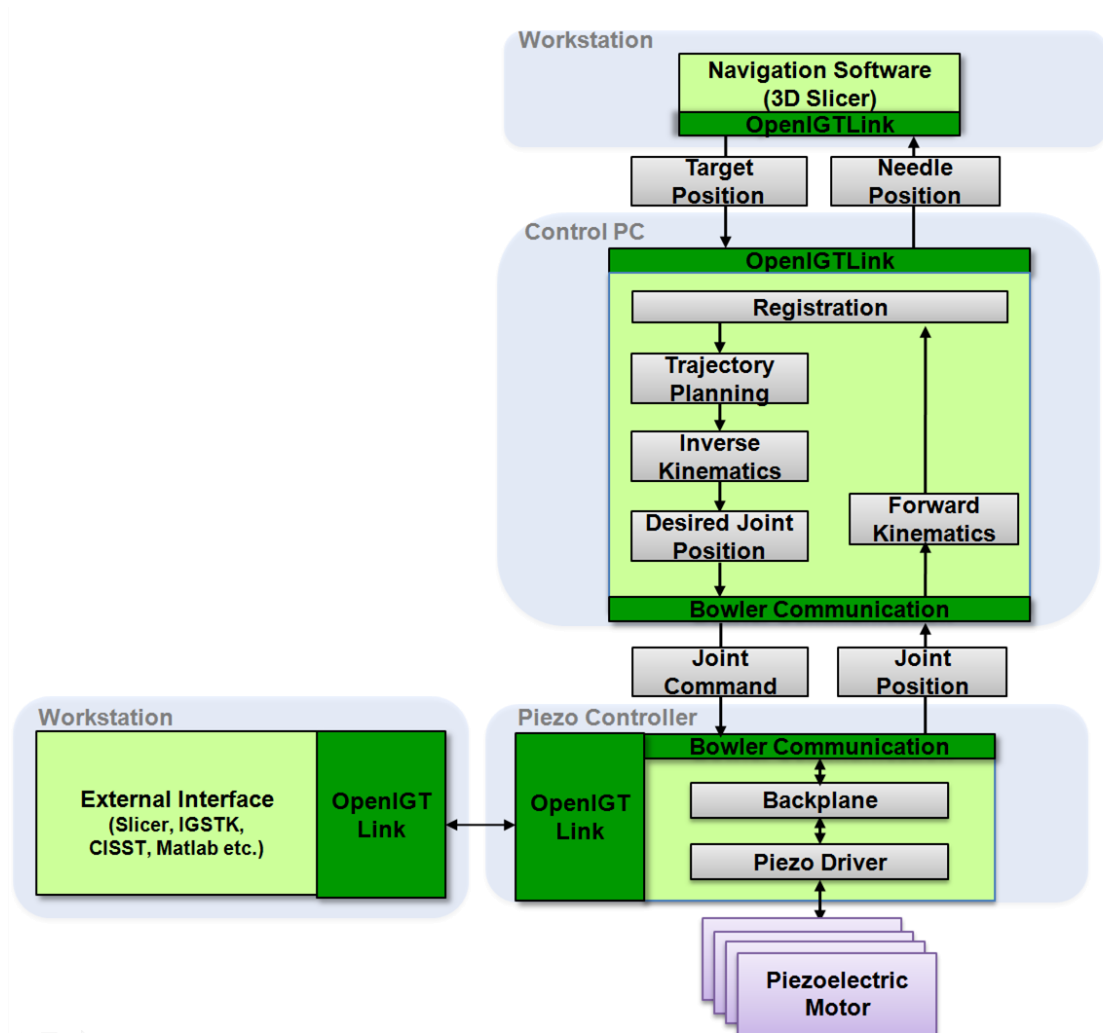


FIGURE 2.5: Current system architecture showing major hardware components and software responsibilities, as presented in this figure prepared by by Su *et al.* [5]. Note that the piezoelectric motor drivers function in real time and operate in machine-level units (encoder tics), the control PC performs kinematic processing and converts commands back and forth between joint-level commands in machine units and system-level commands in patient coordinates, and the workstation primarily operates navigation software to determine target locations and procedure planning. An alternative command method uses the workstation to calculate kinematics to produce joint-level commands which are pushed down directly to the in-room controller.

The new version of the in-room controller is also dramatically reshaped to support modular development. Certain modules such as power supplies, communication modules, electrical shielding and signal aggregation are constructed as an integrated infrastructure enclosure supporting a plurality of interchangeable modules. Currently developed interchangeable modules focus on the control of various

electromechanical actuators, however the hardware and software interface allows for the development of modules with a wide variety of capabilities. The distributed processing architecture makes the development of new modules more labor intensive as an embedded digital processing section must be integrated with each new device. But once a module has been successfully completed, the total system is more easily reconfigured. The set of modules used to create the complete support infrastructure and initial actuation systems are discussed in depth in this chapter, and include the following devices:

1. **Piezoelectric Actuator Driver:** A module developed to operate a number of commercially available PZAs, despite vastly different driving requirements. This device interfaces with the backplane signal aggregator, operates actuation, encoding and sensing devices, and is located in the in-room controller. This module was designed to be easily applied to more generic motion control and I/O applications.
2. **Integrated Infrastructure Enclosure:** A pre-integrated infrastructure platform that supports the interchangeable modular equipment of the scanner room controller. While this unit is comprised of several distinct modules itself, it is designed to function as a cohesive unit, pre-assembled in a configuration best suited to the end users' needs to support the application of reconfigurable modules.
3. **Backplane & Signal Aggregator:** Concatenates the majority of electrical connections between the reconfigurable modules and the rest of the scanner room controller, as well as supports a digital communication handler that manages data flow from

the unique drivers to the control computer. The current version accomodates up to 8 interchangeable modules.

4. **Console Room Interface Unit:** Converts fiber optic ethernet from the in-room controller back to standard ethernet and houses the control PC, which interprets commands from navigation software in the user workstation to DOF level commands sent to the interchangeable modules.
5. **Software Architecture:** Communication structure developed to tier and isolate abstraction layers that maximize functional isolation.
6. **Registration Hardware and Methods:** Hardware unit utilized to register the manipulator with patient coordinates.

These modules serve as the support structure and interface definition which can then be used to rapidly develop application specific mechanisms and software. The application specific devices are effectively modules themselves, however they should be optimized to accomplish a specific task, whereas remaining system modules are generalized to support system operation. An example of an application specific mechanism is the stereotactic neural device presented in Chapter 4.

2.4 System Modules

The following sections describe the research and development process for creating and refining specific custom components of the modular MRI-compatible development system, as an expression of the architecture described above. Each of these devices were selected for

development due to the lack of a commercially available analog which was MRI safe while maintaining acceptable levels of image interference. Though PZAs were targeted for the primary actuation method for initial applications of this system, shown in Fig. 2.6, available drivers used to operate these motors can cause a large amount of image degradation while driving actuators during scanning [32, 68]. The development process for each of the system components components followed the same basic structure:

1. A COTS version of a required component or module is shown to be either unavailable, unacceptable, or cost prohibitive.
2. The primary source of interference caused by the device is determined, as well as the reasons the device was designed in a manner that produces the interference.
3. The device is redesigned such that the interference or safety issue is removed, ideally through circumvention, but possibly through suppression.
4. A prototype device is constructed and validated.
5. A robust, final version of the device is refined, including a manufacturing pipeline.

2.4.1 Piezoelectric Actuator Driver

The piezoelectric actuator driver represents one of the central contributions to the modular development system, and underwent several iterations of simulation, production, experimentation, and revision. Initially, this research effort was targeted only to operate

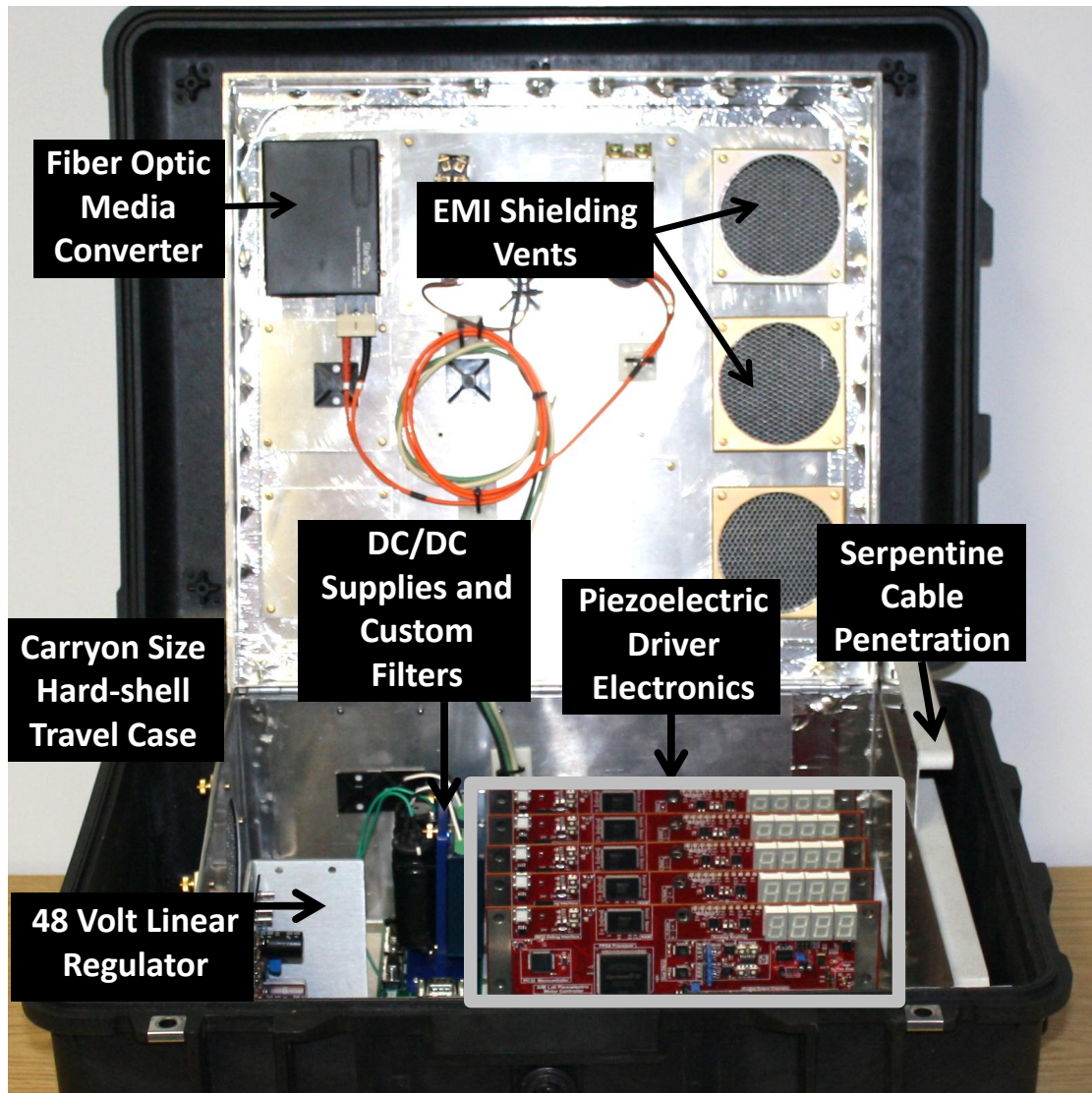


FIGURE 2.6: Note the fiber optic media converter with a permanent bulkhead penetration, EMI shielding vents positioned over power amplifiers for cooling, location of the linear regulator above the wheels, serpentine cable penetration, and piezoelectric driver circuitry.

non-harmonic Piezo LEGS walking actuators (PiezoMotor, Uppsala, Sweden) However, success of this first application coupled with the limited mechanical properties of Piezo LEGS actuators necessitated the redesign of this device to support a wider range of PZAs, including both harmonic and non-harmonic motors. This posed an even more complicated challenge, as the the differences between the driving waveforms and control methods of various PZAs can be significant. The Piezo LEGS PZA, a typical non-harmonic, requires

4 high precision synchronized driving waveforms, ranging from 0-48 volts at a frequency range of approximately $750Hz - 3kHz$, while a Nanomotion (Nanomotion Corporation, Yokneam Israel), requires two synchronized driving waveforms centered at ground with an RMS of approximately 450 volts at a frequency of $50kHz$, representing the maximum among typically used PZAs. The standard architecture for drivers of these motors is based on a switched transistor system that further compounds difficulties in creating this device. While these systems are very efficient and inexpensive to construct, the switching of the transistors introduces high frequency artifacts commonly known as “ringing.” This was identified as the primary source of scanner interference caused by these drivers, as can be seen in Fig. 2.7. The progression of the development of these drivers first focused on developing and validating an amplifier capable of driving the desired actuators while controlling higher frequency sub-components, then developing a complete device robustly supporting its operation.

2.4.1.1 Evolution of Architecture and Designs

Due to the difficulty of driving capacitive loads coupled with the need for tightly controlled amplifier performance to limit noise from being introduced in the scanner, a discrete transistor AB-style amplifier was initially targeted for the analog driving stage. First, this circuit was designed and simulated using NI Multisim to determine load capabilities, distortion, and transient response to changing loads, as shown in Fig. 2.8. While this approach showed very promising results in simulation, in practice it was not successful. The circuit

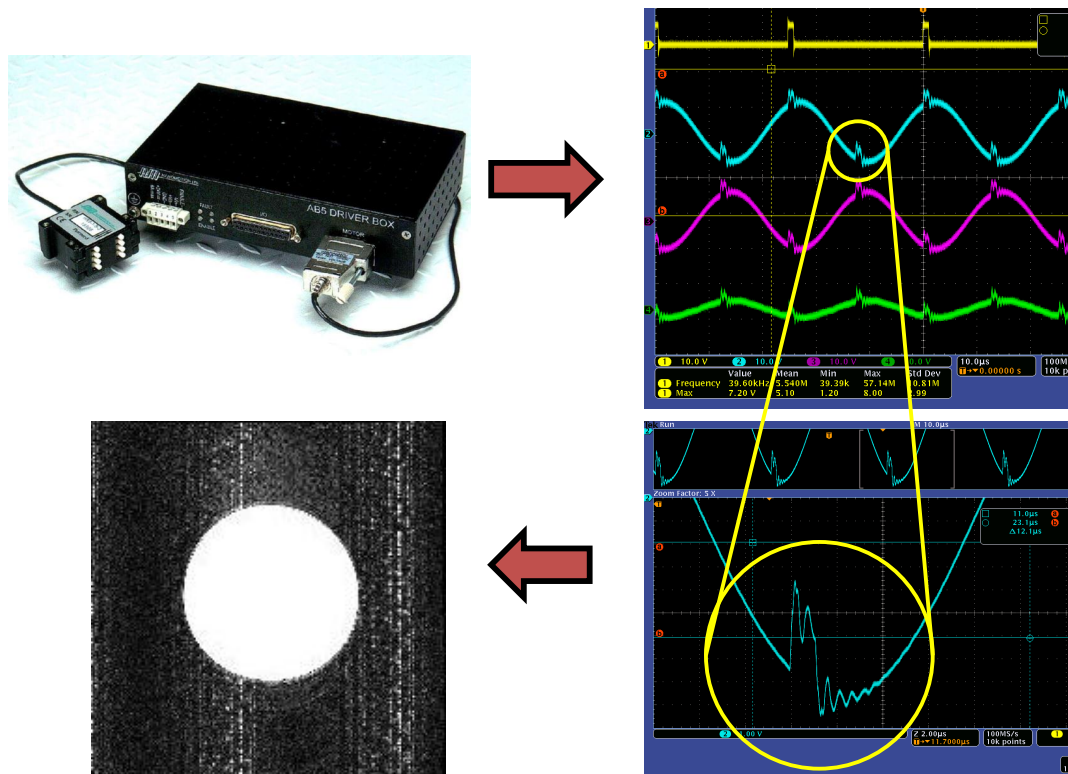


FIGURE 2.7: Upper Left: Non-magnetic Nanomotion motor and driver. Upper Right: Capture of waveforms produced by driver. Lower Right: Close up of high frequency artifact transmitted on motor driving lines. Bottom Left: Scanner image showing the effect of the high frequency artifact.

proved to be unstable with failure analysis revealing that the structure of the circuit, coupled with the high capacitive load, made it highly susceptible to thermal runaway leading to burn out. At this point several methods to improve the circuit were analyzed, including thermally coupling the transistors, adding buffering to make the circuit less prone to runaway, and utilizing linear amplification. Initial review of the design capabilities indicated that while discrete transistor amplification stage can be applied in more elegant and versatile methods with much higher power efficiency and current carrying density. Despite these benefits, the simplicity, robustness and noise free operation of a linear amplification stage made it the better choice. Eventually, a power circuit based on the OP549 Linear Amplifier (Texas Instruments, Dallas Texas), coupled with a pi-filter

output to control noise was analyzed using NI Multisim. When simulated experiments predicted stable operation of the circuit under the desired loads with less than 0.25% total harmonic distortion, the circuit was finalized and constructed.

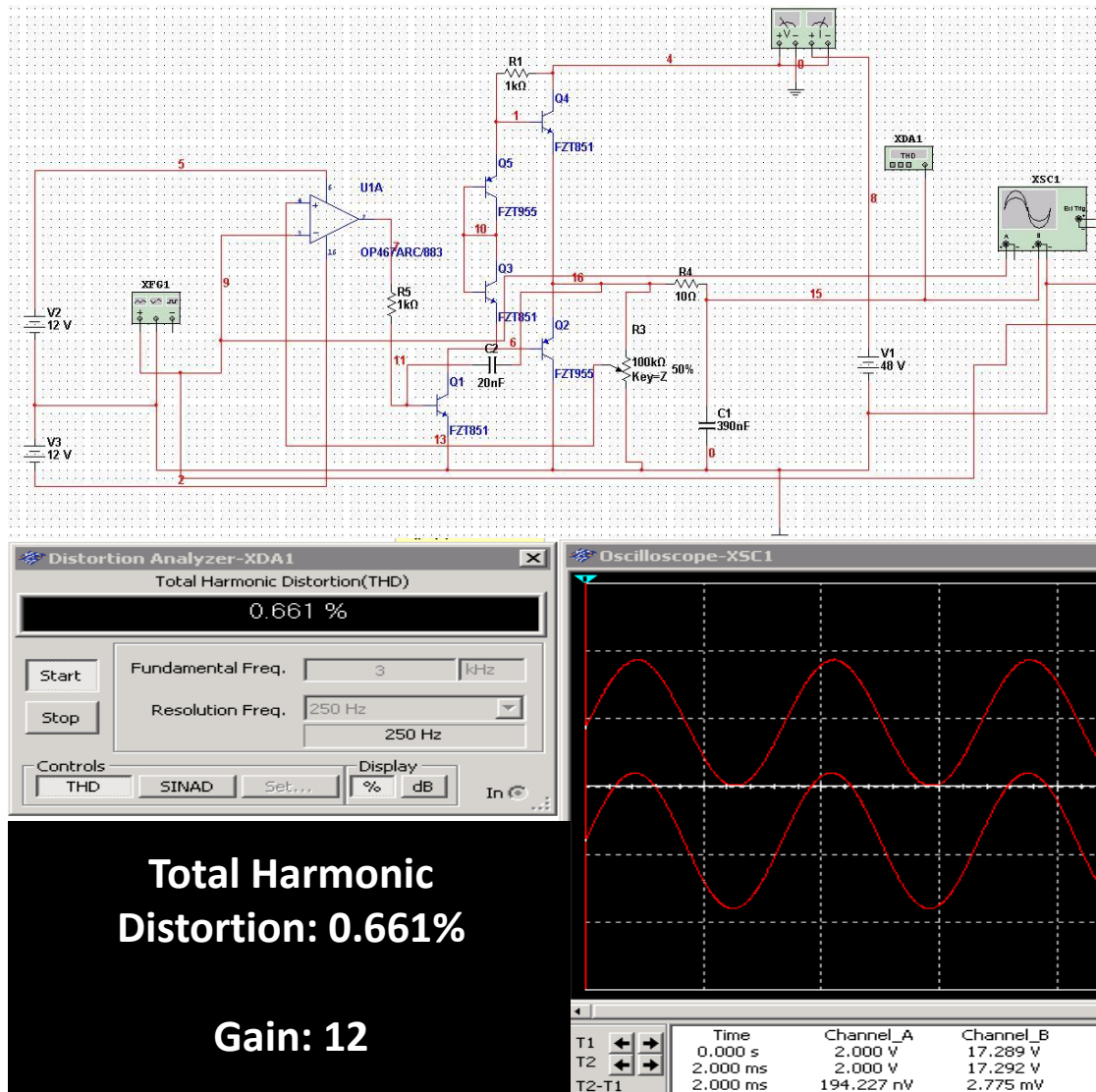


FIGURE 2.8: Top: Schematic of AB-style amplifier initially targeted to operate Piezo LEGS amplifiers. Note the discrete transistor structure and representative load of a motor channel. Bottom: Multisim instrument output of amplifier model. Note the low total harmonic distortion (THD) calculation.

As discussed in Appendix A, Piezo LEGS quasi-static actuators utilize a single drive waveform which is phase offset and inverted to produce four independent driving signals. When a drive waveform that

is symmetrical in both directions is selected, a circuit which generates only two phased waveforms can be used in conjunction with two unity gain inversion amplifiers to generate the driving signals for the remaining two channels. Applying the previously discussed power stage to amplify these signals allowed the use of a COTS stereo audio device to generate driving waveforms for the initial validation of the amplifier performance, both in terms of image interference, and motor functionality. MatLab (The MathWorks Inc., Natick Massachusetts) was used to encode phased driving waveforms into stereo audio files, which were then encoded to MP3 files that were then loaded onto an iPod shuffle (Apple Computers, Cupertino, California) which was used to provide the operating signals required by the above described signal processing circuit. These waves were amplified by the experimental power stage and used to drive the PZA in the scanner.

Initial tests of the new amplification system demonstrated very little SNR loss (1.9% maximum, 0.5% average) while effectively driving the actuator within the isocenter of the scanner bore. This indicated that a robust printed circuit board (PCB) version of a driver should be developed with integrated digital signal synthesis. The first generation controll was developed to behave like a traditional COTS servo amplifier, where it receives and analog control signal proportional to the output. This structure necessitated the operation of a real-time computing platform within the control box in the scanner room, as analog velocity commands cannot be transmitted reliably through the scanner room patch panel without causing image interference. This version of the controller was the first to be successfully produced on a printed circuit board, as shown in Fig. 2.9. Linear

regulators were used to step down the 48-volt power supply rail to create the lower voltages required to operate the driver's subsystems.

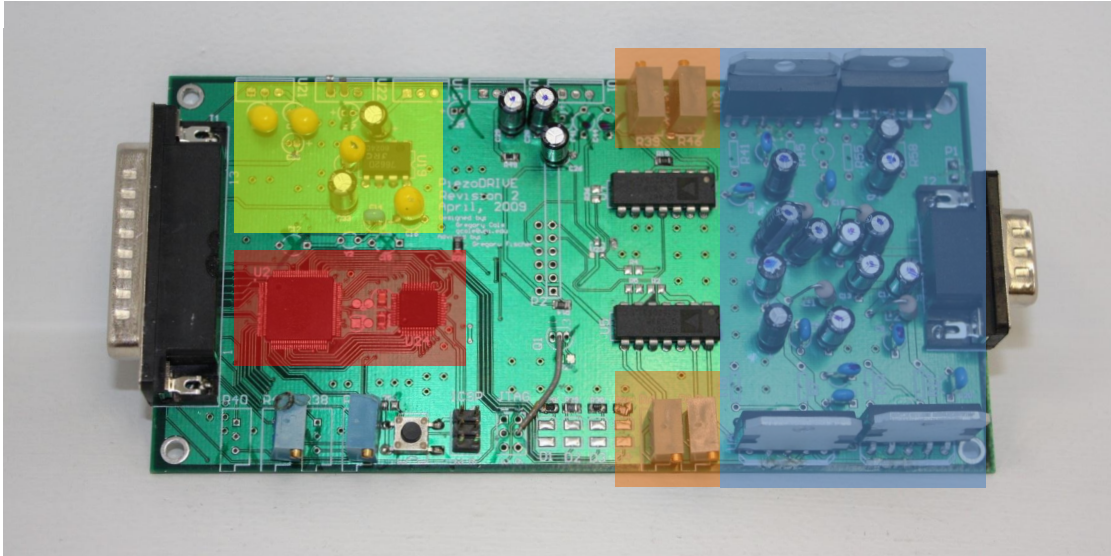


FIGURE 2.9: Image of the second complete revision of piezoelectric actuator board, with functional blocks identified. Blue box contains power amplification stage and output filtering, orange boxes contain trimming resistors used to adjust gains and DC bias, red box contains digital processing stage, and yellow box contain I/O protection circuitry.

The initial prototype of the amplifier was evaluated in benchtop trials, and was determined to operate within specification, then integrated with the first generation robot controller. The unit was initially designed to operate off of a single 48-volt power input. Both intermittent instability of the step-down power converters and the availability of regulated power supply channels within the controller led to the boards subsystems being driven by power supplies common to all devices within the control unit, greatly improving reliability. This observation later influenced functional allocation of the redesigned system architecture.

Experimental analysis revealed that this control structure was reliable, repeatable and offered the lowest published SNR change of

any group attempting to operate a similar PZA under similar imaging conditions. In addition to this, the system was entirely scanner agnostic. These results were presented by Wang *et al.* in [67].

2.4.1.2 Final Embodiment Development

Successful integration of the first MRI-compatible modular architecture led to a careful analysis of successes, difficulties, and failures of that system. The results of this audit of system performance indicated that while the individual components of the system performed very well, ineffective integration practices had yielded serious stability and robustness deficiencies. At this point, the architecture was redesigned, focusing on distributed processing, durable construction and interface design. In order to develop a robust, extensible and dissemination-ready final product, a systems engineering approach was taken to ensure effective interface design and total system stability.

Needs Assessment An expanded set of desired hardware and software capabilities of the piezoelectric driver unit was developed, as well as an interface design. Hardware and software components targeted for support were selected based upon research into optimal devices for construction of current laboratory projects, as well as a cross-section of components currently being used by other laboratories for image-guided interventional devices, displayed in Table 2.1.

Analog Functional Specifications:

Communication	Actuation	Encoding	Sensing and Input
USB	Nanomotion	US Digital Optical Encoders	Button
Serial	PiezoLEGS	Potentiometer	Digital I/O (25)
Board-to-Board	PCB	Reflective Encoder	Analog I/O (5)
	Squiggle		FPI Sensor
	Shinsei		

TABLE 2.1: Piezoelectric actuator driver hardware and software targeted for support. Items in black are required to be supported, while items in red are desired to be supported.

The operational requirements of the components listed in Table 2.1 dictated the functional specifications of the analog stage for the final form of the PZA driver. Corresponding to the two major categories of PZA, there are two main modes of operation for the PZA driver: harmonic and non-harmonic operation. Though the analog requirements for these two operating modes are very different, they were both successfully accommodated by constructing an amplifier with two operating modes. Harmonic actuators use a high frequency (on the order of 50kHz), sinusoidal driving waveform which throughout this document will be referred to as “High Frequency Mode.” Non-harmonic actuators use a lower frequency driving waveform (on the order of 3kHz) which throughout this document will be referred to as “Low Frequency Mode.” The functional definition of these two operating modes is given below:

1. **Low-Frequency Mode:** Arbitrarily shaped waveforms requiring a throughput of 6 million 10 bit samples per second on 4 independent channels with a range of 0 – 48 volts in order to take advantage of the full resolution of manufacturer provided optimized waveforms. At an operating frequency range

of $150 - 55,000\text{Hz}$, a minimum overall slew rate of $6\text{V}/\mu\text{s}$ is required based on analysis of waveform shape. Minimum current carrying capabilities of 4 amps per channel

2. **High-Frequency Mode:** Sinusoidal waveforms, 2 independent channels, 350 volts RMS maximum, $25 - 75\text{kHz}$ operating frequency, minimum current capabilities of 0.5 amp per channel

While Shinsei ultrasonic motors (Shinsei Corporation, Tokyo, Japan) are targeted for support, the large current requirements of these motors indicated that the initial analog system being driven by OPA549 operational amplifiers may not be sufficiently powerful. As such, preparations have been made to develop and incorporate a higher power secondary amplifier module so as not to overtax the electronics packages.

Final Design

Digital Specifications: While the previous version of the PZA driver, which essentially converted an analog signal into scaled PZA driving signals, relied on an external control computer monitoring feedback systems and generating real time commands, this driver was designed to be significantly more capable. The new PZA driver design shifted from receiving real-time commands to receiving set-point commands and using sensor feedback to execute control loops internally. In addition to this, all four channels were independently generated rather than generating two waveforms and inverting them to create the requisite four. This increase in computational load required a more capable embedded processing architecture. As can be seen in Fig. [2.10](#), an FPGA was added to the design to generate motor driving signals, leaving a microcontroller to administer control loop

operation, communication and distribution of commands. A PIC32 processor was selected for this task to leverage their inherent stability, high operating speeds and simplicity of application. The digital architecture was selected utilizing a decision matrix designed to balance capabilities, assembly cost, and available development tools.

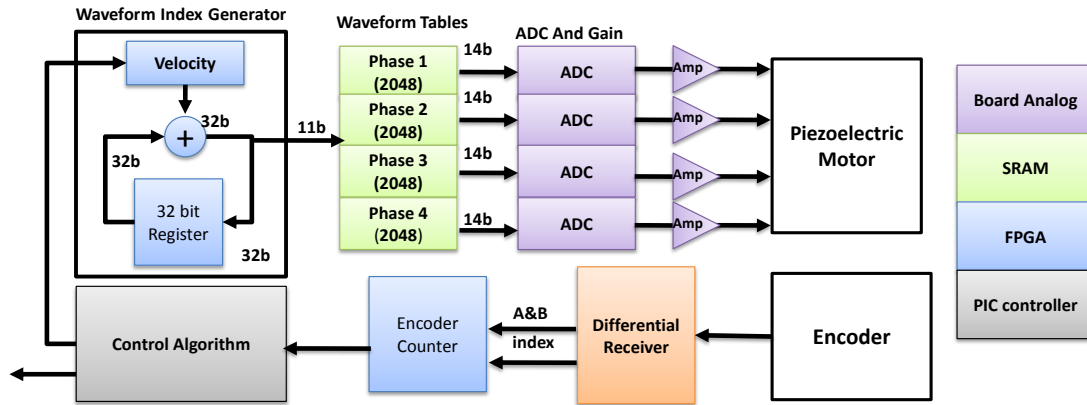


FIGURE 2.10: Architecture of piezoelectric actuator driver. Note the functional allocation legend on the right-hand side.

This functional architecture was combined with the digital communication requirements to develop the current expression of the PCB, which integrates a board-edge connector to easily connect and disconnect to the backplane aggregator, a series of indication LEDs which can be programmed by the user to issue warnings, I/O protection, USB support, and a series of LED numeric outputs to allow the creation and display of status and error codes. A labeled image of this board is shown in Fig. 2.11.

2.4.2 Integrated Infrastructure Enclosure

Whenever an electronic device to be operated within the scanner room is developed, control of EMI is a major concern. As discussed in previous sections, all signal components which could interfere with the scanner are prevented from being transmitted to the in-bore

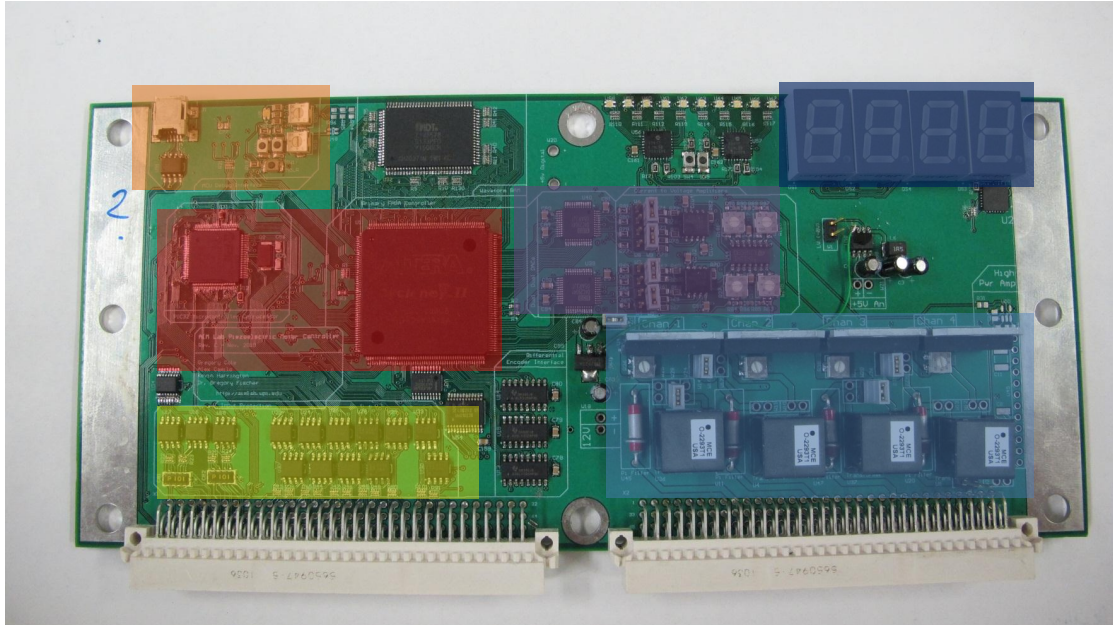


FIGURE 2.11: Current version of the piezoelectric actuator driver. The light blue box is the analog output stage, comprising the linear amplifier stage, transformers, and pi filters; the purple box is the digital-to-analog conversion section with tuning resistors; the dark blue box is LED output; the orange box contains the USB and flash card interfaces; the yellow box is I/O protection circuitry; and the red box is the digital stage.

manipulator, however it is impractical to put this kind of restriction on the digital equipment within the controller box. To enable the operation of digital processing hardware within the scanner room, a method of containing electrical noise generated by this equipment was required, expressed in this system as a Faraday cage. While in many previous systems, the Faraday cage was a simple conductive enclosure, experience demonstrated that certain support equipment, such as power supplies, communications devices and penetrations, should be permanently integrated into the enclosure to streamline the development of new devices. The progression of prototypes which lead to this knowledge is shown in Fig. 2.12. This section details not only the Faraday enclosure itself, but also the placement and coordination within it of crucial infrastructure support equipment.

Initial prototypes were little more than COTS aluminum boxes with

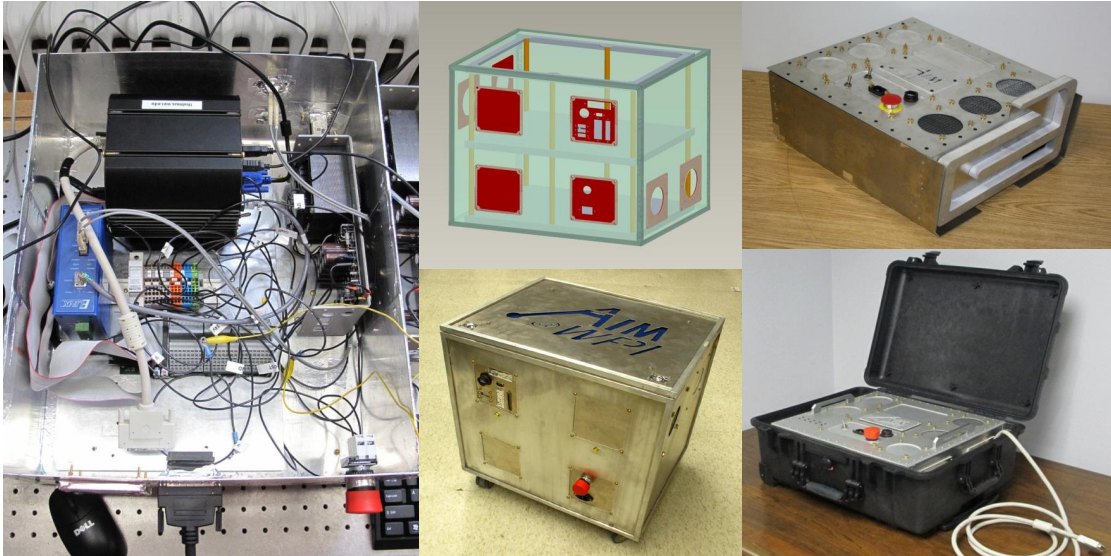


FIGURE 2.12: Progression of prototype Faraday enclosures. Far Left: simple aluminum box with hand-cut bulkhead connections sealed with shielding tape. Center: First modular Faraday enclosure featuring wheels for transportation. Right Bottom: First prototype of final revision of enclosure. Lid is not permanently attached to enclosure, and serpentine penetration is too narrow to be effectively utilized. Right Top: Final prototype of Faraday enclosure. Note hinged lid and wide serpentine.

patch panel holes cut into the sides and sealed with EMI shielding tape. Soon, however, it became clear that a more permanent solution was required in order to allow the unit to be opened and closed regularly, which necessitated the design of a constructed unit.

2.4.2.1 First Prototype Modular Enclosure

This modular system was designed to accommodate components capable of being easily reconfigured for a variety of projects, so the enclosure was designed as a two-tiered removable equipment rack with swappable interface plates, as shown in Fig. 2.13.

This unit was developed before the restructuring of the total system, as it was still targeted to contain the control computer within the scanner room. This prototype was designed to use a removable equipment rack to enable easy modification of internal components,

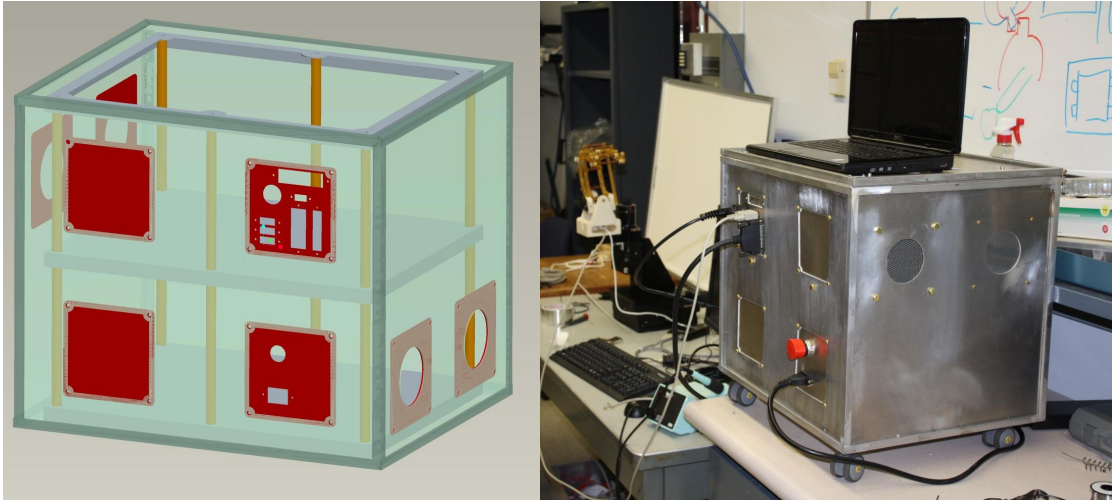


FIGURE 2.13: Left: Transparent model of first modular Faraday enclosure depicting modular patch panels and two-tiered removable equipment rack. Right: Photograph of prototype enclosure, operating an early prototype of the stereotactic neural intervention device. Note the MRI-compatible caster wheels, emergency stop, and bulkhead connectors.

modular patch panels to allow for new interfaces to be rapidly integrated, as well as a hinged lid and wheels to make transportation and on-site access easier. Unfortunately, the ergonomic aspects for this design were not as convenient as was initially thought. The hand clearance between the storage rack and the wall was insufficient, making removal of the equipment rack difficult. Though the modular patch panels were relatively easy to remove, they still required custom machining to construct which was inconvenient and costly. In addition to this, the two layer nature of the equipment rack virtually required its removal to perform any significant modification of the control system. This in turn necessitated the removal of all modular patch panels as they contained connections to the equipment contained within the rack. Finally, the entire enclosure was constructed of 24 gauge aluminum which was stiff enough to be structurally sound, however flexible to the point that the seams between the patch panels, sidewalls and lid developed gaps over time, allowing EMI to leak out. This in turn required that all seams be

sealed with EMI shielding tape. Analysis of its deficiencies yielded the final design requirements as follows:

1. There will be only one tier of equipment, such that all components can be accessed without being removed.
2. Tools will not be required to interchange shielded penetrations.
3. Wiring will be minimized.
4. Transportation ergonomics and ruggedization will be similar to carry-on luggage.

While previous iterations of this design were approached as prototypes, the design of this version began during the restructuring of the system architecture and was targeted to be a production ready, final design. Though detailed discussions of design requirements follow, the driving requirement for this unit was ease of use. Primary difficulties in previous systems involved transportation, robustness, and modularity. The final version is intended to be easily transported and set up by a single person, small enough to be taken as airline carry-on luggage and robust enough to withstand air transportation. Finally, the system is targeted to be easily reconfigured, such that electronic modules within the controller can be exchanged with minimal effort and basic hand tools capable of being stored within the unit itself. In addition, while many components of the control system and their mounting within the enclosure were modified to be more easily and repeatably replaced, some components of the system are required to support core functionality. These components are permanently integrated into the final enclosure design. The combination of these permanently integrated infrastructure components, specialized

ruggedization, and unique cable penetration method yields a final component that represents a significant contribution towards the development and deployment of MRI-compatible mechatronic systems.

2.4.2.2 Final Module Concept

The final implementation of the modular MRI-compatible device development system leverages an equipment enclosure with integrated infrastructure support. Previous iterations of the system have revealed several components that were identified as essential to the operation of the system modules, and as such were targeted for this permanent integration with the Faraday cage. Basic functions of the control system will be supported by the following devices:

1. Backplane signal aggregator
2. 48-volt linear regulator
3. 12 V and 5 V switching regulators
4. Fiber optic media converter
5. Serpentine penetration
6. Wiring harness pigtail

While the electrical and software interfaces between these components is very straightforward, great care and testing was undertaken to ensure proper mechanical construction. Through personal experience and communication with our collaborators, it was understood that the control packages to be developed were required to travel not only between the laboratory where they were under development

and a scanner room, but also over larger distances to run experiments with other collaborators. In order to facilitate dissemination of this equipment to a larger audience and ease transportation between remote sites, the new enclosure was designed not only to be highly ruggedized, but also to fit within the maximum allowable size for commercial airline carry-on, as required by the Transport Safety Authority. As shown in Fig. 2.14, the final enclosure was targeted to fit within a Pelican (Pelican Case Corporation, San Antonio, TX) 1560 hard shell travel case, which is itself the maximum allowable size of airline carry-on luggage.

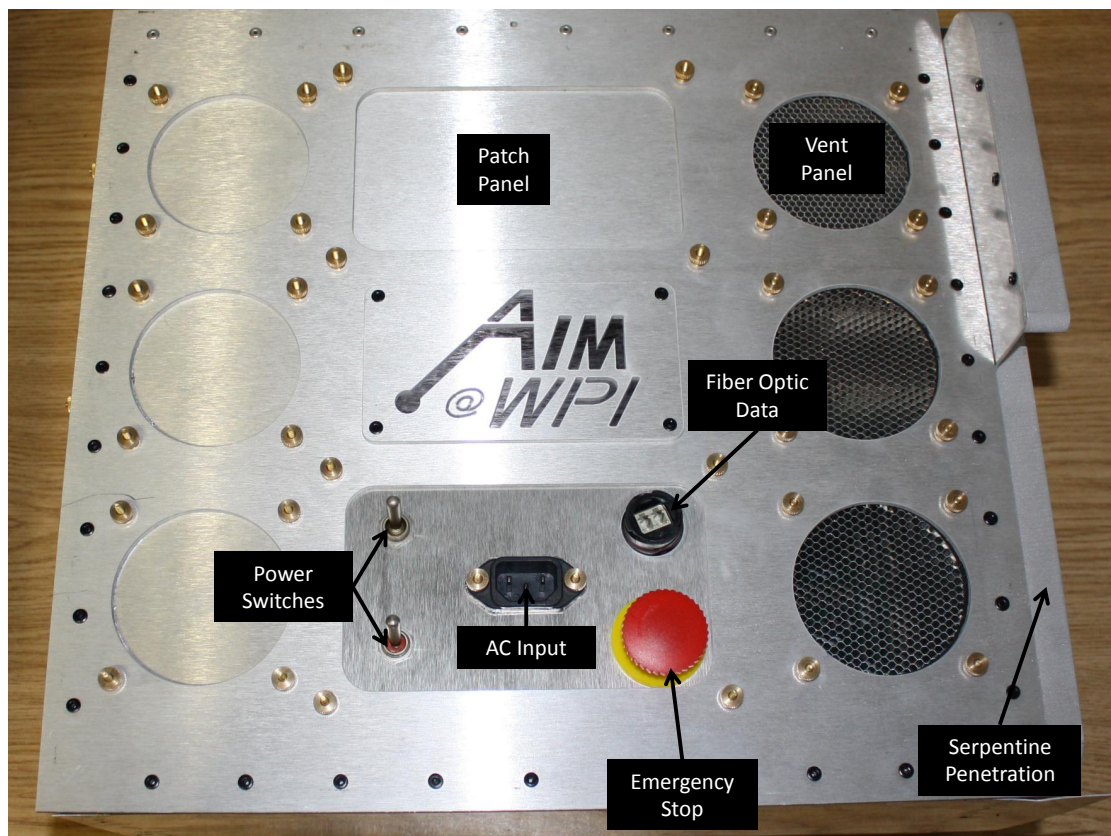


FIGURE 2.14: Top of Faraday enclosure with penetrations and surface components labeled. Interior component placement of the system modules is given in Fig. 2.6.

Ergonomics, Weight Distribution, and Ruggedization In order to make transportation of the equipment as comfortable and safe as possible,

weight was distributed such that the center of gravity was placed 4 inches away from the center toward the wheels. This allowed for the case to be stable when standing on end and reduced vibration in the heaviest components when rolling over uneven terrain while still allowing a comfortable feel when lifted with the side handle. Though no formal testing was performed to determine levels of shock transferred to components within the case during motion and transportation, the distribution of weight throughout the case was measured, and the case was tested for durability. It was tested by being rolled for extended periods of time over different surfaces — including sidewalk, smooth asphalt, rough asphalt (roads, old parking lots), grass, gravel, smooth concrete with dividers, indoor surfaces and surface transitions (elevator gaps, doorjambs, etc.) — to determine if connections were loosened or subcircuits dislodged. The case was actively rolled over each surface at a pace of approximately 4 miles per hour for a minimum of 20 minutes, as well as each interior transition being rolled over at a similar velocity for a minimum of 200 iterations. Had damage, loose connections, or dislodged components been observed, deeper investigation into the forces involved or the damage caused would have been needed. Since the system showed no negative effects from this test, other, more pressing areas were investigated.

RF Shielding and Attenuation Experience has shown that implementing designs which necessitate RF shielding tape require increasing amounts of tape, while becoming less effectively shielded with each application. In order to circumvent this permanently, a hardware package that was truly reconfigurable but requiring no additional machining or patching was desired. To address equipment

access, a hinged lid with a shielding lip was implemented, such that the contour of the lip would encourage continuous contact about the entire border of the case, as depicted in Fig. 2.15.

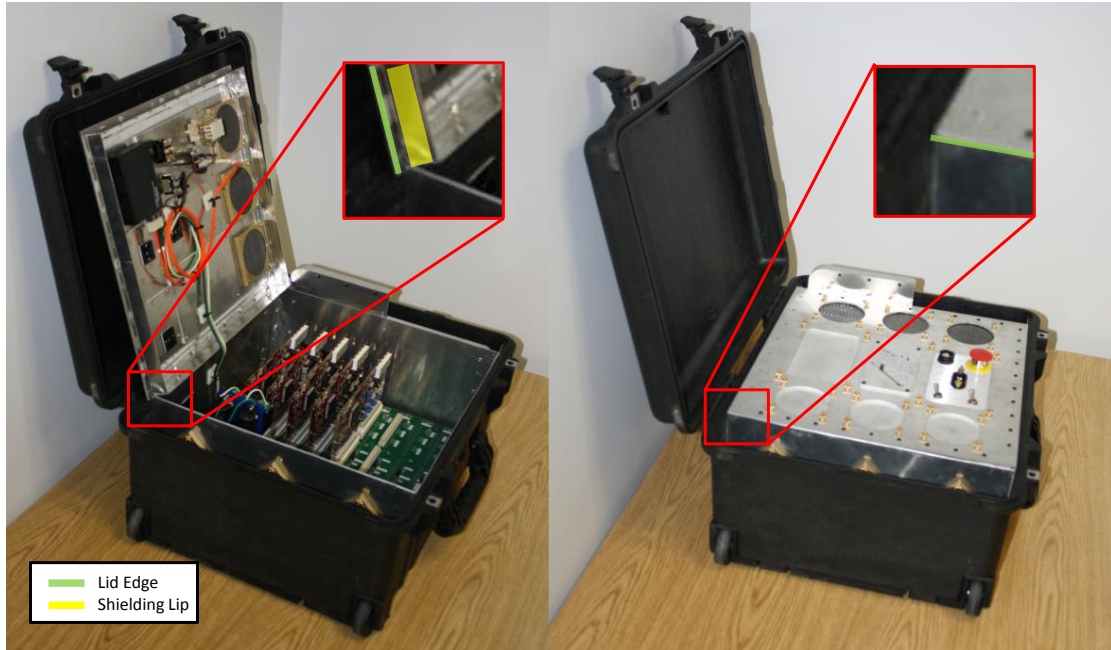


FIGURE 2.15: Depiction of location of shielding lip and its interaction with the side panel of the equipment enclosure. Note how on the left inset the 0.75 inch tall shielding lip is seen protruding from the bottom of the edge of the lid, while on the right inset, it is clear that the lid edge is flush with the sidewall, indicating the shielding lip is parallel to, and pressed against the side wall on the interior of the enclosure.

While the majority of the development of the Faraday cage was fairly straightforward from previous experience and experimental validation, the issue of creating a tool-less, reconfigurable penetration remained unsolved. Shielded bulkhead connectors are traditionally utilized in this situation. But this system was designed to be a development platform used by many people so the time and expense required to create a new shielded bulkhead for each new cable penetration needed was prohibitive. Although creating standard cable penetration “blanks” was discussed, this would indicate that all cables penetrating the enclosure would require a shielded head termination, and only the terminations originally machined into the

blanks would be usable. This seemed as though it would stifle rapid proof-of-concept experimentation, so a penetration without a predetermined connector was desired. The selected concept for this design was a serpentine guide through which cables could be routed without the use of any connector. To ensure that EMI could not escape from within the controller enclosure, this serpentine bulkhead penetration was designed as a waveguide. Classically, waveguides have been designed to maximize transferral of desired frequencies through them. However, the equations developed characterizing waveguide design were used to ensure that the serpentine penetration would **block** the transmission of all EMI which could be detected by the scanner. Since the standard sensitivity of many diagnostic MRI machines is in the area of approximately 1 MHz to 300MHz (as the most common resonant frequency for diagnostic scanners at this point is 1.5, 3, and 7 Tesla), the serpentine penetration was designed to suppress all frequencies below 600 MHz. Waveguides can operate with many modes, each corresponding to different methods of transferring energy through them. To ensure that all frequencies to which an MRI is sensitive are suppressed through shifting the lowest cutoff frequency of the waveguide above the highest reception frequency of the scanner, only the cutoff frequency of the $m = n = 1$ mode needs to be considered, as the cutoff frequencies for all higher modes will be higher. The equation, as presented in [69], for a rectangular waveguide cutoff frequency is

$$f_{cutoff} = \frac{c}{2\sqrt{\epsilon\mu}} \sqrt{\left(\frac{m}{a}\right)^2 + \left(\frac{n}{b}\right)^2} \quad (2.1)$$

where ϵ and μ are the permittivity and permeability, respectively, of the material within the waveguide (air in this case, meaning $\epsilon =$

$\mu = 1$), c is the speed of light, and a and b are the dimensions of the rectangular cross section of the waveguide channel, utilizing meter-second SI units. Since the minimum cutoff frequency is sought, only the first mode is considered, and thus $m = n = 1$. Additionally, a minimum cutoff frequency of $f_{cutoff} = 600,000,000$ is desired, so substituting, simplifying, and defining as an inequality yields the following:

$$(600MHz) < \frac{c}{2\sqrt{1}} \sqrt{\left(\frac{1}{a}\right)^2 + \left(\frac{1}{b}\right)^2} \quad (2.2)$$

$$\left(\frac{(600MHz)2}{c}\right)^2 < \left(\frac{1}{a^2}\right) + \left(\frac{1}{b^2}\right) \quad (2.3)$$

$$16.022 < \left(\frac{1}{a^2}\right) + \left(\frac{1}{b^2}\right) \quad (2.4)$$

Once this relationship was determined, the diameter, bending radius, and number of cables which were required to be run out of the penetration were calculated, so that minimum requirements for both cross sectional area and linear dimensions of the rectangular guide could be determined. Allowing for all of the currently designed wiring harnesses to be passed through the waveguide with a safety factor of 3, it was determined that a $4cm \times 2cm$ waveguide would allow all cables to penetrate while leaving a reasonable margin for future cabling being developed. Substituting this into equation 2.4, we see that in fact this cross section does satisfy our requirements; substituting into equation 2.1, the cutoff frequencies of the individual waveguide sections are found to be $6.97GHz$ and $7.08GHz$. Additionally, the walls of the waveguide were set to be at

least 2.25cm wide, giving the serpentine a broad area of contact to ensure that additional open pathways for radiation are not formed through gaps between the conductive cover and the waveguide itself. Final design of the waveguide is shown in Fig 2.16.

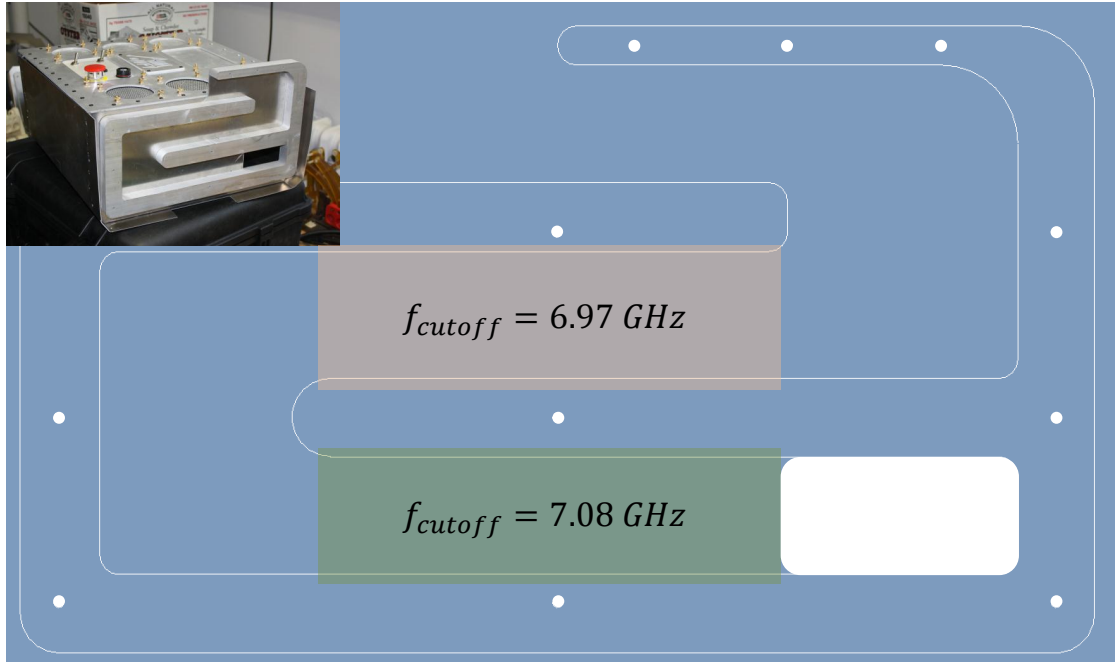


FIGURE 2.16: Serpentine enclosure penetration with two functional waveguide sections identified. Inset: photograph of waveguide. Note the broad edges on the serpentine designed to ensure an uninterrupted line of contact between the serpentine and the serpentine cap.

2.4.3 Backplane & Signal Aggregator

To improve the physical ruggedness of the system as a whole while simultaneously reducing cabling and communication complications, a backplane signal aggregator was developed. This aggregator managed the flow of all signals moving through the scanner room controller, as well as providing a convenient method of combining all communication pathways from the interface box and control computer to the scanner room controller into one ethernet connection. Communication signals are aggregated via an embedded microcontroller. The majority of the backplane's physical presence serves to

bundle the majority of electrical connections between components within the controller into a convenient and robust printed circuit board. The current backplane supports 8 PZA drivers, whose connections to equipment outside of the controller box are distributed via 2 VHDCI SCSI 68-pin compact, shielded, twisted pair cables, which were chosen for their compact layout and commercial availability. While this is the current expression of the aggregator, the processing and communication section of the board has been developed with a modular interface, allowing for unique backplanes capable of supporting project-specific arrangements of hardware modules easily. In addition to the cross-connection of system hardware modules, and concatenation of I/O signals, the current backplane also manages power filtering and distribution, as well as software control of power supply switching. The backplane signal aggregator is shown in Fig. 2.17, with relevant sections highlighted.

2.4.4 Power Supply

In the design of any electronic device, especially one as complicated as a motion control system, application of voltage shifting devices in the form of power supplies is nearly unavoidable. Currently, there are two main architectures used for converting one DC voltage level to another, linear and switching regulators. In general, switching regulators tend to be smaller, less expensive, more reliable, and much more efficient. However by nature of their design, their output contains high frequency electronic artifacts. While these artifacts are generally of a very low amplitude and are suitable for a majority of modern applications, the noise artifacts generated by switching regulators is highly disruptive to an MRI scanner. Many groups

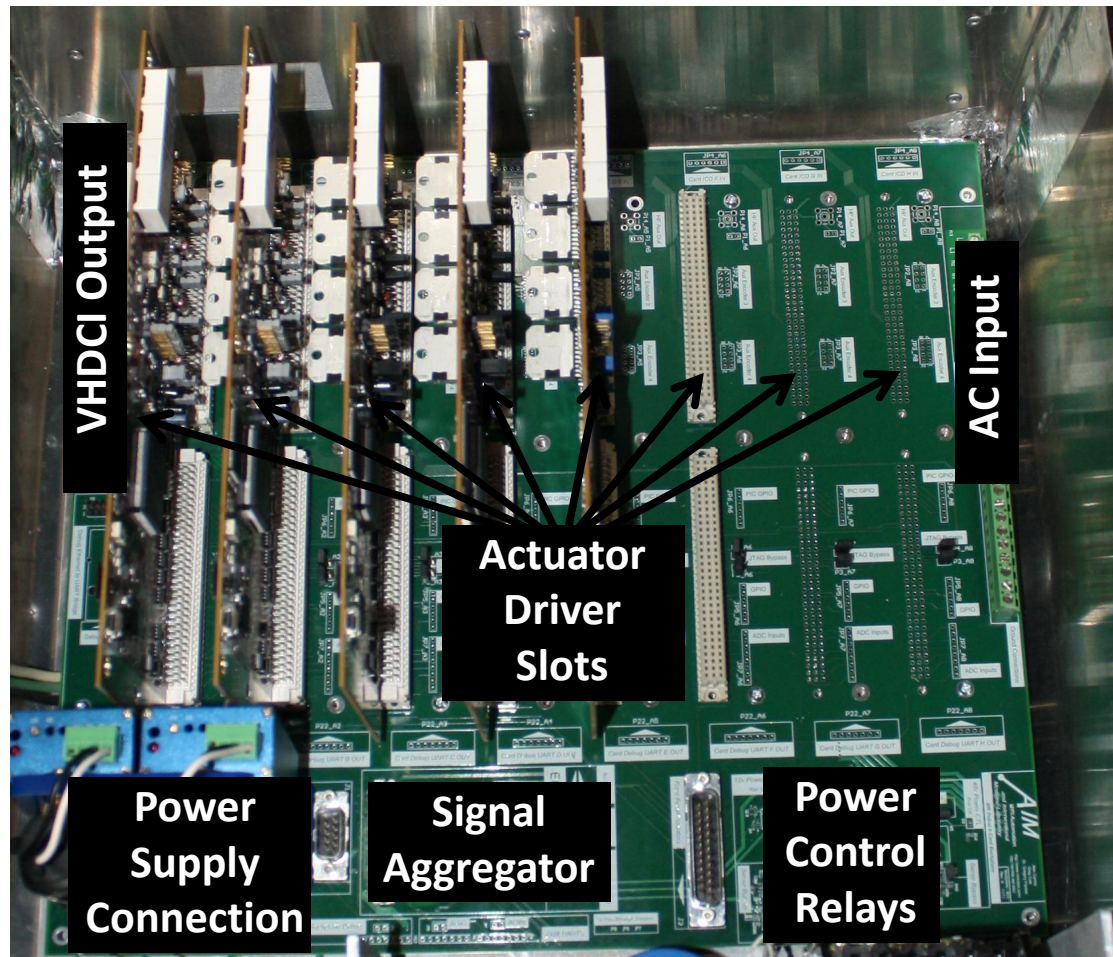


FIGURE 2.17: Backplane signal aggregator with relevant sections highlighted and labeled. Note how all of the electrical connections within the scanner room controller are routed through the backplane for transparency, simplicity, and control.

endeavoring to create MRI-compatible mechatronics opt to use linear style regulators, locate high precision switching regulators outside of the scanner room and pass the DC power through the patch panel, or even operate their equipment from batteries, all to avoid using switching regulators within the scanner room. Though saving power is not generally of concern in a hospital setting on a scale such as this, generation of excess heat quickly complicates the development of any integrated electronic system. In addition, variable high-efficiency MRI-compatible switching power supplies would greatly

expand design capabilities for MR guided mechatronics, and characterizing methods for their construction represented a significant contribution. Though the switching frequency, and hence the frequency of interference generated by these devices, is often below the detection bandwidth of the scanner, the noise is emitted in the form of a triangle wave which has higher frequency components. These components can be expressed with this infinite Fourier series:

$$\sum_{n=0}^{\infty} \frac{1}{\pi n} \sin 2\pi n t f \quad (2.5)$$

where n is the number of the subcomponent and f is the frequency of the sawtooth wave. In the proposed architecture, a medical-grade linear AC-DC converter generates 48 VDC from the in-room AC supply, which will be stepped down to other required voltage levels via custom switching regulators. While there are many nuances to power electronic design, the first step in the process is to understand the operating constraints which are acceptable. The driving constraint for this design bringing the noise emitted from the regulator down to an acceptable level so as not to interfere with scanner operation. While the majority of the EMI radiated from the device will be contained by the equipment enclosure, the voltage rails supplied by it will be passed out of the control box and used to power sensors and periphery devices placed within the scanner bore. Because of this, design of the regulator will be guided by reducing the output noise, or “ripple voltage”, to an acceptable level.

2.4.4.1 Driving Design Parameters with EMI Properties

In order to properly determine appropriate performance benchmarks for the new power supply design, it was necessary to understand the types of noise to which the scanner is sensitive. Any MRIs' receive system is design to interpret a narrow range of frequencies centered about the resonance frequency of the scanner. The Larmor equation defines the relationship between the field strength of the scanner and the resonant frequency, as seen below:

$$\omega_0 = \gamma\beta_0 \quad (2.6)$$

where ω_0 is the resonant frequency, γ is the gyromagnetic ratio, which is unique and specific to every atom, and β_0 is the strength of the magnetic field. Since MRIs' analyze the motion of hydrogen atoms, the gyromagnetic ratio of hydrogen, 42.56 MHz/Tesla, is used in the Larmor equation to determine the resonant frequency of a scanner in terms of the field strength of that scanner [70]. It was postulated that by ensuring all signals emitted within the MRIs' detection range were below a detectable amplitude, scanner interference could be avoided. Because the noise generated by switching power supplies contains subcomponents of an infinite number of higher frequency components, a logical choice would be to push all frequencies of noise generated by the electronics above the scanner detectable range, ensuring no signals possibly detectable by the scanner were emitted. A study of the progression of scanner development indicated this was not the case as higher static field strength provides higher resolution and contrast[71]. Currently the development of 7 and 9.4 Tesla systems for clinical use are nearing completion. A 7

Tesla scanner would have a resonant frequency of 300 MHz, with a detection range extending to even higher frequencies. Because the costs and time required to develop power supply systems operating at that frequency range was prohibitive, the focus of the project was turned to creating a design for which all frequency subcomponents in a scanner's detection range could be removed via filtration. One tenth of the resonant frequency of the lowest field, commonly used clinical scanner was targeted to be the cutoff frequency for the noise components. Since the lowest field strength, commonly used clinical scanner found was 0.05 Tesla, the cutoff frequency target was derived using the Larmor equation:

$$\omega_0 = \gamma\beta_0 \quad (2.7)$$

$$\omega_0 = 42.56 \frac{MHz}{Tesla} \times 0.05 Tesla \quad (2.8)$$

$$\omega_0 = 2.128 MHz \quad (2.9)$$

Yielding a cutoff frequency of approximately 200 kHz. Motivated by reducing the heat generation by the system as a whole, the maximum energy dissipated by the filters was targeted to be 0.1 watts, under largest possible continuous load. Since this power supply is targeted to be capable of providing a continuous current of 20 Amps at 5 Volts (corresponding to the electrical demands of device consuming the most energy in the controller, the embedded computer in the initial control system design), this energy dissipation level limits the voltage level of filtered noise to 5 millivolts. Inspection of the general form of a component of a sawtooth wave indicates that as the base frequency is driven lower, the rippled voltage is divided by a larger

value of n to give the amplitude of such a subcomponent. Combining these restrictions, with the definition of the subcomponents of a sawtooth wave, a relationship between maximum switching frequency and ripple voltage level can be derived, as shown below:

$$\sum_{n=0}^{\infty} \frac{V_r}{\pi n} \sin 2\pi n t f \quad (2.10)$$

where the component magnitude diminishes with the frequency as can be seen in Fig. 2.18, and is expressed and solved for n as:

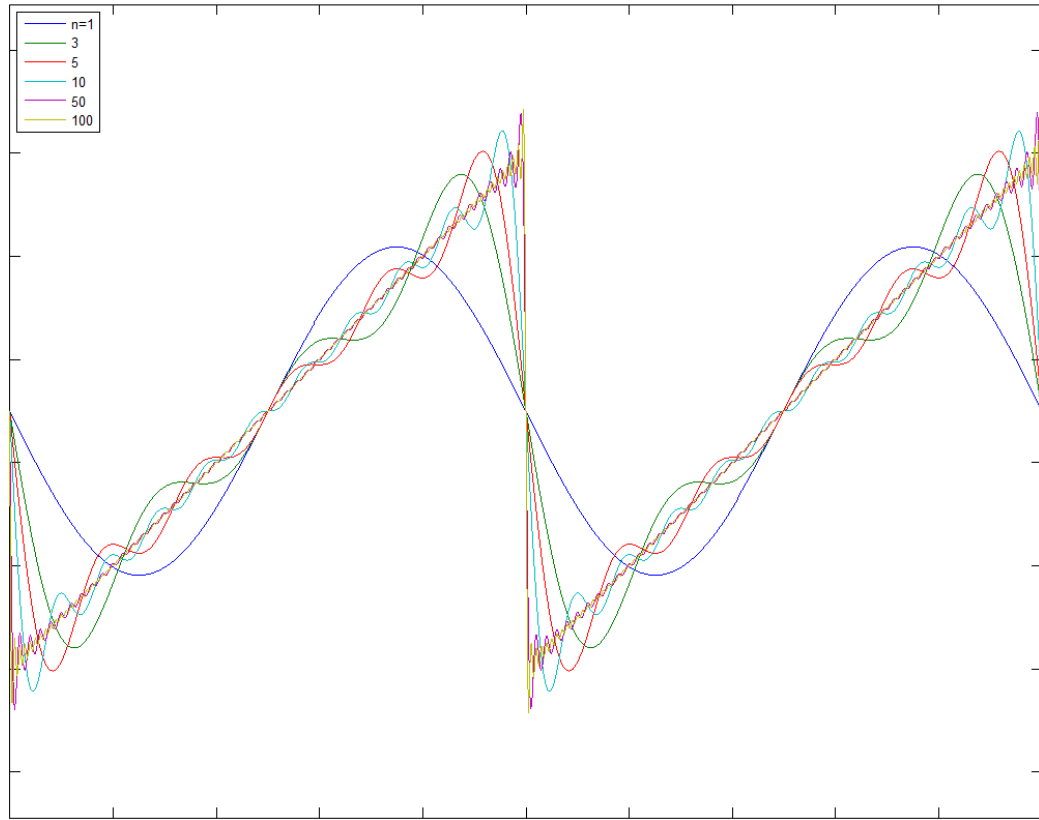


FIGURE 2.18: Depiction of a sawtooth wave and the diminishing amplitudes of its subcomponents.

$$\frac{V_r}{\pi n} = 5mV \quad (2.11)$$

$$\frac{V_r}{\pi 5mV} = n \quad (2.12)$$

and the frequency is expressed and solved for n as:

$$\pi 2nf = 200kHz \quad (2.13)$$

$$\frac{200kHz}{\pi 2f} = n \quad (2.14)$$

These two equations can then be set equal to each other in the following manner, and be reduced to a relationship between the ripple voltage, frequency, and a constant.

$$\frac{200kHz}{\pi 2f} = \frac{V_r}{\pi 5mV} \quad (2.15)$$

$$\frac{200kHz 5mV}{2} = V_r f \quad (2.16)$$

$$500 = V_r f \quad (2.17)$$

This equation indicated that with a targeted maximum ripple voltage of 10 mV, an acceptable switching frequency would be a maximum of 50 kHz. In order to maintain an additional safety factor, initially a switching frequency of 25 kHz was targeted. This switching frequency is far below the average switching frequency of most COTS switching regulators, so a custom regulator was developed. The low frequency necessitate, high value primary components with large amounts of energy storage to accommodate the high current operation targeted for the device. Initially, simulation was used to refine the design of the power supply, as will be discussed in the coming sections.

2.4.4.2 Synchronous Operating Principles and Analysis

To determine the best architecture for the power supply, the most common switching regulator architectures were modeled using LT-Spice (Linear Technologies, Milpitas, CA) to simulate their performance operating within the defined parameters. Once the models were stabilized, the synchronous buck architecture demonstrated the highest efficiency under all of our targeted operating conditions, an important factor when considering the difficulty of implementing cooling systems in this environment. The architecture of a synchronous buck converter is shown in Fig. 2.19.

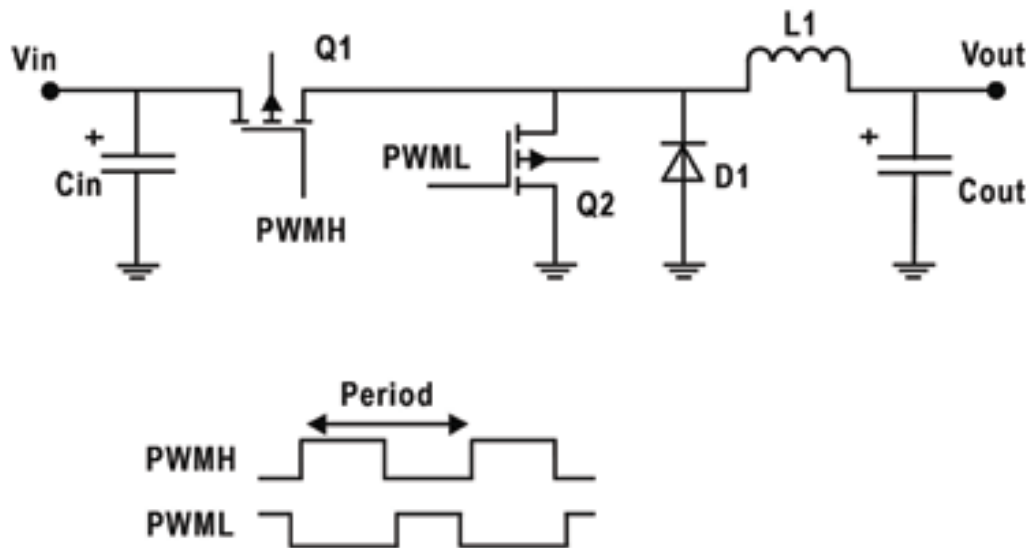


FIGURE 2.19: Basic architecture of a synchronous buck converter. Note the diode used to clamp the voltage and the MOSFETs used to relieve the current-carrying load of the diode so that the device can operate more efficiently. This figure taken from Dumais [72]

Once the synchronous buck architecture was selected, component specification and modeling began. Due to the limited availability of very low-frequency programmable buck-boost controllers on the market, a semi-obsolete controller, the *LT1339* (Linear Technologies,

Milpitas, CA), was selected. Initially, the basic values for component specifications were derived utilizing the following conditions:

1. Must have total output ripple voltage under $2mV$
2. Must be at least 85% efficient
3. Must be no larger than 1.5" X 3" X 5" in size
4. Must be stable at no load and always operate in continuous conduction mode
5. Must not vary output average load voltage in response to load changes of more than 5% of targeted output voltage
6. Must not overshoot output voltage on startup by more than 1 volt
7. Must maintain maximum amplitude on all components of output ripple voltage over $200kHz$ in frequency at under $0.01mV$ in amplitude
8. $12 \text{ volts} < V_i < 60$
9. $1 \text{ volt} < V_o$

By conforming to these guidelines, not only will a single power supply design be capable of supporting a wide variety of applications that could be developed for new system devices, but they could also be utilized to generate all required power rails for the current system, while contributing less heat, weight, and cost than purchasing linear power supplies. To achieve these goals, equations governing the operation of buck-boost converters were used to derive the initial model for the converter, shown in Fig. [2.21](#).

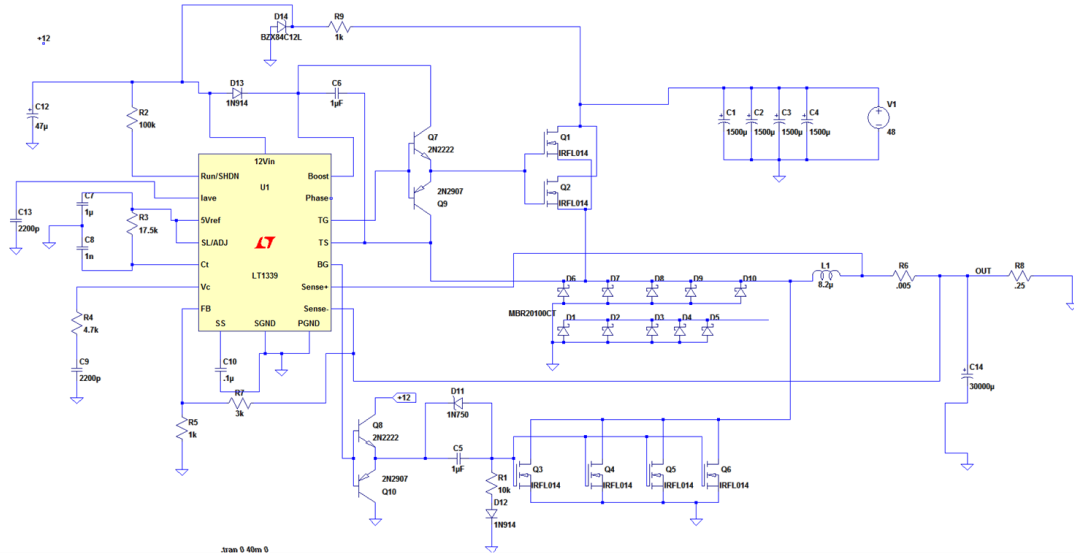


FIGURE 2.20: Schematic of proposed power supply shown in LTSpice. Note that all components are modeled utilizing SPICE models of actual components and no ideal devices.

Note the relatively large values for the output capacitance ($150,000\mu F$) and inductance ($32,000\mu H$) as compared to a standard high-frequency 20 – amp switching regulator, which would have component values an order of magnitude smaller. The low switching frequency required for the operation of this device necessitates component values which store a great deal of additional energy in order to maintain the desired output voltage level. Also note how the high current-low frequency operation required the use of multiple high current diodes and MOSFETs to support the current being run through this system. This design was analyzed using entirely model-based components, as opposed to using ideal components, to ensure a more accurate analysis. Furthermore, this model was analyzed in terms of current consumption, startup time, and ripple voltage output for voltage output levels between 1volt and 90volts to ensure it would behave in a similar fashion over the entire operating range. A selection of plots for the conversion of 48volts to 5volts is shown below in Fig. 2.21.

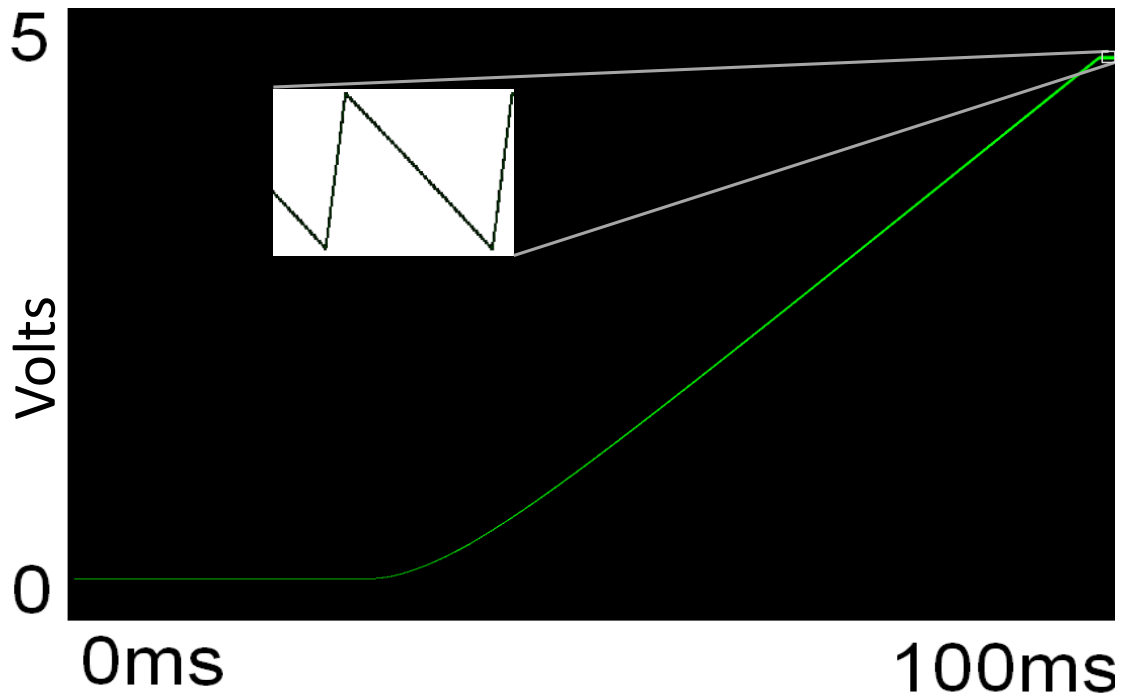


FIGURE 2.21: Simulated startup transient of the proposed power supply. Note how ripple voltage is contained to less than 2mV, and voltage overshoot on startup is less than 0.025 volts.

While LTSpice does not allow for modification of circuit state during an analysis, it does allow saving the state of an analysis, modifying the value of a component in the schematic, then continuing the analysis based on the updated component value. This method was utilized to simulate dynamic loading of the power supply to ensure both that the power supply would remain safe in its output voltage as well as produce no image-degrading noise. The results of these simulations confirmed the stability of the power supply over the operating range desired, so with design and construction proceeded.

2.4.4.3 Physical Construction and Testing

The schematic for this power supply was transferred to Altium Designer (Altium Limited, Belrose Australia), which was then used to

design a printed circuit board, shown in Fig. 2.23. This power supply was constructed and tested using a simulated load, such that its performance could be analyzed before it was used to power the rest of the system components. The prototype unit is also shown in Fig. 2.23. Once construction was completed, the power supply performed as designed and was installed in an aluminum enclosure within the scanner equipment system. The regulator was successfully integrated with the control system.

Initial compatibility tests indicated the power supply was performing as designed and caused very little noise when operated during imaging. This unit operated the system for an extended period of time. Before the system was returned to the scanner for a formal test of the power supply's compatibility, however, the power supply was accidentally damaged beyond repair. At this point, the knowledge gained from modeling, analyzing, and testing the unit drove the creation of a new power supply system, which represents the final form of the power supply system module.

2.4.4.4 Final Power Supply Implementation

The power supply system failure occurred during the architecture redesign, and as such the specifications for creating a new power supply changed significantly. In the new architecture, the control computer is moved from the in-room controller to the interface unit which resides in the scanner control room, reducing the demand for regulated 5 volt power under MR conditions from 100 watts to 5 watts. Because component selection at this power range is much broader, a switching regulator which operated at the required switching frequency could be sourced. However, it required the addition of a

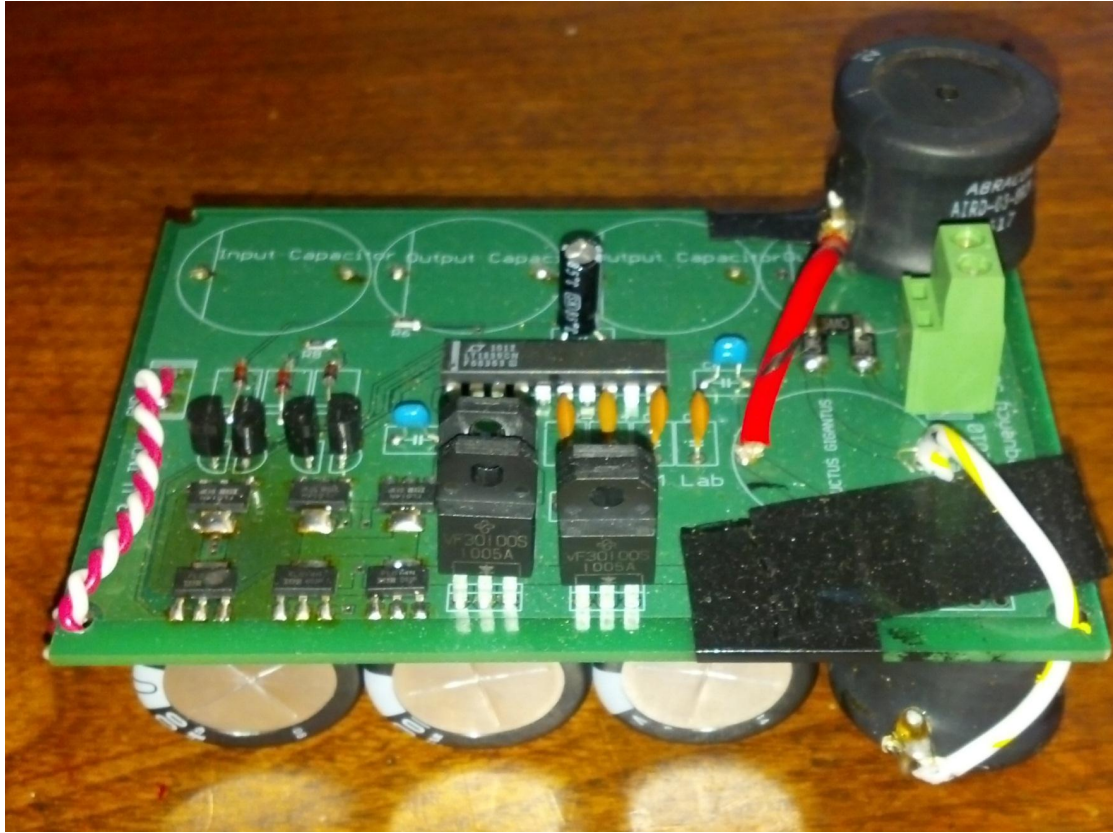


FIGURE 2.22: Prototype of switching regulator. Note the three 50,000 μF capacitors and 36,000 μH inductor array. The discoloration around the transistors comes from a flux paste, not heat damage as it may appear.

filtration module to bring the output noise within acceptable ranges. The lessons learned through the development of the switching regulator drove the design of the filtration modules that would be attached to the COTS power supplies such that their output would be suitable for use in an MRI. By adding a tuned inductor-capacitor-resistor (LCR) network to the converter, the output ripple voltage can be reduced dramatically by acting as a filtering and energy storage system, stabilizing the output voltage even under varying current demands, as can be seen in Fig. 2.23.

Once these filtration modules were constructed, the operation of the total power supply system was first analyzed using a dynamic load cell to verify its operating properties before connecting it to the control system. As can be seen in Fig. 2.24, the power supply

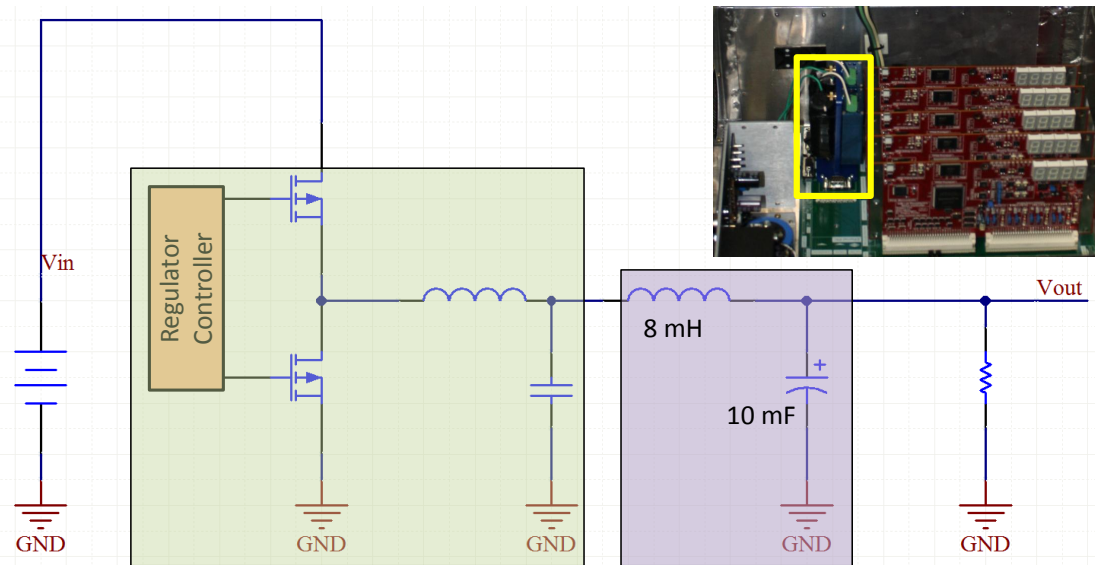


FIGURE 2.23: Schematic of an off-the-shelf switching regulator (green) and the added filtering circuit (purple). Note that the output voltage of the filter is no longer maintained by the power supply, and under small enough loads will creep downwards as the inductor saturates. Inset: Power supply unit installation location.

alone has an appropriate switching frequency, however the amplitude of the ripple voltage is far higher than the derived specifications. Addition of the external filtration modules successfully brings the ripple voltage into the acceptable range. The supply was tested for performance under dynamic operating conditions, and was shown to not deviate from the ideal voltage output range for more than 5 ms, even with the addition and disconnection of large loads. At this point the supply system was integrated with the control system.

2.4.5 Console Room Interface Unit

For the system architecture, the four major hardware components of this system are the robotic manipulator, scanner room controller, console room interface unit, and user workstation: an architecture selected to isolate functional responsibilities of the system to individual components.

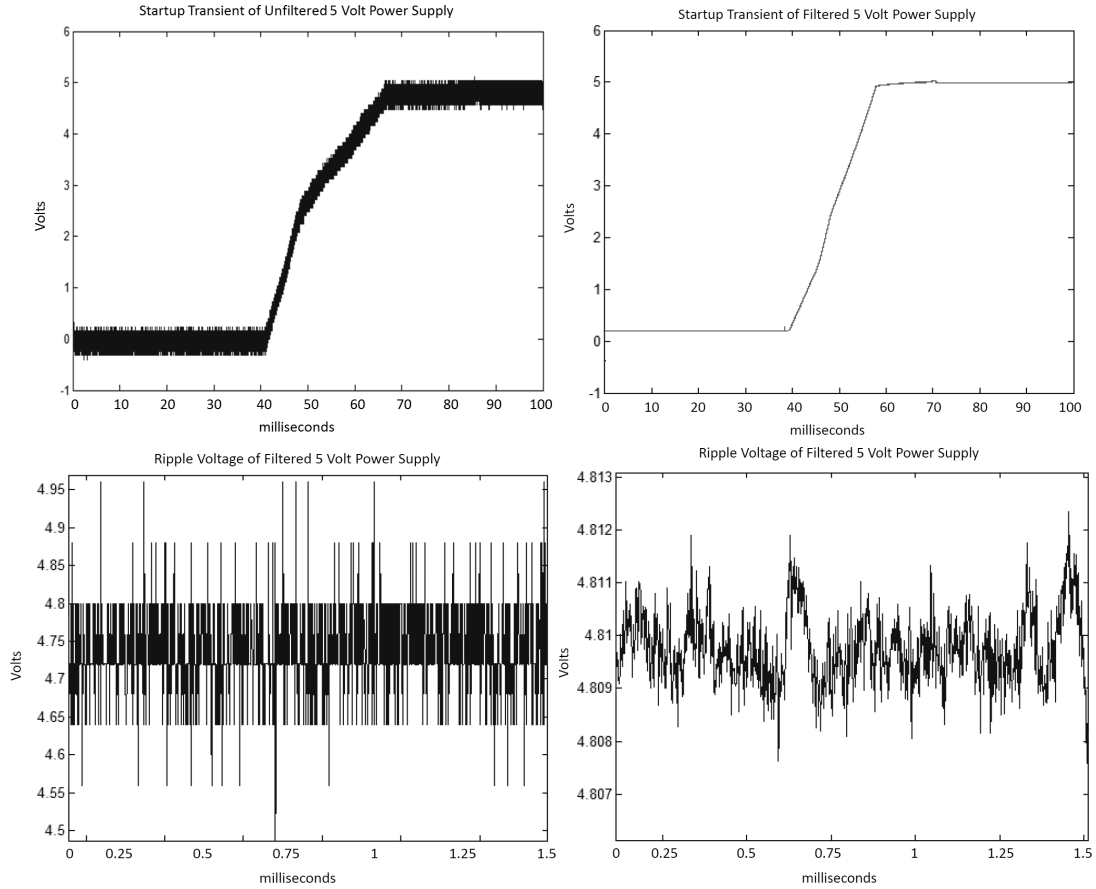


FIGURE 2.24: Left top: Startup transient of 5-volt unmodified switching regulator. Left bottom: Ripple voltage of unmodified switching regulator. Note how the ripple voltage amplitude is over 0.5 volt. Right top: Startup transient of modified switching power supply. Right bottom: Ripple voltage of modified switching power supply. Note how the ripple voltage is now less than 0.004 volt.

The scanner room controller receives joint-level commands, operates actuator and sensing devices, and executes all real-time processing.

The user workstation operates navigation software and generates targeting commands in patient coordinates.

The console room interface unit serves as an intermediary between these two units, converting electrical and fiber optic communication signals, as well as calculating forward and inverse kinematics and device registration, as described by Su *et al.*[5]. This essentially allows the interface unit computer to act as a translator, resolving

patient-space target commands to joint-level commands. The interface unit which houses the control computer and ethernet converter is comprised entirely of COTS devices, and is shown in Fig. 2.25

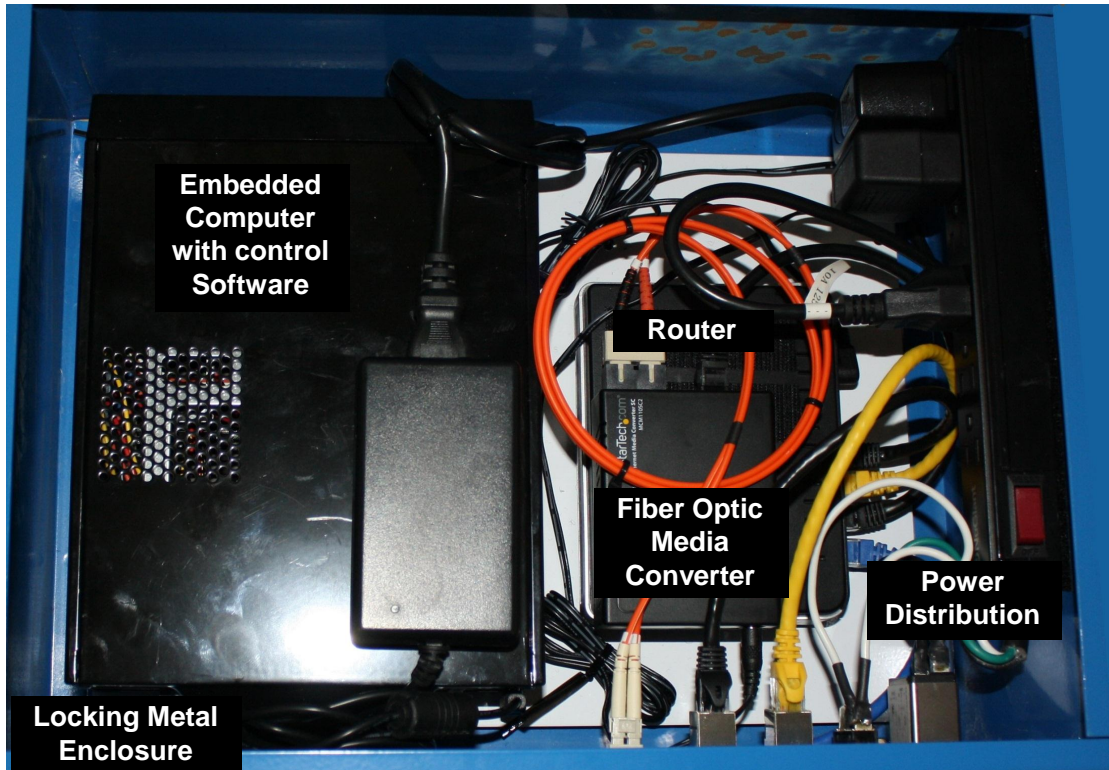


FIGURE 2.25: Interface unit with cover open, identifying control computer, media converter, and power distribution. Inset: connections on the front of the interface unit.

2.5 Experimental Validation

2.5.1 MRI Compatibility Evaluation

To date, there have been a series of experiments with this system, mainly focusing on the ability of the system to generate and control motion while remaining MRI-compatible. All of the modules presented earlier have been tested individually and as an integrated whole to ensure that no aspect of the system creates an unacceptable amount of image interference. The specific scan protocols are

the same as in [67]. The metric of choice to measure signal loss is the signal-to-noise ratio (SNR), which compares an image section that is expected to be 100% signal (at the center of a homogenous object) with an image section expected to be 100% dark (from the empty space of the imaging volume), as shown in Fig. 4.10. The results of the total system demonstrate a very low amount of interference, as shown in Fig. 4.10, with a normalized SNR loss never exceeding 2.1%, as shown in Table 4.1.

Presently, in the many attempts to develop actuated MRI-guided interventional robotic systems, a primary concern has been image compatibility. The most common metric for determining the compatibility of a device is a measurement of the SNR, with the most widely accepted method of calculating SNR and SNR change being the standard put forth by the National Electrical Manufacturers Association (NEMA)[73]. Appendix C is a complete copy of the NEMA standard. Because there is no accepted standard for allowable SNR and SNR-change levels for MRI-guided interventions, and because this system is targeted to support the development of a wide variety of interventional procedures, all supported system modules are designed to contribute minimal levels of image interference when operated within the scanner during imaging, allowing the user a maximum amount of freedom in his own design work. In order to validate the compatibility, a cross-section of procedures which currently utilize MRI guidance and procedures that are currently being targeted for MRI guidance was established, as given in Table 2.5.1.3.

In order to demonstrate that the system modules can function within the scanner environment in the manner predicted, NEMA standard

TABLE 2.2: Experimental Results of MRI Compatibility Evaluation showing SNR and percentage change

Protocol	Baseline	Motor Off (%change)	Motor Running (%change)
T1W	148.7	150.5 (1.24%)	149.8 (0.76%)
T2W	620.4	631.8 (1.84%)	629.4 (1.46%)
FGRE	141.2	142.8 (1.19%)	141.6 (0.30%)
EPI	228.4	223.6 (2.09%)	226.3 (0.92%)

experiments for all of these protocols were performed [73]. The specific requirements for compliance with a NEMA-standard SNR analysis begin with the following experimental setup properties:

1. Region of interest is a centered, regularly shaped geometric area enclosing at least 75% of the image of the signal-producing volume of the phantom.
2. The phantom shall be centered in the RF receive coil.
3. The RF receive coil shall be electrically loaded such that the electrical parameters are the same as when a 50-90kg human is positioned for a scan.
4. The room and phantom temperatures shall be $22 + 4^{\circ}C$.
5. A spin echo pulse sequence (first echo) is recommended but not required.
6. $TR \geq 3xT1$ of the filler material in the signal-producing volume.
7. TE shall be within the clinically selectable range.
8. A single, transverse axial slice shall be acquired at isocenter.
9. The selected field of view shall not exceed 110% of the largest linear dimension of the RF coil in the image plane.

10. The slice thickness shall be $\leq 10mm$.

In addition to these scan conditions, four sets of image processing methods are approved and detailed by the NEMA standard. Our lab chose to use two of the four methods: image subtraction and single magnitude image analysis. While the image subtraction method classically is considered to be a more mathematically accurate reporting method, physical shift between consecutive scans can greatly skew and distort results of this type of analysis, which is why the single magnitude image analysis is also utilized [73].

2.5.1.1 Image Subtraction Analysis of Image Noise

The first step in this analysis is a pixel-by-pixel subtraction of the baseline image from the studied image, creating a third image. The standard deviation (SD) of the pixel values of this resulting image is used to determine the image noise from the following equation:

$$SD = \left(\frac{\sum_{i=1}^n \sum_{j=1}^m (V(i, j) - V)^2}{\sum_{i=1}^n ((m_i) - 1)} \right)^{\frac{1}{2}} \quad (2.18)$$

1. V is the average pixel value in the subtracted image
2. $V(i, j)$ is a specific pixel value
3. i index spans the read encode direction
4. j index spans the phase encode direction

To aid in ameliorating the effects of physical shift during imaging, an additional equation, which can reduce the effects of temporal

instability through the evaluation of successive differences between adjacent points in the image, is defined with the same terms:

$$SD = \left(\frac{\sum_{i=1}^n \sum_{j=1}^m (V(i, j+1) - V(i, j))^2}{2 \sum_{i=1}^n ((m_i) - 1)} \right)^{\frac{1}{2}} \quad (2.19)$$

Since both of these SD measurement operations involve a difference operation, the noise measurement must be corrected as follows:

$$\text{image noise} = \frac{SD}{\sqrt{2}} \quad (2.20)$$

2.5.1.2 Single Image Measure of Image Noise

When utilizing the single magnitude image method, the SNR of each individual image is determined, and then the SNR change between the baseline image and the study image is calculated. With this method, the average signal strength is measured within the signal producing area, then a space outside of the signal producing area of at least 1,000 pixels in size is analyzed to determine the SD of noise in the measurement regions of interest (MROI), as shown in Fig. 2.26. Since the image is a magnitude image, the noise distribution will not be Gaussian distributed but rectified to a Rayleigh distribution, therefore the SD is estimated from the mean of the Rayleigh distribution, such that the resulting SD figure must be adjusted with a correction factor given by the following equation:

$$imagenoise = \frac{SD}{0.66} \quad (2.21)$$

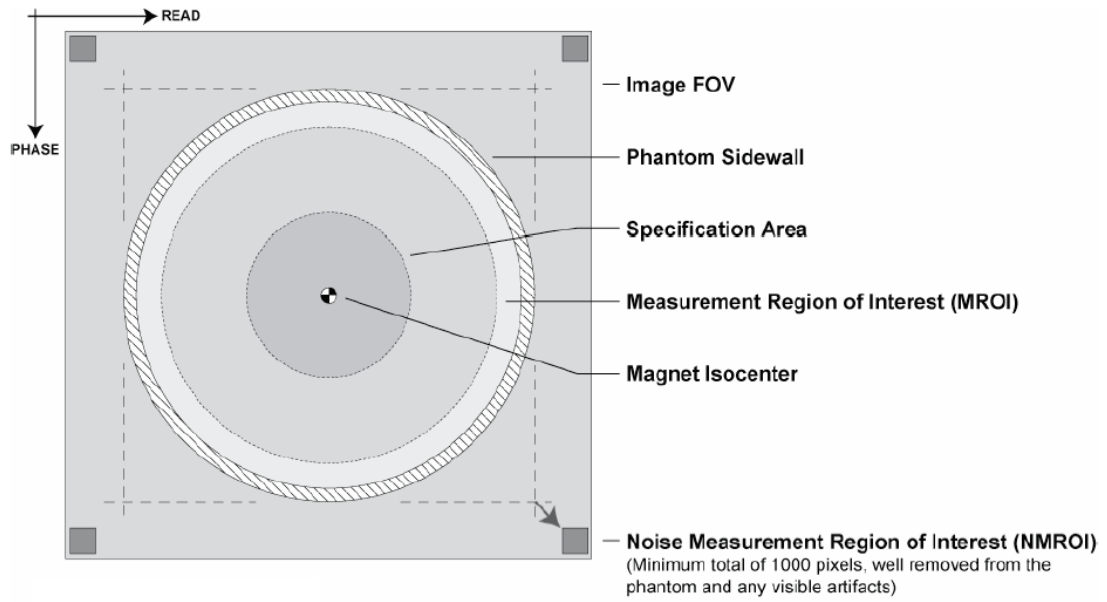


FIGURE 2.26: Imaging protocol guidelines for magnitude image-based SNR evaluation taken from [73]

2.5.1.3 SNR Calculations and Results

Whichever method is utilized to determine image noise, SNR is the following ratio:

$$SNR = \frac{S}{\text{image noise}} \quad (2.22)$$

Where S is the mean pixel value in the MROI minus the baseline pixel offset value, if any. Results of SNR analysis of the entire system were very promising, showing great improvements over all published, scanner-independent results which could be found by the authors, for either of the actuators studied. As shown in Table, the SNR loss of the subtraction analysis was never above 4%, and that of the magnitude image analysis was never above 2%.

To derive these figures of image interference results, first an image subtraction protocol was used. It is a graphical rather than numerical

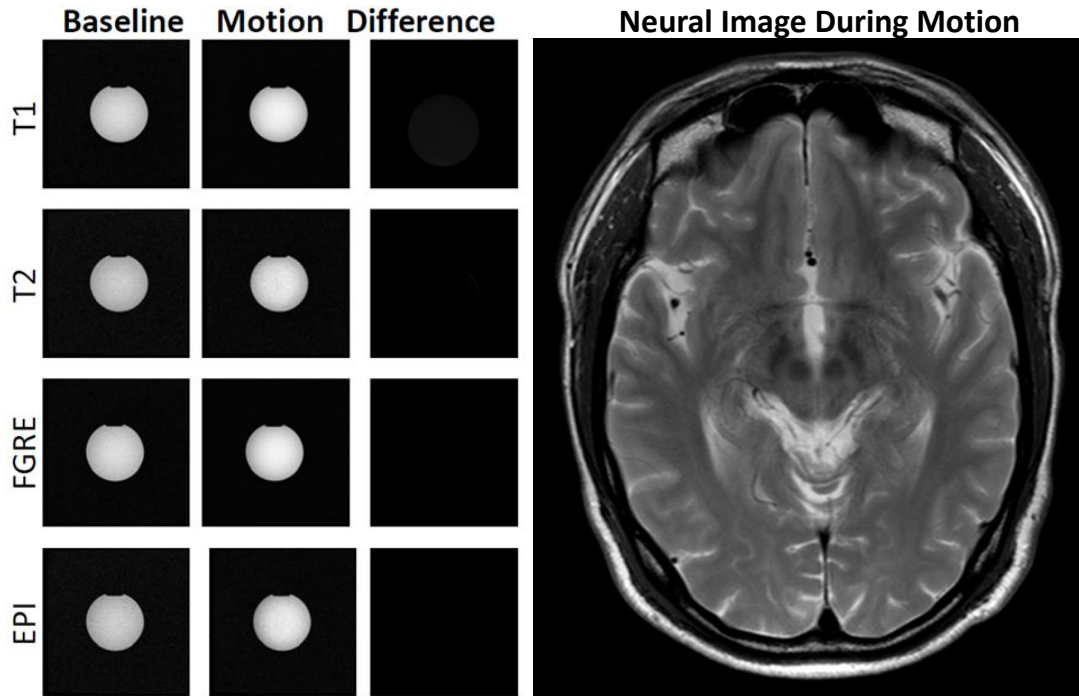


FIGURE 2.27: Left: Image subtraction analysis of interference caused by equipment under a variety of imaging protocols. Right: MR image of neural anatomy with system in place and operating.

method, the subtracted images are often visually compared to give context to the numbers and are shown as qualitative evidence of the compatibility of the system and actuators under the protocols targeted, as shown below in Fig. 2.27.

2.5.2 Joint-Level Accuracy

After functionality and image compatibility of the system had been established, the mechanical control performance of the system was analyzed. System-level accuracy is assessed for the neural intervention system in Chapter 4. This took the form of analyzing step and sign response of a single, encoded actuator free from any addition equipment. Validation of more complex and precise motions will be given in Chapter 4 when the neural intervention system is presented.

A single Piezo LEGS actuator was connected to a U.S. Digital optical encoding system with a maximum resolution of 1,250 counts per revolution, and operated under PID (proportional-integral-derivative controller) loop control. As given in Fig. 2.28, the step response plot shows no detectable overshoot, due in part the rapid loop time of the control system (less than 1 millisecond) and the high holding force and sub-millisecond clamping time of the actuator when de-energized.

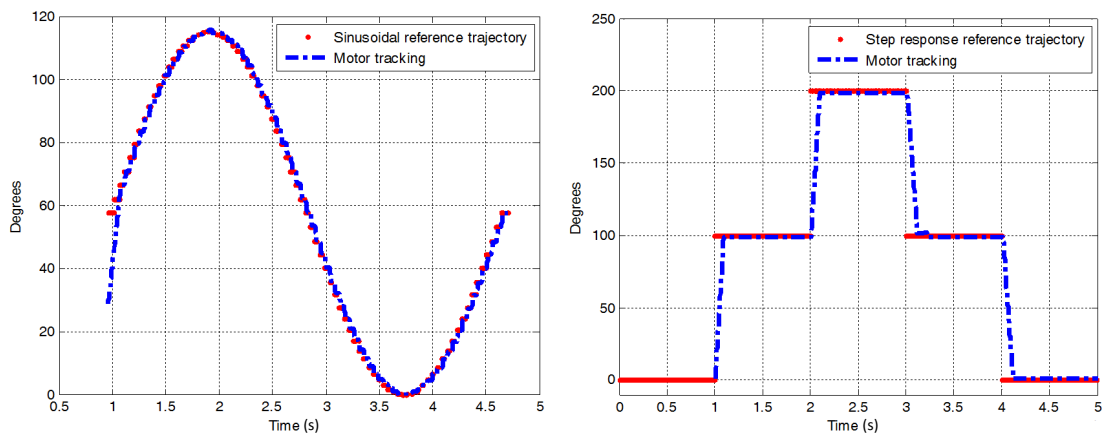


FIGURE 2.28: Plots of sinusoidal tracking and step response for individual joints. Note the lack of overshoot and the rapid stopping times.

2.6 Discussion

Development of robotic technology is often based upon leveraging the use of a development platform which integrates communication, actuation driving, and processing such that the developer can focus narrowly on the specific contribution being sought. Before the presented work, the lack of a development platform for the creation of MRI-compatible actuated devices presented a significant obstacle to the development process. The current expression of this system supports the development of MRI-guided interventional devices by

integrating a series of modular basic components which have been developed or selected to be MRI-compatible. The system not only represents an “end to end” robotic development platform featuring navigation, communication, actuation, and sensing, but the totality of the deployed system has been shown to operate with very low levels of image interference. This system allows users to focus on their primary areas of research, as it provides the totality of the infrastructure for an experimental environment. An example of such a design process detailing the development of a stereotactic neural intervention device is presented in Chapter 4, though several other applications developed using this system are presented below.

Demonstrated Applications

The work presented in Chapter 4 of this dissertation detailing the MRI-compatible stereotactic neural intervention device represents the first successful application of this system to an interventional procedure, although this is not the only device created to date which leveraged the advantages of this system to speed its creation. Other members of the AIM laboratory have developed devices utilizing this system, including an MRI-guided prostate intervention system presented by Su *et al.* which also utilizes the modular prismatic motion stage shared by the stereotactic neural intervention system [56, 74–76]. Collaboration between Su and Cardona *et al.* [29] further expanded the functionality of this prostatic intervention device to include operation of a concentric tube continuum robot. The paper detailing this research was a finalist in the 2012 International Conference on Robotics and Automation. Furthermore, the process leading from project origination to functional prototype of this design not

only followed the proposed rapid device development procedure, but also required a total development time of less than 8 weeks. In addition to this, a haptic master device was constructed and deployed for insertion of the prostate brachytherapy device for use within a scanner. This device was created by trimming the model of the prostate robot in SolidWorks, printing with a 3D printer, and assembling with only the linear slide and encoder system present, all in under 3 days. Nevertheless, the modular architecture supported integration with the prostate system nearly immediately upon construction. Additionally, a novel needle driver module is currently under development. A single student is responsible for all of the development work. While kinematic and structural analysis of the device is ongoing, the student has the ability to devote all of his attention to the kinematic specification and modeling of this device, as the software and hardware platform presented here accommodate all other infrastructure associated with testing and deploying it. Currently, the system is being used by several other institutions and laboratories including labs at Harvard University, Johns Hopkins University and the Warrior Research Center at Auburn University.

Chapter 3

Characterization of Piezoelectric Actuation to Enable Advanced Control

3.1 Overview

The method with which an electromagnetic motor converts electrical energy to mechanical energy is very straightforward and well understood. The electrical potential is directly proportional to the force being generated, which leads to straightforward operation of these motors under a variety of control schemes including force control. The method with which a PZA converts electrical energy input into a mechanical output is highly complex in comparison. It is a combination of a repetitious electromechanical action, which is then converted mechanically into a continuous motion often through a frictional transfer. Independently each step of this process is fairly well understood and modeled. Predictive modeling of a complete actuators behavior is quite difficult due to the scale of the individual piezoelectric motions combined with the crystals' susceptibility to

minute changes in operating conditions. This complex behavior does not present a problem when operated under closed loop conditions, as a simple PID controller can easily adjust for changes in the motors operating properties. Operating these motors under open loop control is another matter. In order to effectively predict a PZA's open loop response to electrical stimuli, many aspects of the internal structure of the actuator must be considered, including but not limited to, contact dynamics of the frictional interface, actuator materials properties and temperature [77, 78]. Further frustrating this effort are the high degree of manufacturing variability of the actuators, rapid wear characteristics, and inherent hysteretic and non-linear behavior [79]. While models with varying degrees of effectiveness have been presented, the variability in actuator behavior, even amongst the same actuator over time, makes using a single model to predict actuator behavior difficult. Because this modular system was developed to support a wide variety of PZAs, implementing a single explicit model of piezoelectric actuation is unlikely to be successful while developing or using a different explicit model for each supported actuator is impractical. For these reasons, modern methods for characterizing motor behavior have been reviewed, and common properties of each method were used to propose a parameter-based method and apparatus for developing low-computational-cost, actuator specific force control models. The parameters of this model are targeted to be fit to a specific actuator over a desired application range using a force analysis module to calibrate each actuator for its desired task.

3.2 Contributions

The contributions of this section include the development and validation of an analytical device and method which can be used to characterize the behavior of linear piezoelectric actuators such that a force control algorithm with low computational costs can be enacted. The contributions of this chapter are summarized as follows:

1. Review of current modeling methods of quasistatic piezoelectric actuation.
2. Proposed parameterized model for operation of PiezoLEGS motor under force control and method for fitting to same to a targeted linear region of operation.
3. Development of equipment and experimental setup to gather required data.
4. Validation of equipment.
5. Development of proposed method to implement equipment and parameter fitting algorithms.

This chapter will review current modeling techniques used for the characterization of the Piezo LEGS PZA, followed by the process to develop the simplified characterization model for these actuators, and finally the justification for this simplification. Additionally, the design and development of the experimental apparatus used to study motor operating characteristics is presented and its effectiveness discussed.

As can be seen in the review published by Spanner *et al.*[80], there exist a wide variety of operating principles for PZAs, which can effectively be separated into two main subcategories: quasi-static and ultrasonic. Even within these two main categories, there are various subtypes of actuating methods; however, this chapter of the dissertation focuses on modeling and control methods for the Piezo LEGS quasi-static actuator. This actuator was chosen due to its widespread use in interventional applications, as was demonstrated in Chapter 1.

3.3 Principals of Operation

The first step toward creating apparatus and methods to characterize an actuator is to understand the operating principle of the actuator in question. The Piezo LEGS piezoelectric actuator is a quasi-static walking leg actuator comprising four bimorph legs arranged in two electrically coupled pairs, as shown in a diagram prepared by Szufnarowski *et al.* in Fig. 3.1.

As can be seen, the motor comprises a series of four piezoelectric bimorph stacks arranged in 2 electrically coupled pairs. When the 4-phase analog driving circuitry energizes these pairs, the tips of the respective stacks move in a phased, periodic path such that only one of the pairs of stacks is in contact with the drive strip at any given time. The shape of this tip deflection varies according to the shape of the driving waveform applied, the specifics of which are presented in Appendix A. This operating principle aids in overcoming some of the strong hysteretic behaviors of piezoelectric stack actuators, since the tip deflection of a stack actuator such as this has

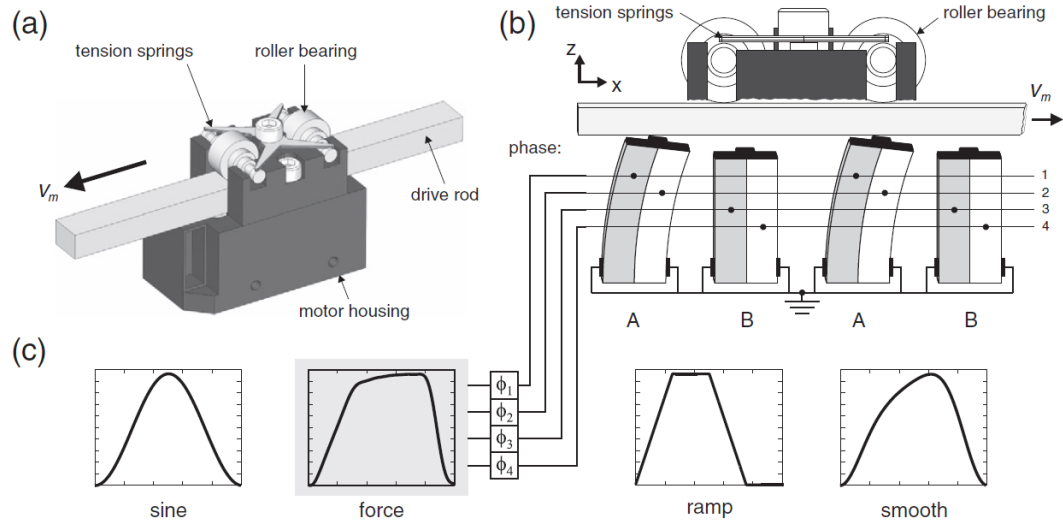


FIGURE 3.1: (a): Solid model of Piezo LEGS actuator with main components identified (bimorph stacks located inside motor housing) (b): Depiction of contact interaction between bimorph legs, drive strip, and preload structure, as well as electrical correlation between driving waveform and bimorph stacks (c): Examples of different wave shapes utilized to drive actuator. Figure taken from Szufnarowski *et. al* [81]

been shown roughly to conform to steady-state operation once the first cycle of driving stimulus is applied [79]. Assuming the motor driving waveform is a constant shape, this operating principle gives rise to four clear available control variables: frequency, phase angle, amplitude, and offset. While it has been shown that the relationship between excitation frequency and motor velocity is fairly linear in an unloaded state, once the motor is loaded this relationship becomes non-linear [82, 83]. Because of this non-linearity, predicting the behaviors of these actuators under dynamic conditions becomes unreliable with simplistic control methods, which is the motivating force driving precision modeling of these actuators [84].

3.4 Modeling Approaches

There has been a great deal of development in the area of characterizing the behaviors of the Piezo LEGS actuators; however, the two most complete modeling methods implemented thus far are those presented by Merry *et al.* [84] and Szufnarowski *et al.* [81, 82]. The work of Merry *et al.* is motivated by improved micro-positioning of atomic force microscopy stages and thus considers these actuators by modeling an individual layer of the 96-layer bimorph stack and then assembling these layers into an increasingly complete model. This model has been used to operate these actuators in position, velocity and force control for small scale motions. While the results of Merry's model demonstrate highly effective fitting, as can be seen in results published in [84], this control method is not practical for applying force control to large-scale motions of the actuators.

Szufnarowski *et al.* have presented both a model focused on the total performance of the actuator considering the entire bimorph stack as a bending beam, and a lumped parameter model where most of the properties of the model are identified from material properties. While this model has been demonstrated to simulate and control a Piezo LEGS actuator with a high degree of precision, as shown in Fig. 3.2, the control method presented has a very high computational cost involved, and cannot operate without the use of a force sensor for feedback.

While these methods have demonstrated a high degree of precision, they are impractical for our purposes due to the high computational cost of operating the control loops. Tse *et al.* presented a method for force control of the Piezo LEGS actuator utilizing a 30-neuron, 2-layer neural network to empirically model the complex system with

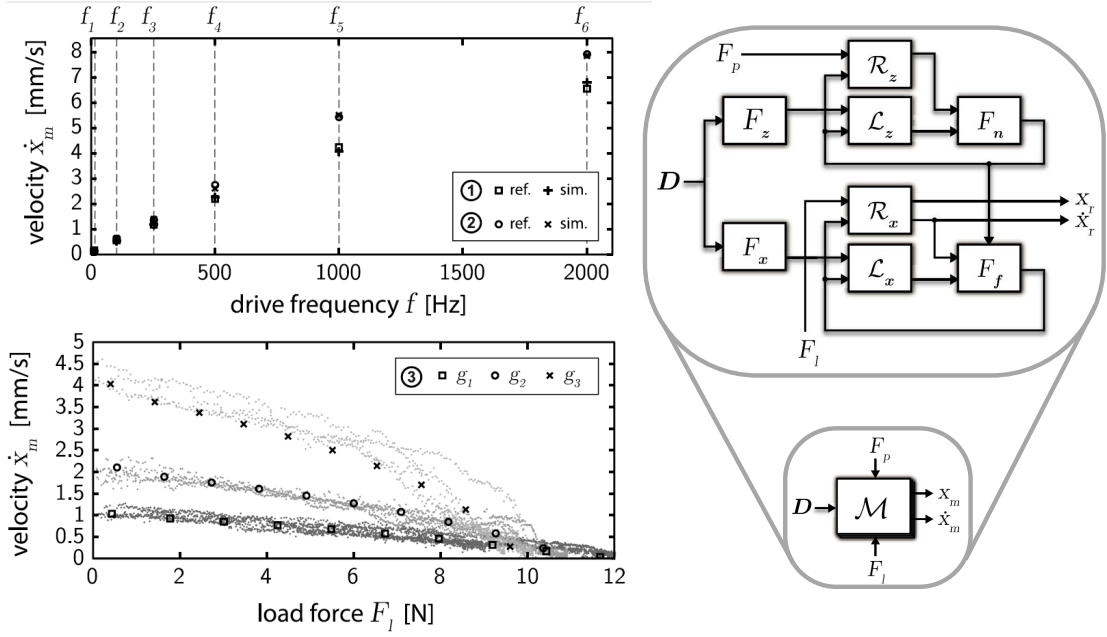


FIGURE 3.2: Left top: Plot of drive frequency vs. velocity, both measured and simulated. Left bottom: Plot of load force and velocity, both measured and simulated. Point cloud represents measured results, while the three series of markers labeled g_1 , g_2 , and g_3 represent model predictions based on 3 driving frequencies. Right top: Detail structure of control model of piezoelectric actuator. Right bottom: Simplified black-box representation of control model depicting inputs and outputs. These diagrams taken from the work of Szufnarowski *et. al* [82]

which the motor was constructed. However, their work as presented is based on admittance control, where force sensing on both master and slave unit are required[85]. Arafa *et al.* presented a dynamic model for a piezoelectric actuator, in which they demonstrate the accuracy of a linear model for the force and velocity response of an actuator. This model uses two separate algorithms, one for when the PZA is loaded in the direction of motion, and one when it is loaded in the opposite direction, the results of which are shown in 3.3. This method was informed by general operating information provided by the manufacturer [86].

Relative benefits, drawbacks, and characteristics of these models both informed and motivated the development of equipment and

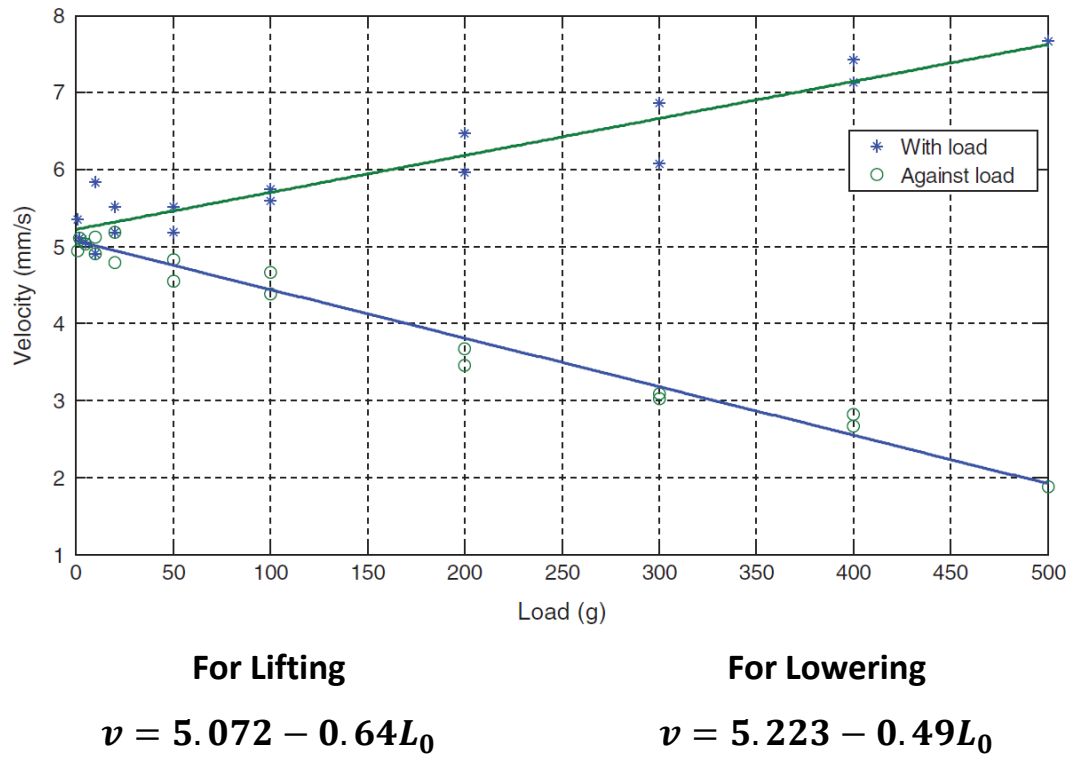


FIGURE 3.3: Top: Plot of load and velocity in lifting and lowering applications with varying load and fixed drive frequency. Bottom: Linear approximation of effects load has on velocity as presented by Arafa *et al.* [86]

methods for advanced control of PZAs. The proposed method couples a simplified, parameter-based motor control algorithm, which is designed to be locally accurate to a specific targeted region of motor operation. Coupled with this proposed control method is the development of analytical equipment and methods which could then be used to study the operation of a specific piece of equipment and fit the parameters of the simplified force control model. As has been demonstrated, while the Piezo LEGS actuator can only be completely characterized through complex models accounting for non-linearities, hysteretic behavior, and material properties, all of the models demonstrated large, approximately linear regions. The experimental results presented by Arafa *et al.* demonstrated the potential for a lower-order control method fit to a specific motor

through empirical observation.

3.5 Proposed Direct Force Control Method

In the presented work, the purpose of operating a motor under direct force control is to support haptic feedback, where robustness and computational efficiency is preferable to sub-millinewton accuracy. Though the required complexity for explicitly enacting precision control of Piezo LEGS actuators over their entire range of operation would be too processor-intensive to operate on the embedded computational unit present in our control system, selection of an approximately linear region of motor operation can be effectively characterized with a simplified model. This strategy is based on results presented in the previous section, coupled with manufacturer-supplied specifications detailing a coupling of step size, load force, and drive frequency, as shown in Fig. 3.4.

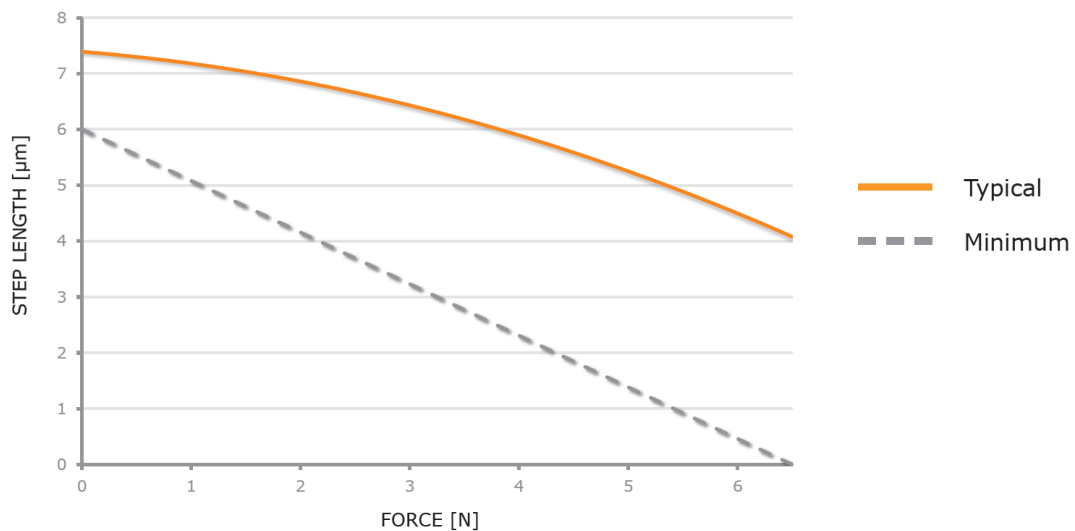


FIGURE 3.4: Specification of step size vs. load under constant frequency operation, provided by manufacturer of Piezo LEGS actuator [87]. Note the curve depicting typical operation and the dotted line depicting manufacturer-guaranteed minimum performance.

The plot in Fig. 3.4 indicates that the relationship between step size, load, and motor velocity can be accurately approximated as linear for a narrow region of operation. If the force control can be operated with a degree of precision sufficient to provide haptic transparency to the operator, its purpose will be fulfilled. An analysis of the accuracy of this control method will be presented, although a determination of the effectiveness of this transparency for use in haptic feedback is beyond the scope of this work.

Development of this force control method progressed as follows:

1. Construction of precision force testing equipment capable of integration with control system
2. Collection of force, velocity, and drive frequency data
3. Analysis of collected data and identification of linear regions
4. Determination of final form of force control method, balancing precision with computational costs
5. Validation of force control method under varying speeds, loads, and excitation frequencies

3.6 Development of Force Testing Equipment

The modular nature of the device development platform for which this module was being developed led to the design of a motor analysis instrument which could be used to study a variety of linear actuators under varying loads, despite the goals of the presented work being

limited to characterization of a Piezo LEGS linear actuator. Additionally, it was desired that the instrument support direct visual observation of the contact interaction of the actuator through microscopy coupled with stroboscopic video capture. These needs led to the following functional specifications of force testing instrumentation:

1. Must be constructed of sufficiently rigid materials such that deflection of structure will not interfere with accuracy of measurements.
2. Must have an interchangeable actuator mount such that new actuators can be attached.
3. Force sensing device must be coupled directly to actuator so that actual loads on the actuator are observed.
4. Must have standard 1"-spacing mounting holes such that it can be mounted to an optical table for observation with microscopy.
5. Must restrain motion of motor to the linear direction such that side loads, torsion, and crabbing do not influence gathered results.
6. Linear translation must contribute 2 orders of magnitude less resistance than the maximum driving force of the motor.

The force testing rig designed to these requirements utilized a Futek LSB200 load cell (Futek Corporation, Columbus, Ohio), an ultra-low friction, precision linear slide (coefficient of friction 0.003), and an Airpot 2KS160 precision dashpot (Airpot Corporation, Norwalk, CT), as shown in Fig. 3.5. A dashpot was selected as the primary loading mechanism since the velocity-dependent force applied by the

device would yield a wider range of force-velocity measurements for a given fixed-frequency test procedure, expanding the value of each individual test run. The primary construction material was 6061–T6 aluminum, and the fabrication method was hydrocutting with hand finishing.

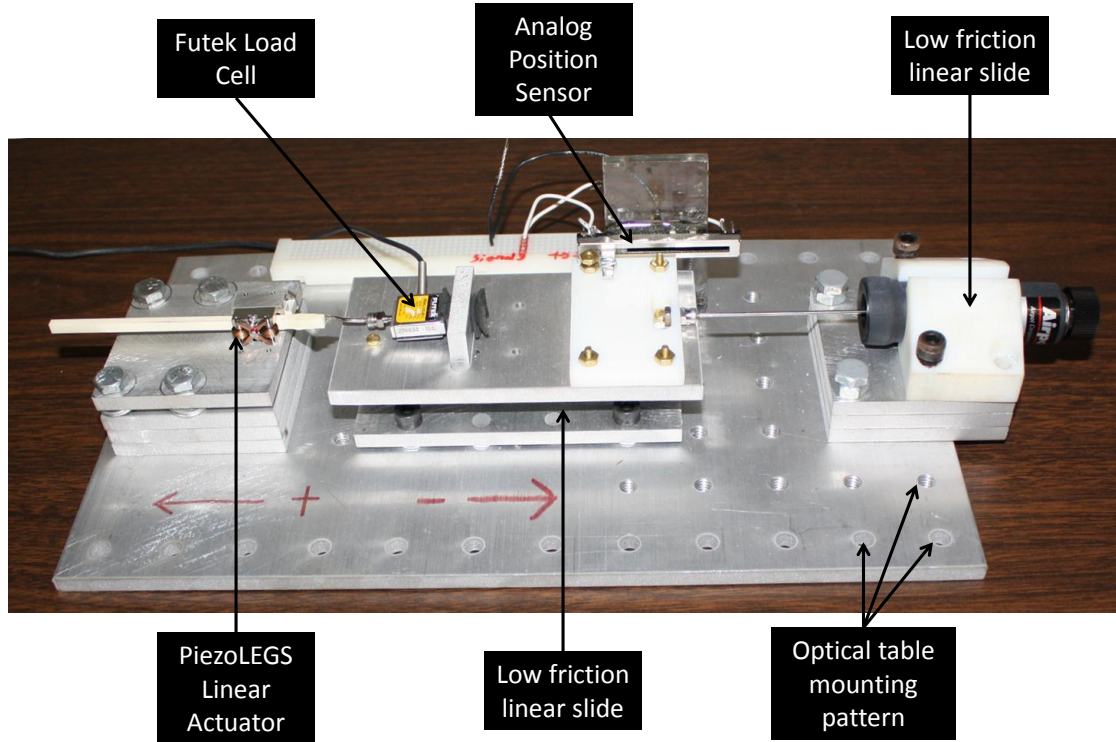


FIGURE 3.5: Force analysis device. Note the placement of force sensor directly in line with Piezo LEGS linear motor and central axis of dashpot load. Also note the placement of potentiometer for position encoding and mounting platter for connecting to optical tables or attaching other devices.

3.7 High Speed Microscopy

A consistent problem with validating PZA models is motion of the crystals cannot be directly observed while the actuator is assembled, due to a lack of line of sight to the drive-peg to drive-strip interaction point, as can be seen in Fig. 3.6 [82]. Additionally, total tip

deflections of the crystal peg is on the order of 6 – 14 micrometers and occurs at frequencies ranging from 50 Hz to 12 kHz, though the manufacturer suggested operating frequency range is between 750 Hz and 3 kHz. Despite high speed cameras capable of operating with a shutter speed well above the Nyquist frequency of this range, assuming the motion of the peg will not contain higher frequency components is invalid. The work presented in this section demonstrates two approaches taken to directly, visually observe oscillations of the driving crystal. Two methods of accomplishing direct observation of crystal motion were attempted in order to both validate existing models, and create a platform for further development and refinement of driving methods for advanced control of PZAs: use of a high speed video camera capable of recording images live, and a stroboscopic method to sequentially image specific sections of the driving waveform with a low speed camera, and assemble them in chronological order. In order to create a line of sight pathway such that the crystals could be directly observed, a viewing portal was cut in the motor housing such that the motor could remain as close to its natural operating state during observation. In order to prevent unnecessarily damaging a motor, direct imaging methods effectiveness was verified using a motor without the preload installed first to confirm that the motion of the crystal leg was observable, after which the motor was modified.

3.7.1 High Speed Camera Observation

The first method attempted used a high speed camera with a microscopy lens attached to capture images of crystal motion in real time. When selecting a high speed camera system, the speed and

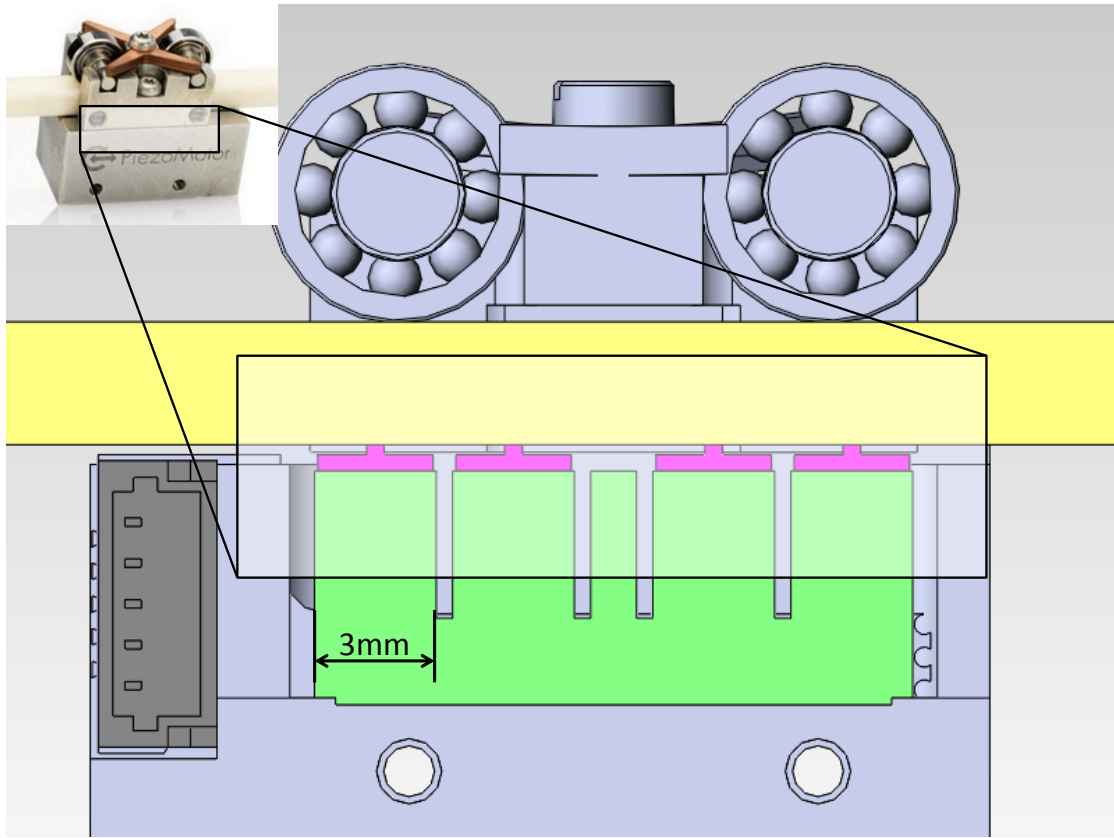


FIGURE 3.6: Diagram of the interaction between the driving legs and driving strip of a PiezoLEGS PZA. Note the yellow drive strip, purple ceramic drive caps, green piezoelectric stacks, and scale. Inset: photograph of PiezoLEGS PZA indicating location of cross section.

resolution at which the camera can capture images are of primary concern, though additional aspects of camera operation such as pixel and sensor size, light sensitivity, and available interfaces must also be considered. Though camera systems capable of imaging with shutter speeds as low as a trillionth of a second have been constructed, for practical purposes in a laboratory setting the available capabilities of high speed cameras are much more limited [88]. The first set of experiments designed for this study was to assess the feasibility of using a high speed camera system for the real-time observation of ceramic driving elements within the PiezoLEGS actuator. For this experiment, an unloaded PZA driven by the modular robot controller was recorded by a high speed camera system. The system chosen for

this analysis was based on a Y7-S3 (IDT Technologies, Tallahassee, FL) camera, capable of capturing images at rate of 9,000 frames per second with a resolution of 1,280 x 720 pixels, a K2/SC long distance microscope lens (Infinity Photo-Optical Company, Boulder, Colorado) and high intensity LED flash which was triggered by the camera shutter, as can be seen in Fig. 3.7.

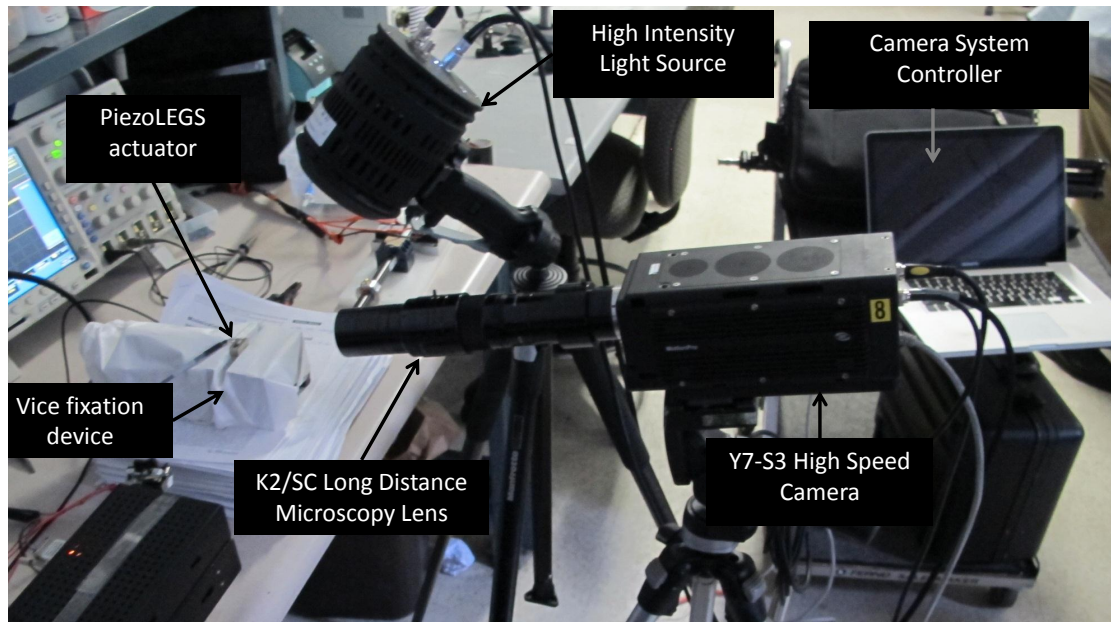


FIGURE 3.7: Experimental setup to analyze possibility of using a commercial high speed camera system to observe PZA crystal peg motion in real time. Note the PiezoLEGS actuator disassembled so the driving pegs are exposed, as well as the high intensity light source, high speed camera, long distance microscopy lens, and camera control system. Not shown is the modular control system presented in Chapter 2 used to operate the motor.

Video collected from this series of experiments demonstrated that the motion of the ceramic leg was visually observable. As can be seen in Fig. 3.7, the actuator being observed was mounted in a fixed stand, while the camera and lighting system was mounted on aluminum tripods, a setup not considered rigid enough for use in the final expression of this experiment. In order to ensure that the vibration being observed was in fact the motion of the crystal leg, and not vibration being caused by external sources, the crystal was

driven at several frequencies that were compared to the frequency of motion being observed in the video collected, in addition to collecting a video of the actuator not being driven. A sample image from this study can be seen in Fig. 3.8.

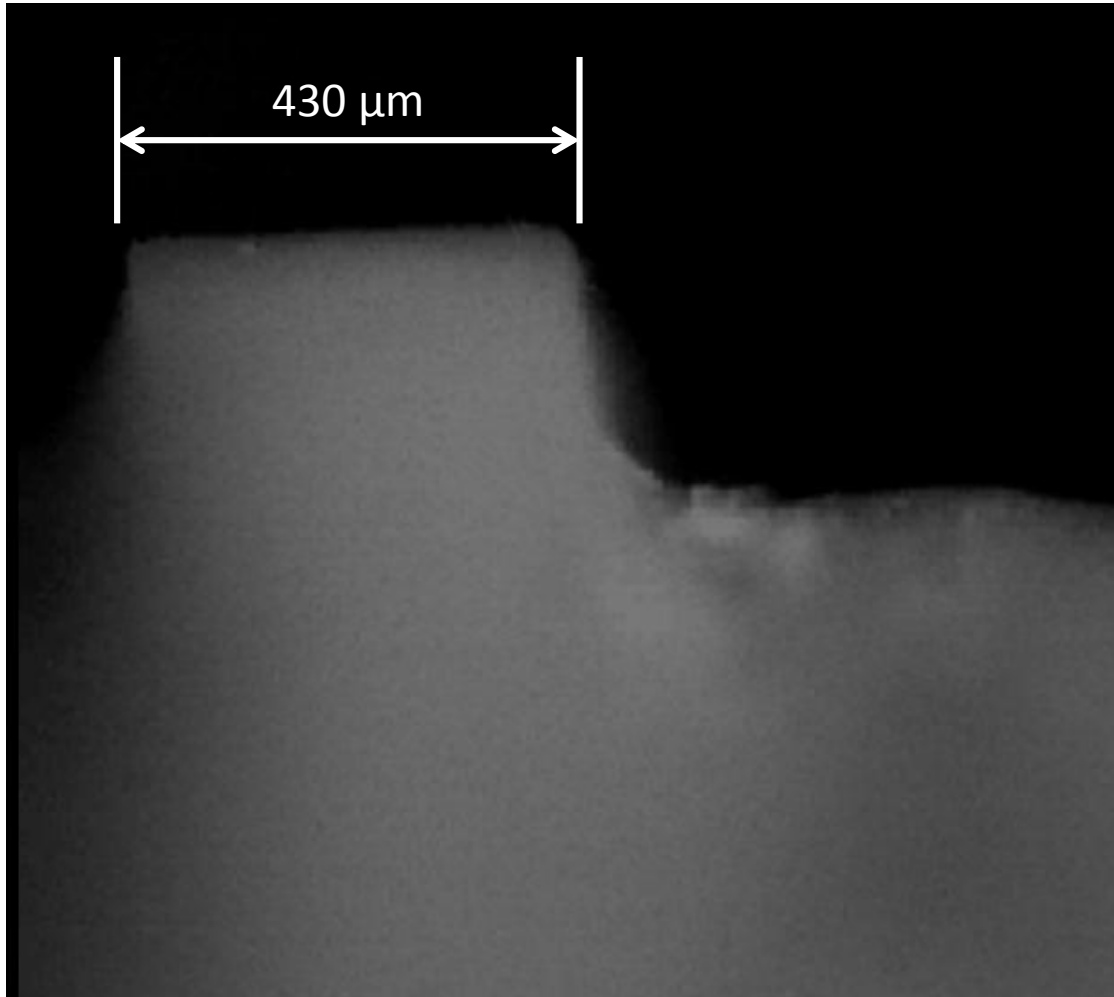


FIGURE 3.8: Sample image gathered during the high speed camera test. Note the field of view is approximately 1.25 mm square, giving an approximate pixel width of 4 micrometers, which is far too large to characterize a 12 micrometer motion. The rectangular driving peg shown is part of the ceramic cap on a driving leg, colored purple in Fig. 3.6

Though this experiment demonstrated that the motion was visually observable, the total deflection of the motion was less than 3 pixels in the image space, indicating a great deal more magnification was required for the images to be usable for motion analysis. Though options to increase magnification were available, implementing them

would require a more effective lighting method, in conjunction with a support system to isolate experimental equipment from vibration. At this point, required mechanical and optical improvements dictated moving the experimental setup from a benchtop environment to an isolated optical table.

3.7.2 Stroboscopic Microscopy

In contrast to the real time, high speed imaging used in the previous experiment, this setup used stroboscopic video capture where the camera continuously records and the light source was triggered by the motor driving equipment rather than the camera equipment. By exposing the same portion of the driving waveform through repeated cycles, a lower speed camera can effectively image a high speed periodic motion. This practice of course relies on the assumption that the motion is truly periodic and repeatable, as individual images will be recorded from successive waveforms.

In order to generate the stroboscopic pulses at the precise point in the wave form desired, the FPGA on the PZA driver module was configured to output the trigger on one of the general purpose input output (GPIO) pins. The trigger pulse was fed out of the controller, into the driving electronics for the stroboscopic light. The terms defining the timing of the illumination triggering mechanism can be seen in Fig. 3.9. Note that ideally the trigger pulse width T_w would be minimized to reduce motion “smearing”, however a minimum duty cycle must be maintained to ensure sufficient illumination.

The second experimental setup, constructed in an attempt to directly observe the interaction between the driving leg of a PiezoLEGS PZA and the driving strip, was constructed on an optical table using

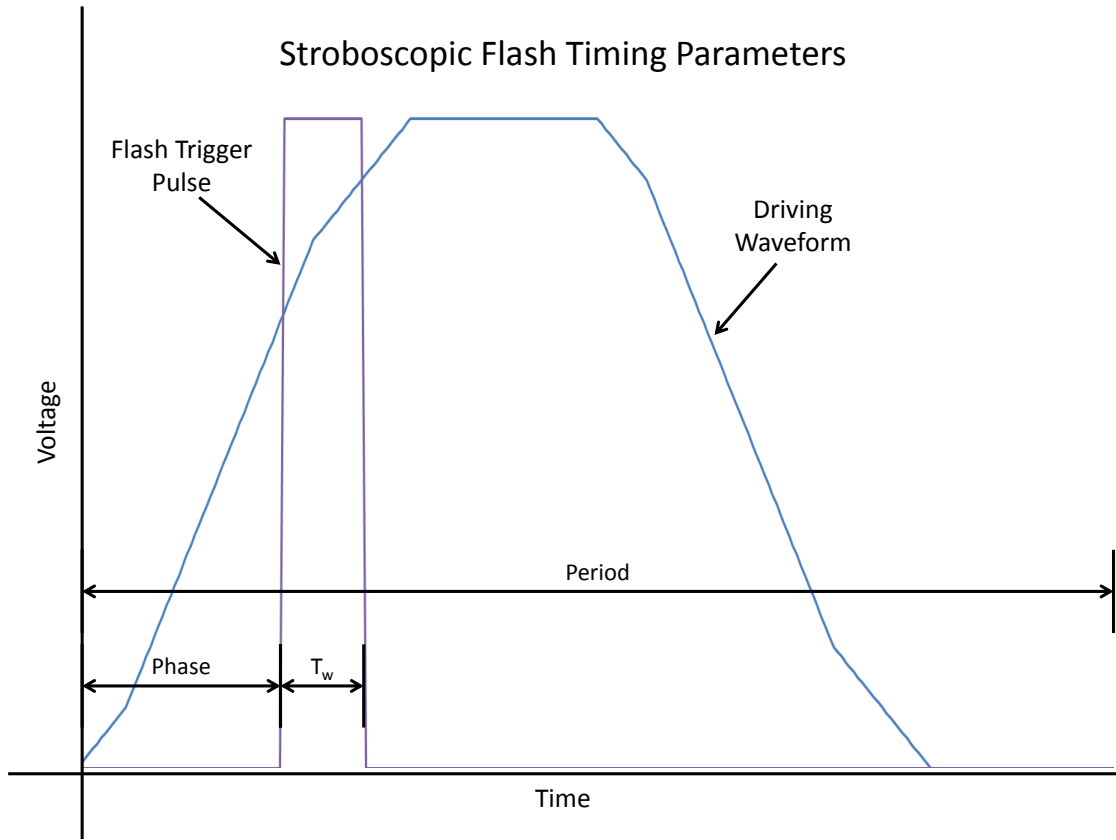


FIGURE 3.9: Stroboscopic illumination timing diagram. T_w is the flash pulse width, phase is the angular offset denoting the position of the illumination pulse in the periodic wave, and period indicating the total time of the wave period being observed.

a Nikon Eclipse microscope (Nikon Instruments Inc, Melville, New York) with a 100x objective lens, and a DC4100 stroboscopic illumination system (Thor Labs, Newton, NJ) and an Allied Manta 15 frame-per-second, 1 megapixel camera ($1,292 \times 734$ resolution) (Allied Vision Technologies, Stadtroda Germany), as can be seen in Fig. 3.10. This yielded an effective sampling rate of a minimum of 16 frames per cycle at 3 kHz driving frequency and a maximum of 64 frames per cycle at a 750 Hz driving frequency, without overlapping exposure of any portion of a driving wave cycle.

Stroboscopic studies of the free crystal oscillating yielded promising results, so a small window was cut out of the side of the motor to provide line of sight to the interaction point between the driving leg

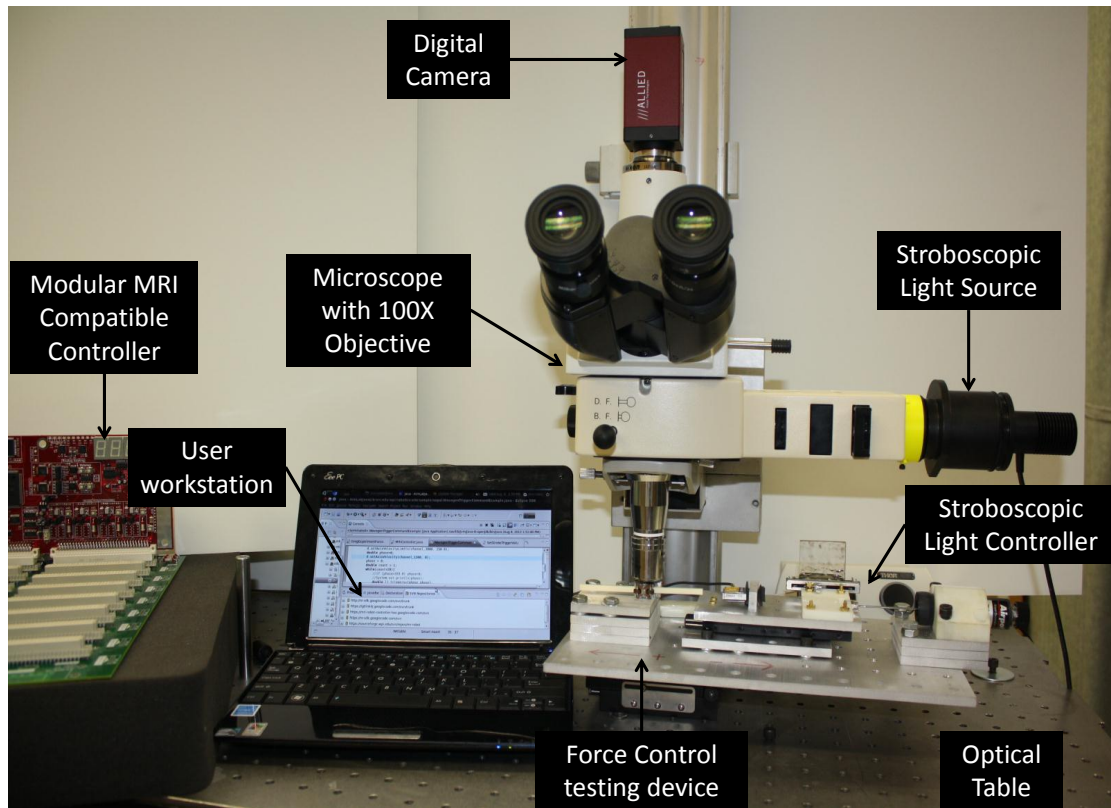


FIGURE 3.10: Experimental setup for stroboscopic microscopy study of piezoelectric leg motion in a PiezoLEGS actuator. Note the stroboscopic light source and controller triggered by the PZA driver, secure mounting of the force control testing equipment presented previously, and high magnification microscope and objective.

and the driven crystal. Though a significant portion of the illumination was blocked once the motor was reassembled, this experiment yielded usable data.

A method and apparatus for directly imaging the motion of a piezoelectric leg in a quasistatic PZA has been demonstrated, as part of the development of a platform which can be used to further refine and investigate methods for operating PZAs. The resolution of imaging acquired indicates currently that the motion can be imaged with up to 300 pixels in the X direction (parallel to drive strip motion) and 175 pixels in the Y direction (normal to drivestrip motion), corresponding to approximately 19 pixels per micrometer.

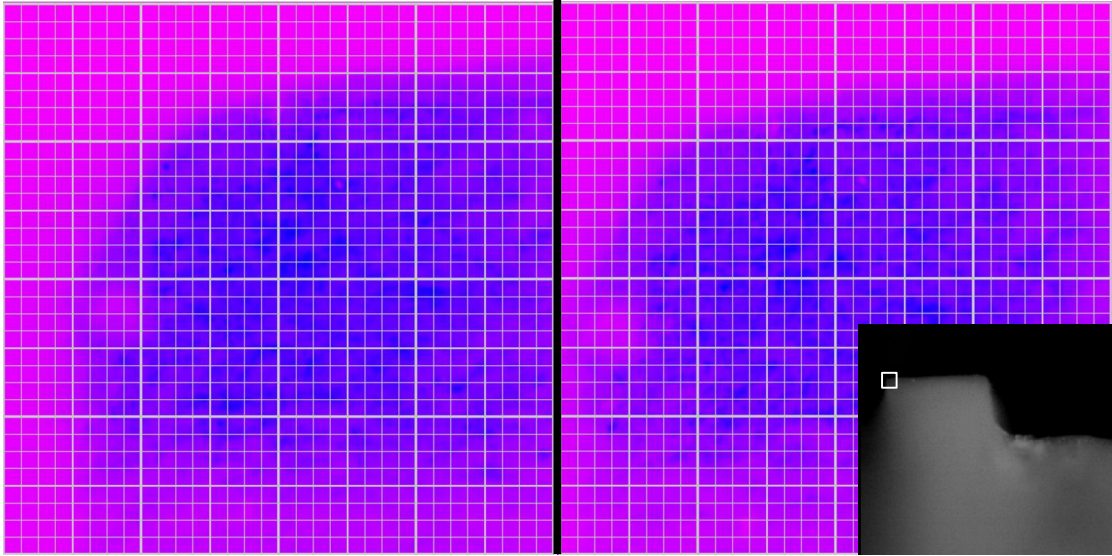


FIGURE 3.11: Sample image acquired by the stroboscopic motion analysis setup during motion. Note the grid size is roughly 3 micrometers per square indicating the reduced field of view, and greatly increased resolution. Note the high speed camera image on the inset, with the field of view for the stroboscopic setup outlined with a white box. Total field of view for the stroboscopic imaging setup is 96 X 96 micrometers.

3.8 Experimental Protocol and Data Analysis

In order to effectively utilize the Piezo LEGS linear actuator selected, its performance within manufacturer specifications needed to be characterized with enough resolution to make interpolation between data points possible while still maintaining an acceptable level of precision. This was accomplished by first selecting a range of operating frequencies and load settings to create an initial data set. Upon analysis and validation, we performed further testing runs to supplement the data. The experimental setup utilized the force analysis device detailed in the previous section, the MRI robot controller described in Chapter 2, and a Tektronix *MSO4034B* oscilloscope. The oscilloscope was utilized to collect data at a sampling rate of 1,000,000 samples per second per channel, yielding a minimum of

333 data points per wave period at the maximum operating frequency to ensure an appropriate amount of resolution was acquired. The initial test distribution ran 165 studies representing a fixed frequency test at intervals of $50Hz$ over the range of $750 - 3,000Hz$ at 3 different loading levels. In addition, a “holdback” set of data which could be utilized for validation of the model was also collected. Representative plots of data for analysis are given in Fig. 3.12.

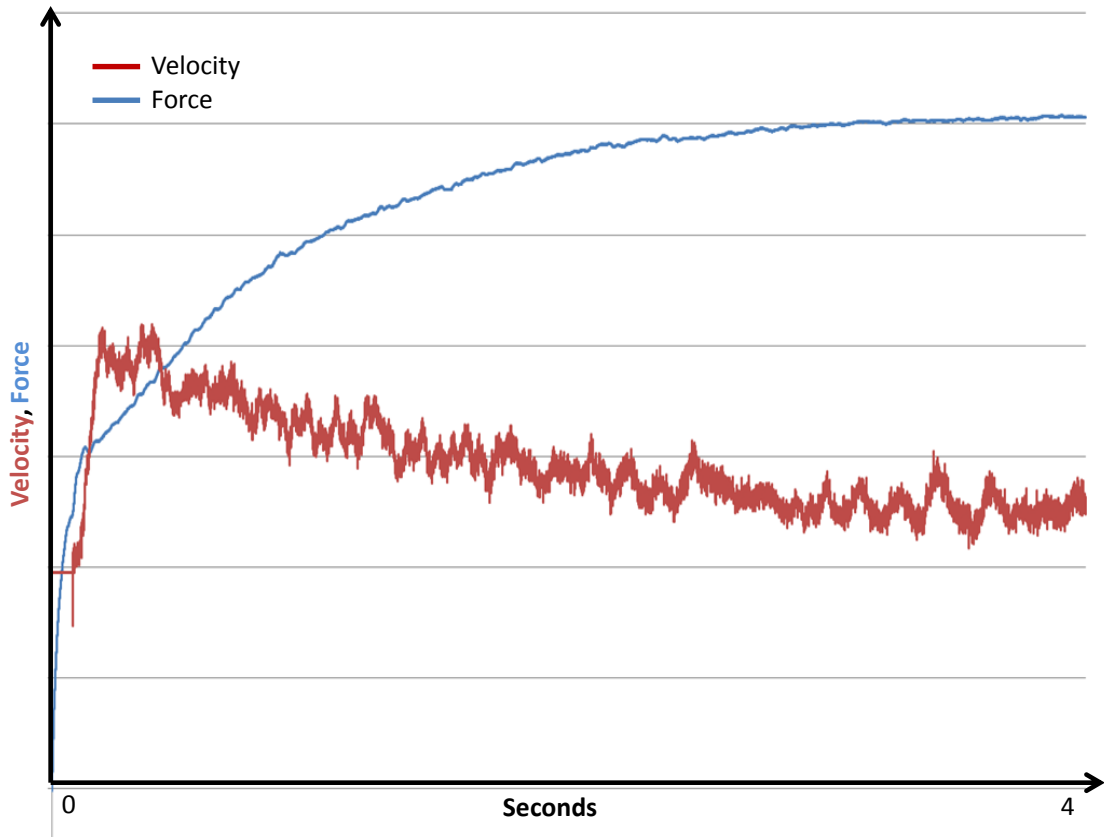


FIGURE 3.12: Representative plot of velocity load and time, with a fixed actuation frequency. Note the apparent inverse relationship between load and velocity at a fixed frequency.

As can be seen in the representative plot, the shape of the input stimuli is clearly visible in the output force recording, in addition to a clear inversely proportional relationship to velocity and force. While a very large dataset, over 52 billion data points, has been collected as a catalog of stimuli response recordings, analysis of this dataset

and derivations of control algorithms from it will be undertaken as future work.

3.9 Discussion

Though there has been a great deal of success developing an advanced characterization of piezoelectric actuator behavior, the majority of this work involves highly complex models not suited to be run on an embedded microprocessor. Additionally, while many models can simulate behavior of a piezoelectric actuator with a great deal of precision, current published work has not demonstrated an effective method to operate a PiezoLEGS actuator in a force control mode of operation without the use of a force sensor for feedback. The presented work sets the stage for development of algorithms to characterize PZA behavior over a narrow range of operation. Any algorithm developed using this equipment would most likely not be extensible to a wide variety of motor operation and installation without recalibration. Creating a method which can calibrate specific motors under specific operating conditions represents a practical advancement in the ability to apply these motors in real world situations. While algorithmic accuracy rapidly decreases as the velocity of the motor approaches zero, it is proposed that future refinement of calibration methods could overcome this difficulty. In addition, while the proposed control method only modulates overall driving frequency, preliminary experimental results demonstrate that modifying phase angle between driving phases has the potential to be leveraged to control force at low speeds. Development of this work is beyond the scope of this project.

Future Work

The goal of the work presented in this chapter is to extend the capabilities of the modular control system, and to evaluate the feasibility of using the control system to execute actuator analysis experimentation instead of just PZA operation. It has been shown that the equipment and methods created are capable of offering greater insight into the operating properties of PZAs. Now that the feasibility of applying this system to further research such as this has been established, logical progression of work with this platform is to develop advanced control methods through motor characterization. While this equipment was created to enable the use of the integrated control system to investigate motor characterization, there exist many other possibilities. Automated data analysis coupled with modified testing equipment could allow future users to calibrate fully assembled mechatronic devices, fitting the model not just to the motor, but the entire motion generation system. Exciting additional approaches could be applying genetic algorithms and automated data collection to optimizing wave forms and closed form models. Though these works present the most logical next steps with this equipment, there are clearly many more areas of development this equipment and methodology could be applied to.

Chapter 4

MRI-Guided Stereotactic Neural Intervention System

4.1 Overview

Leveraging the features of the modular development platform, a clinical system targeted a specific class of neural intervention procedure. As was discussed in Chapter 1, stereotactic surgery was developed to enable neurosurgeons to target and treat diseases effecting deep structures of the brain. While neural stereotaxy has been successfully applied for a period of time spanning decades, it remains highly invasive, time consuming, and plagued with difficulties associated with targeting and confirmation. Special attention was given to the aspects of ergonomics, clinical workflow, and substantial equivalence to streamline acceptance of this device by practicing clinicians and clearance by the Food and Drug Administration.

Development of this system was guided by a working relationship with our primary clinical partner, Dr. Julie Pilitsis, who provided an analysis of her own clinical experiences which shaped the functional

specifications and requirements of the final system. In order to better understand the effect of secondary image fusion on procedure time and accuracy, 10 consecutive DBS procedures (3 bilateral, 7 unilateral) performed via the traditional approach with a frame were considered. All patients underwent pre-operative MRI, planning, frame placement, intra-operative CT with frame, and surgery with micro-electrode recording (MER). A significant trend of decreased accuracy of secondary lead placement in bilateral implantations in the x -direction was noted, which is presumed to be associated with *in situ* tissue shift. Further examination of these procedures revealed that a significant portion of procedure time was associated with attaching and imaging a CT fiducial frame to register patient anatomy with pre-operative imaging, as well as performing MER to confirm target location. By utilizing live guidance for targeting and confirmation in order to circumvent both of these processes, at least a 50% reduction in procedure time is predicted, while minimizing targeting errors associated with tissue shift. These two primary advantages over existing practices — reduction in procedure time and increased targeting accuracy — are simultaneously accomplished by eliminating the secondary image fusion and registration processes, which can be observed in the process flow comparison in Fig. 4.1.

The full system architecture of the MRI robot control system, including details regarding planning software and integration of real-time MR imaging, are described in [89], and in more detail in Chapter 2. The focus of this chapter is the design and evaluation of the robotic manipulator, which is organized as follows: Section 4.3.1 describes the workspace analysis and design requirements for the proposed device, and Section 4.4 describes the detailed design of a system prototype. Results of the MRI compatibility, workflow validation,

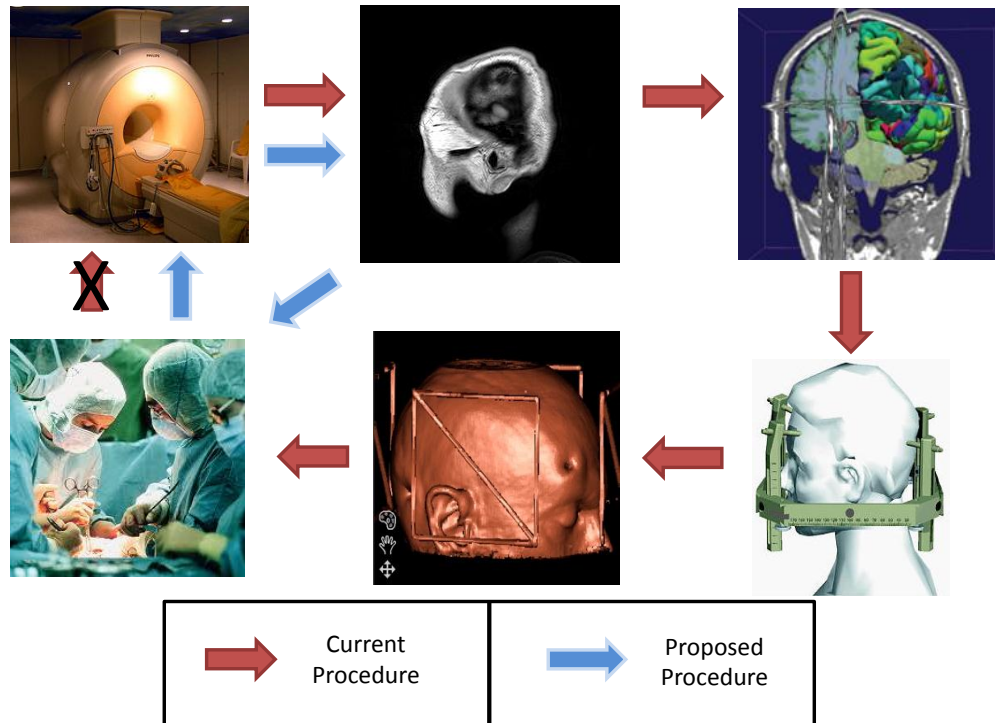


FIGURE 4.1: Depiction of current process flow procedure (red arrows) and proposed process flow procedure (blue arrows). Note how the proposed procedure promises a reduction in procedure time, in addition to allowing for MRI confirmation of electrode placement.

and accuracy are presented in Section 4.6, with a discussion of the system in Section 4.7.

4.2 Contributions

Though DBS therapy is widely and effectively applied, it is a very invasive procedure with a great deal of risks, costs, and trauma involved. The MRI-guided DBS electrode placement system and new procedural structure endeavor to improve patient outcomes from a DBS procedure through increasing targeting accuracy and reducing procedure time, targeting error, trauma, and anesthesia. This development is especially important considering the array of new applications for DBS currently being investigated, including treatments

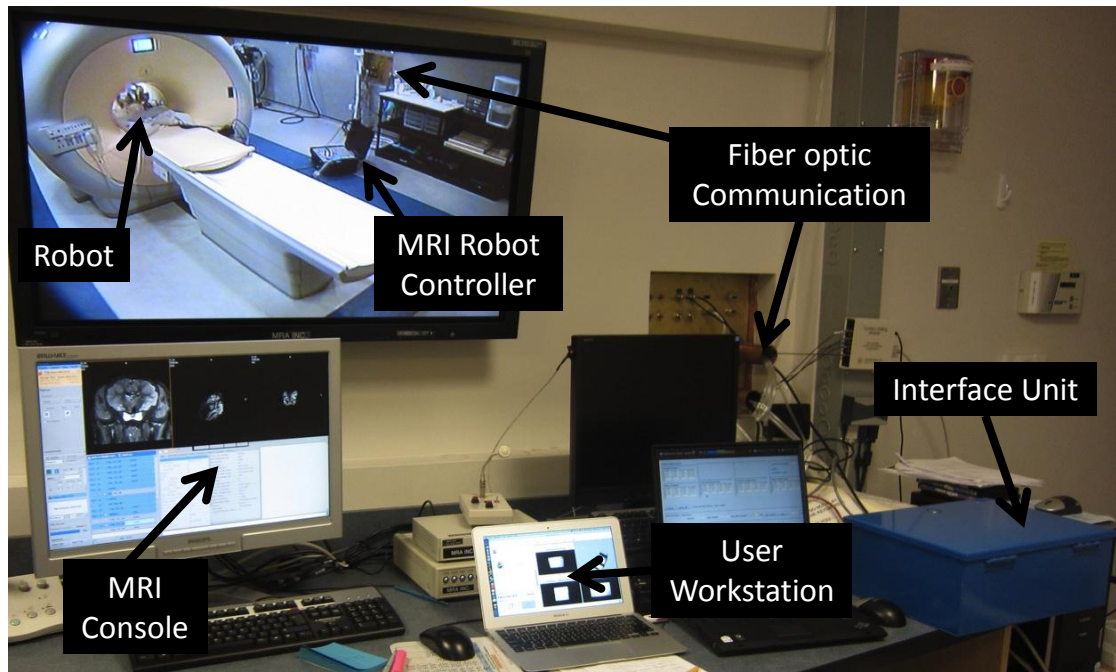


FIGURE 4.2: Configuration of the MRI-compatible neurosurgery system. The robotic stereotactic manipulator is placed within the scanner bore, and the MRI Robot Controller resides inside the scanner room. The Robot Controller communicates with the control computer within the Interface Unit through a fiber optic link. The Robot Control Software running on the control computer communicates with 3D Slicer navigation software through OpenIGTLink.

for essential tremor, dystonia, chronic depression, chronic pain, and others. Primary contributions include the following:

1. Defined specifications to guide the development of the interventional device. The design is driven by kinematic equivalence with current stereotactic frame designs, thus allowing a streamlined FDA 510K clearance process as well as adoption by the surgical community
2. Development and refinement of a stereotactic neural intervention device for live MRI guidance. This device is entirely MRI-compatible, and ergonomically constructed to allow room for the clinician to dextrously manipulate cannula insertion.

3. Improved procedure plan. While the actual intervention pathway planning remains identical, procedure preparation is greatly streamlined. By performing the entire procedure with an automated device operating under MRI guidance which has been registered to patient coordinates, lengthy secondary image fusions processes are circumvented.
4. Validation of the complete system in terms of MRI compatibility, manipulator level accuracy, and image-guided accuracy.

4.3 Design Requirements

4.3.1 Workspace Analysis and Specifications

The workspace and working envelope are tightly constrained in the scanner bore. For development and testing of this system, a Philips Achieva 3T system with a bore diameter of 60cm was targeted. With the bed in place, this leaves 45cm clearance for patient and robot. An average human cranium is $20\text{-}25\text{cm}$ from forehead to occiput, leaving a clearance of approximately 20cm between the forehead and the top of the scanner bore if the patient's cranium is secured very close to the surface of the bed, as can be seen in Fig. 4.3.

The typical range of motion of a DBS electrode placement stepper drive is approximately 50mm . A stepper drive is a precision insertion device which is used to precisely control the depth of insertion of the DBS electrode delivery cannula. In order to accommodate a plurality of stereotactic procedures, up to 75mm of insertion depth is allowed. In order to clear the skull and imaging coils, the mechanism must sweep an arc of at least 15cm in radius from the target point. While

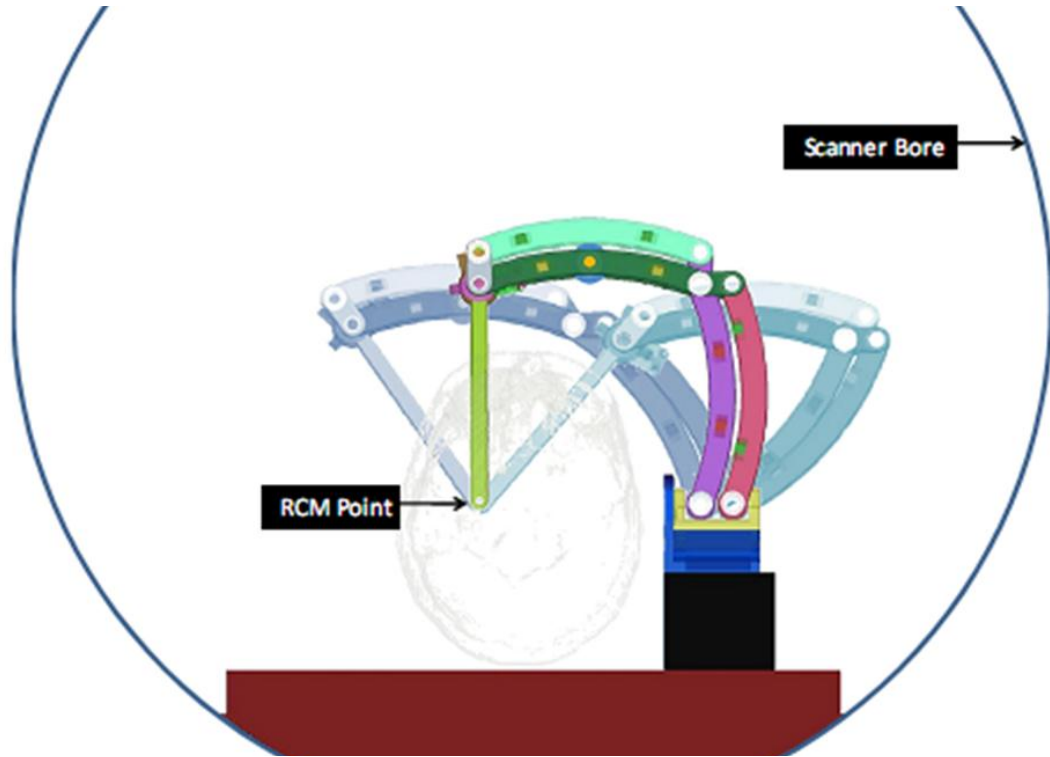


FIGURE 4.3: Diagram depicting the relative size of the scanner bore, an average sized adult male skull, and the bore of a diagnostic scanner.

it is desirable to create a system that will support all procedures currently performed with a manual stereotactic frame, the constrained geometry of the bore makes accommodating this goal with a single mechanism impractical. To allow for future expansions to functionality, the system has been created with a modular architecture such that portions of the mechanism may be replaced with additional devices optimized for other procedures. To enable the range of motion required for typical DBS lead placement, the proposed manipulator is designed to allow 60° of motion from the axial plane symmetric about the vertical. In the sagittal plane, the required range of motion is up to 60° from the vertical, as derived from [49], [90], and [91]. Three prismatic axes coupled with two perpendicular angular axes with precision motion control can accomplish this task, with a predicted final resolution of $0.1mm$ for the robotic mechanism at the tool placement tip.

4.3.2 Performance Requirements

Fig. 4.4 shows a traditionally used manual stereotactic frame (left) and the designed robot prototype (right), demonstrating how the DOF are distributed so as to maintain kinematic equivalence with the stereotactic frame. The first realization of the system provides three prismatic motions ($DOF\#1 - DOF\#3$), two angular motions ($DOF\#4$ and $DOF\#5$), and a manual cannula guide ($DOF\#6$). In future designs, actuated cannula insertion may be implemented to allow complete closed-loop control of the insertion procedure based on real-time MR imaging. In many modern DBS electrode insertion procedures using a stereotactic frame, a set of x , y and z coordinates are used to set the target point, and a set of θ_1 and θ_2 arc angles to align the orientation of the electrode cannula about the target location. To mimic that functionality, a 2-DOF remote center of motion (RCM) mechanism is employed, which is equivalent to aligning the motion axes of $DOF\#4 - DOF\#6$ such that they intersect at the target location. Since significant changes in orientation are clinically inadvisable in neurological interventions, the RCM point is set at the target point rather than the typically used insertion point [92]. The accuracy of individual servo-controlled joints is targeted to be the encoder resolution of $0.01mm$, and the cannula placement accuracy of the robotic system itself is targeted to be $0.1mm$ in free space in order to support complete system accuracy, including registration errors, of $1.0mm$, approximating the clinically significant target size for deep brain therapy [90], [93].

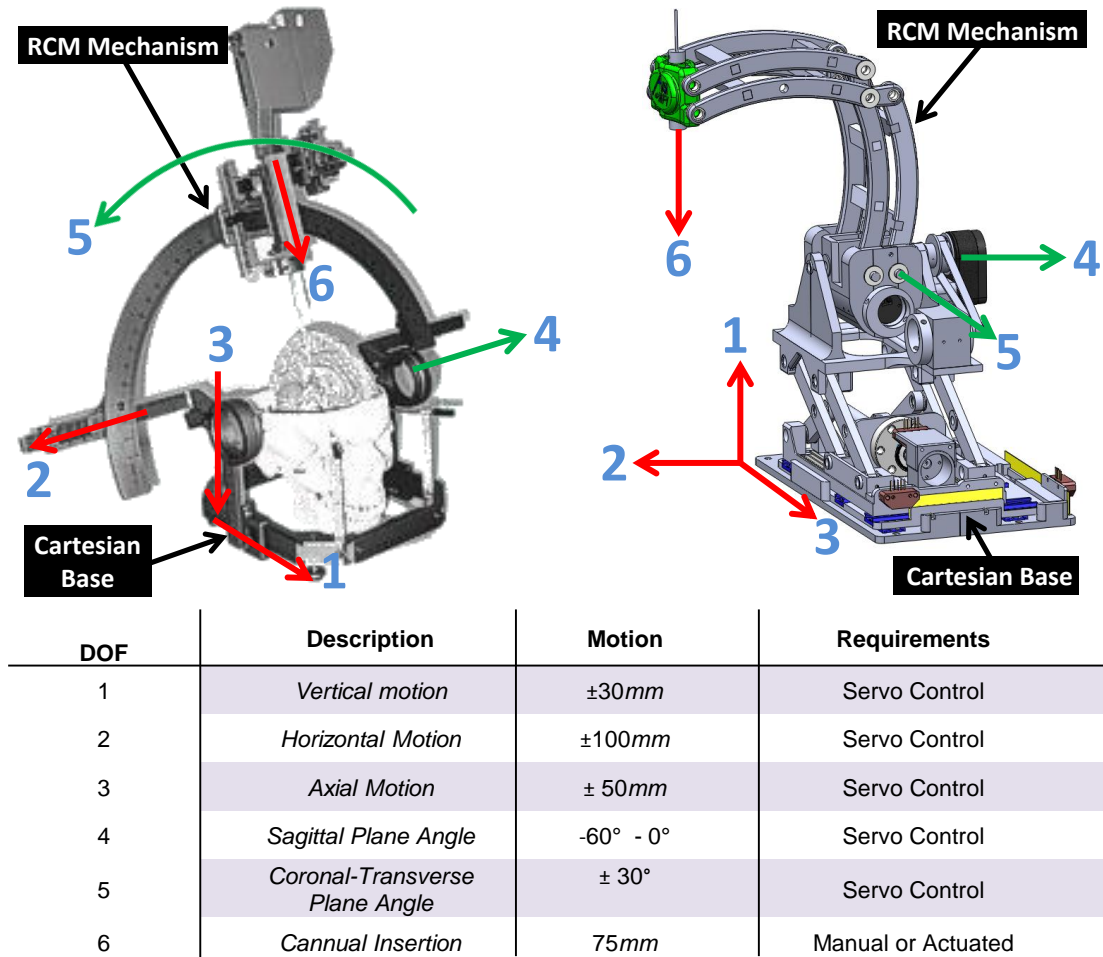


FIGURE 4.4: Assignment of degrees of freedom of a traditional manual stereotactic frame to the proposed equivalent robotic system. Translation DOF in red, rotational DOF in green.

4.3.3 System Architecture

This system was created using the modular MRI-guided development platform presented in Chapter 2, though the majority of the development of the neural intervention system progressed in parallel with the platform. The presented system is capable of registering patient anatomy to robot coordinates, positioning a cannula guide, and performing an intervention without moving the patient out of the imaging space. This enables the use of real-time imaging for precise placement of cannulae in soft tissues. In addition to sequences for structural images, those for diffusion imaging, fMRI, and MR spectroscopy are also available intraoperatively, promising enhanced

visualization and targeting of pathologies. Accurate and robust needle placement devices, navigated based on such image guidance, are becoming valuable clinical tools and have clear applications in several other organ systems.

Planning is performed on pre-procedure MR images or pre-operative images registered to the intra-operative images via fiducial registration. Additionally, multi-parametric image datasets and statistical atlases may be visualized or integrated during planning.

Once the robotic system is registered, this device is removed. Since the robot base is fixed in scanner coordinates, this registration is only necessary once. The insertion axis of the cannula can also be localized via a double walled tube filled with MRI contrast agent located coaxial to the insertion axis. Intraoperatively, MR images are acquired showing the target location and cannula axis. An iterative process of imaging and robot motion allow alignment of the cannula axis through the target within the scanner bore. Once alignment is achieved, the cannula is inserted manually under real-time MR image guidance.

4.4 Mechanism Design

The robotic manipulator must operate with high precision and utilize actuation systems that can be finely controlled with minimal backlash while maintaining MRI compatibility. Similarly to the Leksell frame kinematics on which this device is based, the neural intervention mechanism can be effectively divided into two parts: a prismatic three-DOF base coupled to a three-DOF RCM mechanism. The three-DOF base operates as a cartesian space positioner and

serves to set the location of the RCM point, as shown in Fig. 4.7. The upper RCM mechanism serves to set the insertion angle through its two rotational DOF and then uses the linear insertion DOF to perform insertions.

4.4.1 RCM Mechanism

Many surgical robots that manipulate laparoscopic tools, needles, or other shafts through a single point of entry employ a remote center of motion (*e.g.* [94]), as it allows up to four DOF around the RCM point: three rotational and one translational (depth). A mechanically constrained RCM mechanism, in the form of a parallelogram linkage, was selected for this system, defining the RCM point at the target location making it kinematically similar to a traditional stereotactic frame.

Initial designs of actuation methods for the mechanism included remotely located motors to drive the entirety of the device through cable systems, as shown in Fig. 4.5, though the power transmission system was deemed to be highly susceptible to binding. In addition to this, the materials targeted for mechanism construction were shown to be insufficiently rigid to support a cable system under proper tension without deflecting in an unacceptable manner.

In order to reduce backlash, rotary actuation of RCM DOF are achieved via Kevlar-reinforced timing belt transmissions, which are loaded via eccentric locking collars on the actuator mounting hardware, thus eliminating the need for secondary tension pulleys.

This mechanism was selected in lieu of a double sliding-beam linkage or a pivoted arm robot because it does not suffer from the large

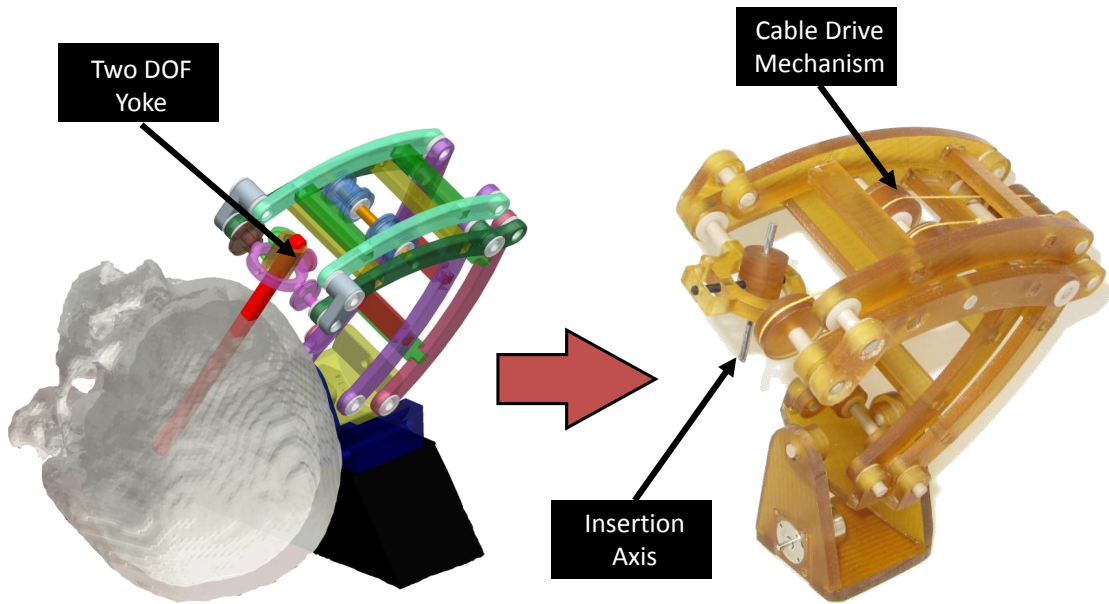


FIGURE 4.5: Initial design of the RCM mechanism. Note the cable-driven design and two-DOF yoke at the head stock to allow for greater flexibility (eliminated in later revisions).

wear surfaces or the high velocities associated with these designs that reduce precision. In addition, by using a parallelogram linkage, an interventional manipulator with a vertical profile of 40mm and a horizontal profile of 60mm has been achieved, leaving a large working volume left within the scanner bore for the surgeon to operate, as shown in Fig. 4.3.

4.4.2 Prismatic Base

As the RCM mechanism atop the neural intervention device can only adjust the angle of the insertion axis so that it is pointing to the RCM point, most commonly used for the target point, the prismatic base is responsible for setting the location of the RCM point. The base mechanism comprises three linear axes: DOF #2 and DOF #3 operate via a direct driver, while DOF #1 is operated via a scissor lift mechanism driven by a rotary actuator and a lead screw, as shown

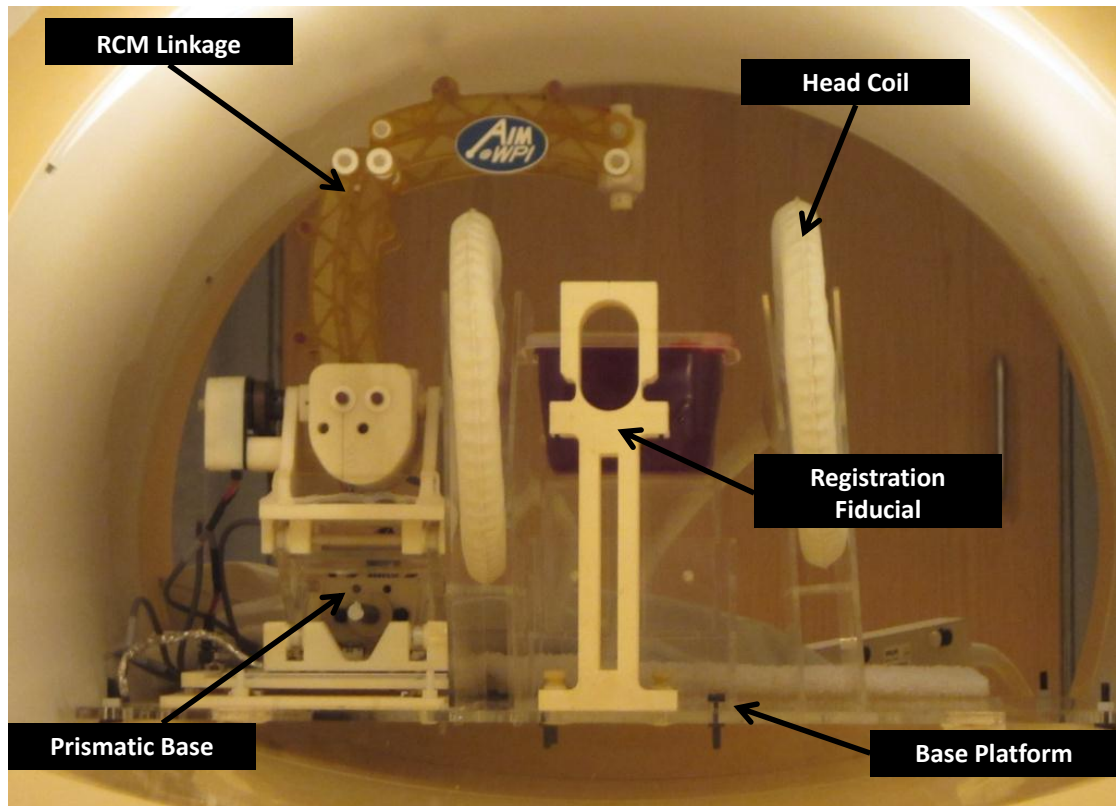


FIGURE 4.6: Final mechanism design of the neural intervention linkage in Fig. 4.7. This method of vertical linear travel was selected for its force magnification through the lead screw mechanism, allowing the vertical lift mechanism’s linear bearings to support the gravitational load of the mechanism normal to the direction of travel. The primary construction material for this mechanism was selected to be polyetherimide (Ultem) because of its high strength, machinability, and suitability for chemical sterilization.

4.5 Application of Modular Device Development Platform

While the mechanism discussed above has been created through the application of the modular MRI guided device development platform discussed in Chapter 2, the specifics of the application of the

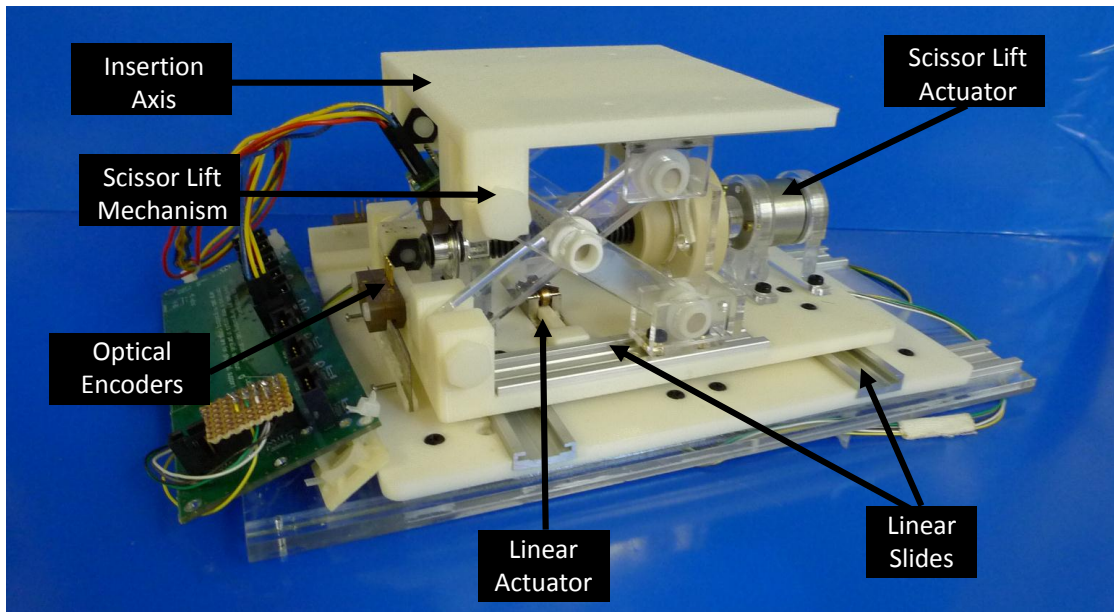


FIGURE 4.7: Prismatic base positioner broken down by degree of freedom and actuation method. Note the two direct drive degrees of freedom and the scissor lift mechanism used to enhance force.

system, including the project specific software created for the neural intervention system will be discussed below.

4.5.1 Robot Controller System

The complete control system shown in Fig. 4.2 comprises three main units: 1) the MRI-compatible robot controller with an electromagnetic interference (EMI)-shielded enclosure containing the electrical systems that directly interface with the robotic manipulator within the scanner room (Fig. 4.8), 2) an interface unit containing ethernet communication hardware and a dedicated computing system which translates high level planning and navigation information into device-level commands, and 3) a user workstation which operates the procedure planning software. The latter two units were constructed of COTS components. The in-room robot controller can be placed as little as 1m from the scanner bore and was specifically developed to

operate mechatronic interventional systems within the scanner bore as described in Chapter 2.

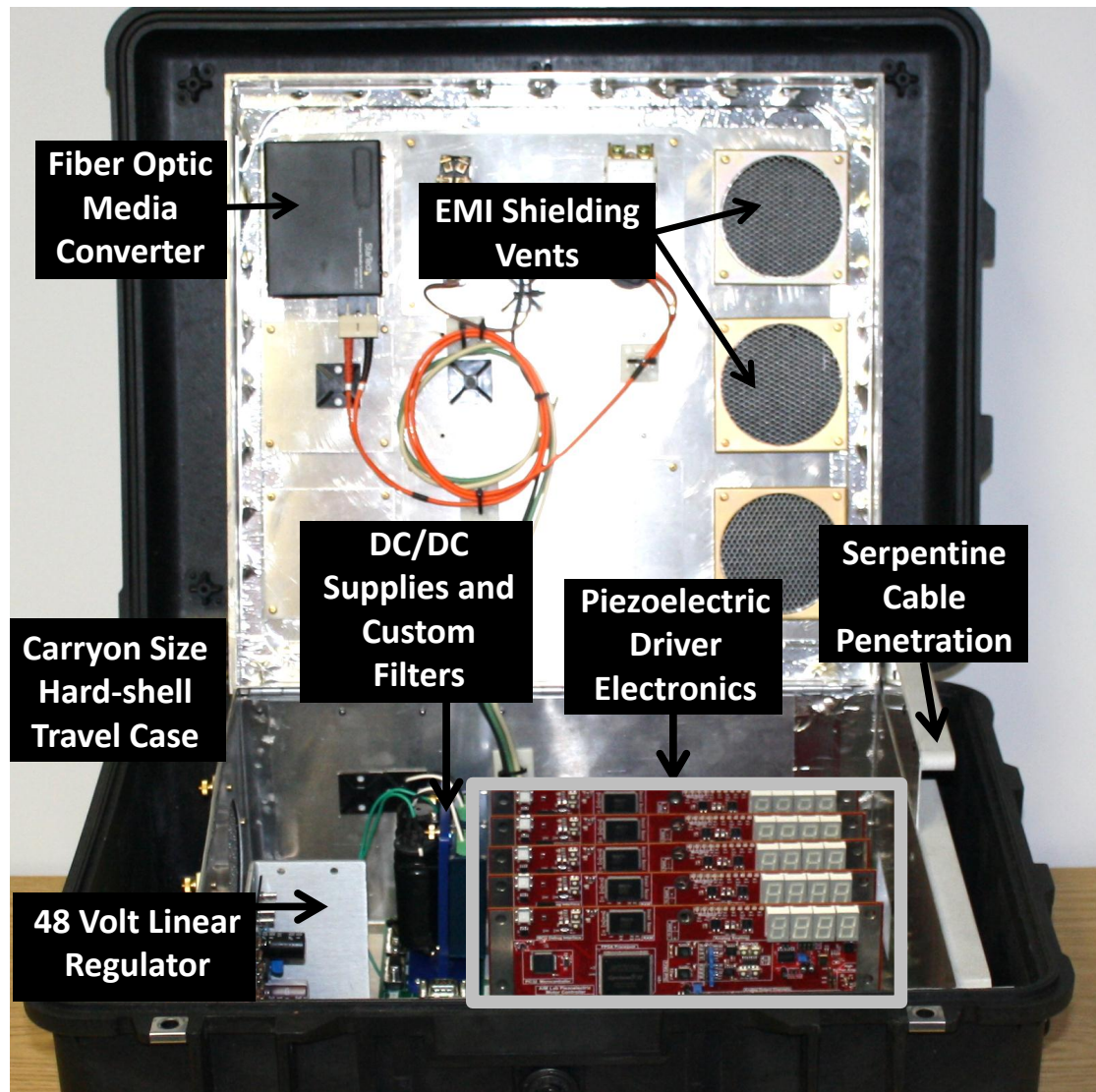


FIGURE 4.8: MRI-compatible robot controller. The shielded enclosure is shown with low-noise power supplies, fiber optic media converter, wave guide for cable penetration, and custom high-precision, low-noise piezoelectric actuator control electronics on an application-specific backplane.

4.5.2 Interface Software

The system supports any navigation software that can provide targets in right-anterior-superior (RAS) coordinates through OpenIGTLink, though it was evaluated using 3D Slicer running on a workstation in

the console room. Note that because RAS coordinates are patient/scanner coordinates, registering to this coordinate system allows direct targeting in live scanner images. A customized graphical user interface (GUI) specially designed for robotic DBS electrode placement is in development. OpenIGTLink, an open-source device connection and communication tool developed for image-guided therapy, is used for the exchange of the components' various types of data, including control commands, position data, and images.

In the planning phase, pre-operative images are retrieved from a DICOM (Digital Imaging and Communications in Medicine standard) server by the navigation software. Registration is performed between the pre-operative planning images and intra-operative imaging within the navigation software. Target points and trajectories for the electrode insertion are selected according to the pre-operative imaging. Once the patient and robot are placed in the MRI scanner, a small stack of MR images is acquired near the expected robot location with the robot orientation set to its centered, home position. These images will capture the fiducial marker affixed to the base of the robotic system (as shown in Fig. 4.11) that can be used to determine the exact position of the base of the robotic manipulator within RAS coordinates. Once the base of the system is registered in RAS coordinates, a series of frame transformations can be used to determine the manipulator position within RAS coordinates, as shown in Fig. 4.9. After the registration phase, the robot controller can accept target coordinates represented in the image (patient) coordinate system using standard RAS coordinates and utilize inverse kinematics to resolve joint-level commands required to achieve the intended pose.

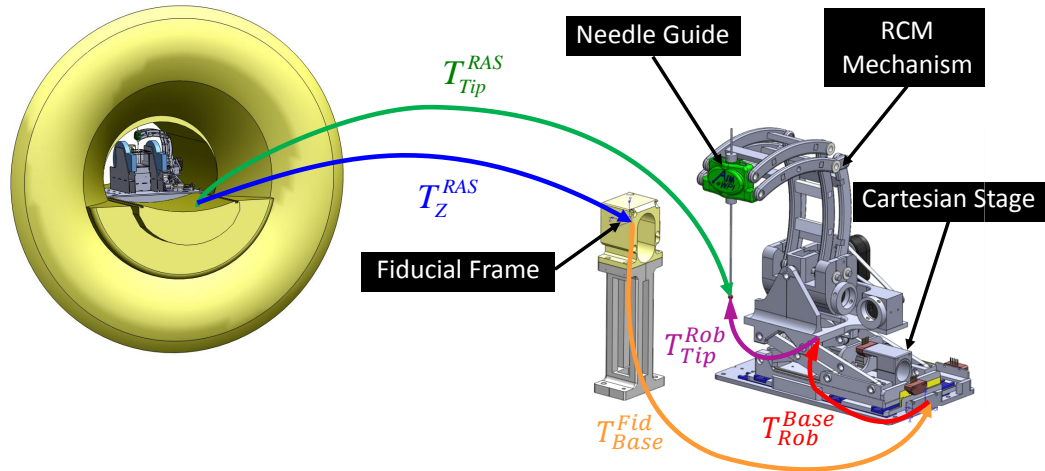


FIGURE 4.9: Frame transformations between the neural manipulator, registration fiducial, and RAS coordinates. Note that the fiducial frame shown represents any registration device that can be used to determine manipulator position in image space and is not restricted to the Z-Frame discussed earlier.

In the current system, the electrode and cannula are inserted manually through the robotically aligned guide sleeve. The axis of the guide sleeve can be confirmed based on imaging coaxial tube of MRI contrast fluid placed in the robot's needle guide. Ma *et. al.* have developed a helical cylindrical tracking fiducial adapted for use with this robotic system, which has been shown to provide a complete 6-DOF registration of the manipulators headstock, rather than a simple on-axis confirmation [95]. Needle advancement in the tissue can be visualized in two complementary ways: 1) a 3D model view of the robot end effector combined with pre-operative 3D images resliced in planes intersecting the insertion axis and 2) 2D real-time MR images acquired from the planes longitudinal or perpendicular to the needle path. The interface software enables “closed-loop” needle guidance, where movement of the robot is captured by the MR imaging and immediately fed back to the physicians to aid their decision for the next action. The reason for keeping a human in the loop is to

increase safety by allowing progress to be monitored using the live MR images. The robot fully aligns the cannula guide sleeve before any contact is made with the patient. If necessary, the placement is adjusted in response to the MR images.

4.6 Validation

To date, there have been a series of experiments with this system, mainly focusing on the ability of the system to precisely generate and control motion while remaining MRI-compatible. This testing process began with image compatibility testing of the complete actuation and encoding system, followed by accuracy analysis. Mechanical performance was tested first by verifying the joint-level accuracy of the system, then proceeding to benchtop validation with an optical tracking system (OTS), and finally culminating in image-guided accuracy analysis with a Phillips Achieva 3T scanner.

4.6.1 MRI Compatibility

All of the modules presented earlier have been tested individually and as an integrated whole, to ensure that no aspect of the system creates an unacceptable amount of image interference.

Four imaging sequences were assessed, as detailed in Table [4.1](#):

1. Diagnostic T1W fast gradient echo
2. Diagnostic T2W fast spin echo
3. Real-time imaging fast gradient echo
4. Functional echo-planar imaging

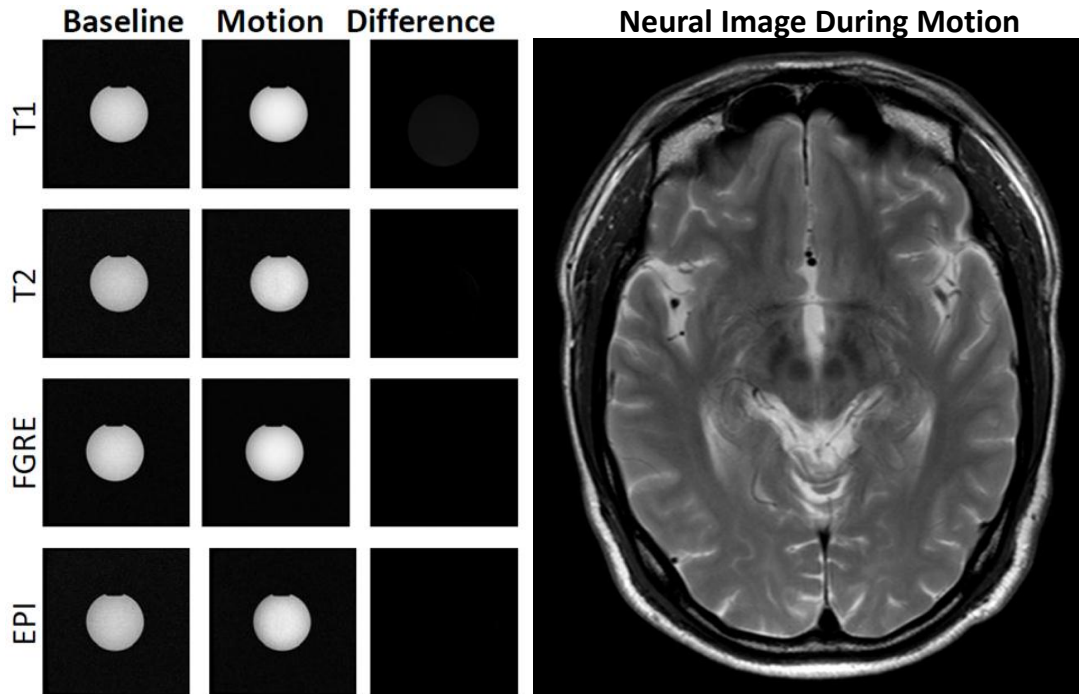


FIGURE 4.10: Left: Image subtraction analysis of MRI compatibility of the neural intervention system. Right: High-resolution MR image of anatomical structures in the brain during motor actuation, showing low noise, high contrast, and sharp boundaries of anatomical structures.

The specific scan protocols are the same as those defined by Wang *et al.* in [67]. The metric of choice to measure signal degradation is the signal-to-noise ratio (SNR), which compares an image section that is expected to be 100% signal with an image section expected to be 100% dark, as shown in Fig. 4.10. A series of 10 images were taken with each of the four protocols. The SNR of each of these images was then computed, and the averages of these ten scores are presented in Table 4.1. The results of the total system demonstrate a very low amount of interference, as shown in Fig. 4.10, with the normalized SNR never decreasing more than 2.3%. Currently there does not exist an accepted standard for suitable decrease in the SNR of MR images when used for interventional guidance so the SNR loss levels observed are very close to scanner variance under the studied imaging protocols.

TABLE 4.1: Experimental Results of MRI Compatibility Evaluation showing SNR and percentage change

Protocol	Baseline	Motor Off(% Change)	Motor Running(% Change)
T1W	148.70	150.5 (1.24%)	149.8 (0.76%)
T2W	620.40	631.8 (1.84%)	629.4 (1.46%)
FGRE	141.20	142.8 (1.19%)	141.6 (0.30%)
EPI	228.40	223.6 (2.09%)	226.3 (0.92%)

4.6.2 Accuracy

The accuracy of the neural stereotaxy system was analyzed using two methods, benchtop validation using an optical tracking system (OTS), as well as validation of the complete system using MRI guidance. Both OTS and image guided validation were performed to decouple targeting errors associated with the robotic system from errors associated with image based registration and targeting.

4.6.2.1 Benchtop OTS Evaluation

The experimental setup used to assess system-level mechanical accuracy is shown in Fig. 4.11. A Polaris (Northern Digital Inc, Waterloo, Ontario) optical tracking system was used, with a passive 6-DOF tracking frame attached to the robot base and an active tracking tool utilized on the end effector. To ensure the device achieved kinematic equivalence with a Leksell surgical frame, mechanical performance of the RCM mechanism was assessed in addition to the system accuracy as a whole.

The experiment was a two step procedure, consisting of robot RCM mechanism calibration and robot end effector evaluation. The first

procedure was performed by moving the mechanism through multiple orientations while keeping the Cartesian base fixed, and performing a pivot calibration to determine tool tip offset. The root mean square (RMS) error of this indicates RCM accuracy. After successfully calibrating the RCM linkage, the robot was moved to 6 targets, with each target consisting of 5 different orientations. Three groups of data were recorded: desired needle transformation, reported needle transformation as displayed with optical encoders, and measured needle transformation from OTS. The experimental data were analyzed to determine tip position error ($1.0mm$), orientation error (2.0°), and RCM intersection point error ($0.3mm$), as given in Table 4.2.

4.6.2.2 MR Image-Guided Evaluation

The experimental setup used to assess system-level accuracy within the scanner is shown in Fig. 4.11. Ceramic needles (so as to isolate robotic system accuracy) were inserted into a gelatin phantom and imaged with a high-resolution $0.5mm^3$ 3D neuroimaging sequence to assess the robot instrument tip position. This experiment accurately reflects the effectiveness with which the robotic system can target an object identified within MR images. The experimental procedure is as follows:

1. Initialize robot and image targeting fiducial.
2. Register robot base position with scanner coordinates.
3. Remove targeting fiducial, and set to the “home” position.
4. Translate base to move RCM point to target location.

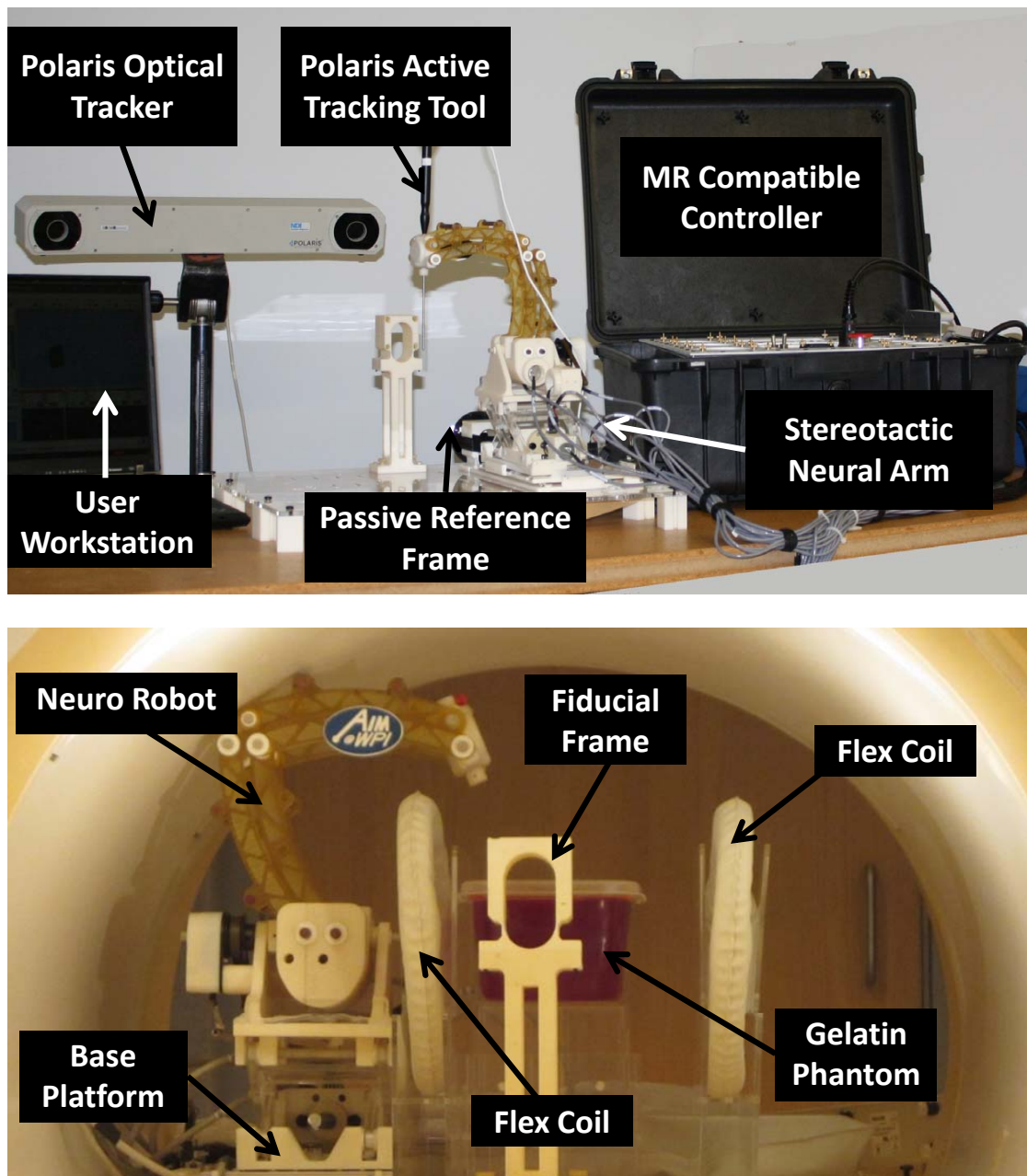


FIGURE 4.11: Top: Experimental setup for benchtop OTS accuracy study. Bottom: Placement of the robotic device within scanner bore for image-guided accuracy study.

5. Rotate RCM axes to each of five insertion trajectories, insert ceramic needle, and image.
6. Retract needle and translate base axes to move RCM point to the next target location, and repeat rotations, insertion, and imaging.

The insertion pathway (tip location and axis) of each needle insertion was determined from the MR image volumes, as shown in Fig. 4.12 for one representative target point. The best-fit intersection point of the five orientations for each target location was found, both to determine the effectiveness of the RCM linkage and to analyze the accuracy of the system as whole. The result demonstrated an RMS position error of approximately $1.4mm$ and an average angular error of approximately 2.0 degrees, as shown in Table 4.2. This result is especially promising when considering that it is a minimal increase in targeting error over the OTS experimental results. Table 4.2 gives three metrics for analyzing system error: tip position, RCM position, and insertion angle. Tip position error is a measure of the distance between a selected target and the actual location of the inserted cannula. RCM position error represents an analysis of the mechanism's performance as an RCM device. For these measurements, a single RCM point is targeted from multiple angles, and the average minimum distance from a single point of all the insertion axes is determined using least squares analysis. Insertion angle error is measured as an angular error between the targeted insertion angle and the actual insertion angle as determined via the OTS system during the benchtop experiment and via image analysis for the MRI-guided experiments.

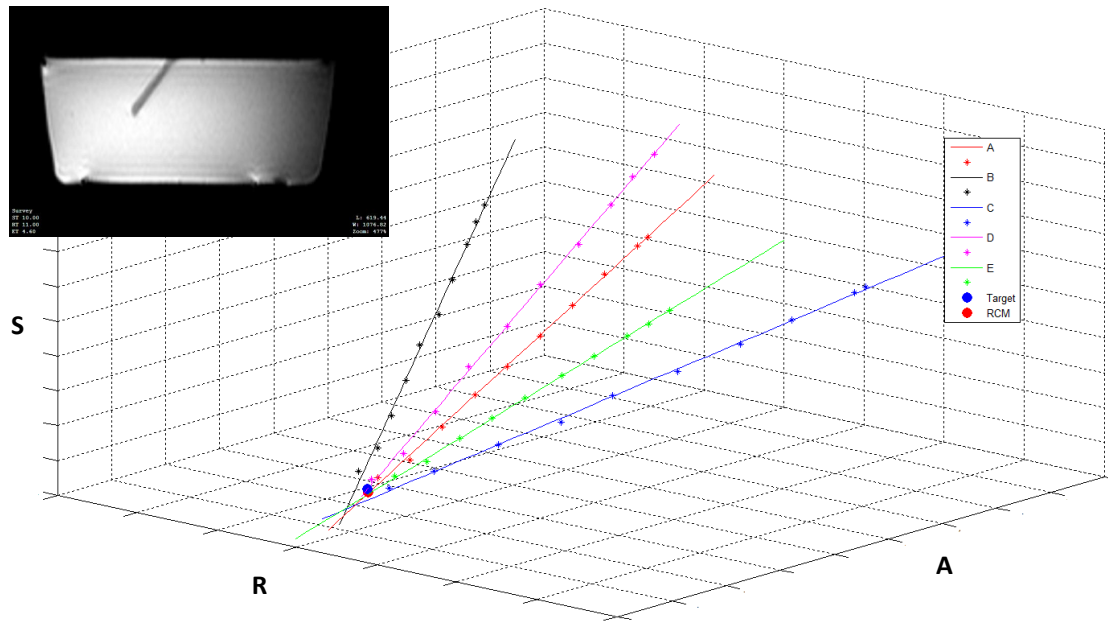


FIGURE 4.12: Plot of intersection of multiple insertion pathways at a given target location from MRI data. Each axis is 40mm in length. Inset: MRI image of phantom with inserted ceramic cannula.

TABLE 4.2: Analysis of OTS and Image-Guided Accuracy Studies

		Tip Position (mm)	RCM Position (mm)	Insertion Angle (Degree)
MRI-Guided	Maximum Error	2.130	0.594	2.789
	Minimum Error	0.512	0.474	0.849
	RMS Error	1.380	0.542	2.029
	Standard Deviation	0.449	0.049	0.579
Optical Tracker	Maximum Error	1.560	0.437	3.069
	Minimum	0.479	0.224	0.896
	RMS Error	1.088	0.330	2.058
	Standard Deviation	0.283	0.051	0.755

In addition to the quantitative analysis of the system accuracy and placement using gel phantoms, a more qualitative set of experiments was performed with an animal cadaver. This experiment was designed to assess workflow and usability in a process more closely related to the actual clinical function of the system. For this procedure, the same experimental setup as the gel phantom experiment was used, however instead of a gel phantom, the head of a sheep was

used, shown in Fig. 4.13.

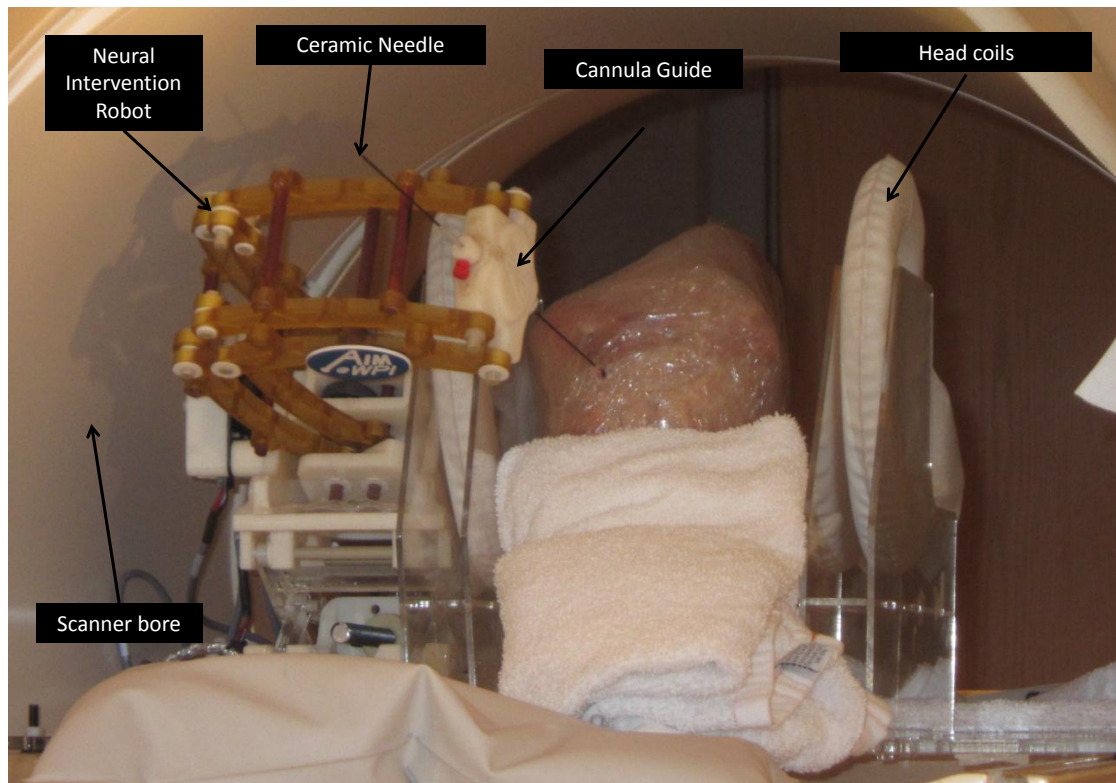


FIGURE 4.13: Experimental setup using a sheeps head targeting cadaver.

The sheeps' head is wrapped in a plastic covering for sanitary reasons, and placed on the mount for the gel phantom in the previous experiment. A hole was drilled in the skull to allow for the insertion of a ceramic needle using the needle guide on the robotic systems headstock. The insertion track made with the drill bit was targeted effectively enough by the robot to allow for the insertion. Though the needle itself cannot be imaged by the scanner because it is made out of ceramic, the void left by the needle insertion is clearly visible in Fig. 4.14.

4.7 Discussion

A prototype integrated robotic system for stereotactic neurosurgery has been developed, and initial testing to determine the potential

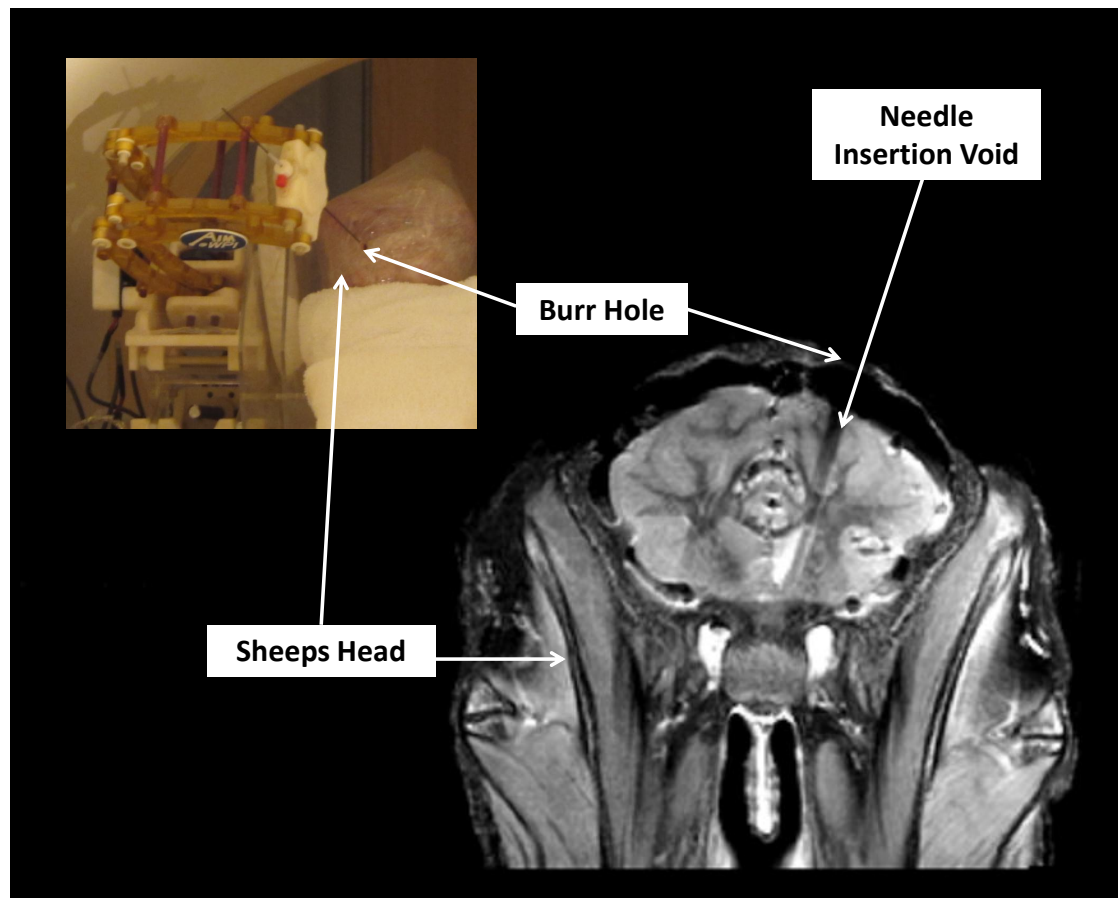


FIGURE 4.14: MRI Image taken of the sheeps head showing the burr hole targeted and the needle insertion pathway. Inset shows robot and corresponding ceramic needle and burr hole.

clinical efficacy has been performed. The system has been designed such that it is scanner-independent, portable, and capable of being deployed and utilized with nearly any diagnostic high-field MRI scanner currently used for neural imaging. In addition to the system's scanner-independence, it has been designed to be mechanically constrained so that it is kinematically equivalent to a manual stereotactic frame in order to reduce sources of error and improve clinician confidence.

When developing MRI-compatible robotic systems, one of the primary considerations is maintaining acceptable image quality during the actuation of the system. While others have traditionally

avoided piezoelectric actuation due to extreme levels of SNR loss during motor operations, such as observed by Krieger *et al.* [25], [1], the tremendous potential actuation precision, high stopping speed, holding force, and inherent MRI safety of piezoelectric actuation indicated the value of investigating methods to use them. The modular system for driving and control of piezoelectric devices to operate the actuation and control system has been shown to be both MRI-compatible and safe, offering less than 2% SNR loss during live motion while imaging, as demonstrated by Wang *et al.* [67] and Cole *et al.* [89]. Using this system streamlined the development process from conception to implementation of the stereotactic neural device by providing a “safe harbor” list of actuation and sensing equipment as well as design guidelines for the construction of the mechanism, which together eliminate compatibility issues.

While the many advantages of live image guidance and robotic surgery have been well established by groups such as Nathoo *et al.* [44] and Gassert *et al.* [43], to date there is no effective system to mimic a stereotactic neurosurgery device currently in use. The system presented here is differentiated from the Neuroarm developed by Sutherland *et al.* [96], a generalized neurosurgical manipulator for operation under MRI guidance, in that this system is specifically a stereotactic surgical device that is mechanically constrained to be kinematically equivalent to a currently used manual stereotactic device. This will increase clinician comfort when operating the device as well as limit the system’s complexity, cost, and required training for operation and maintenance. The interface is very similar to that used by neurosurgical planning software, and the method for registering MR images to patient and robot coordinates is both effective and efficient. Combining these aspects, the system provides

a clear pathway through clinical trials and FDA clearance to improved patient outcomes by making a significant improvement in procedure efficiency and effectiveness with a minimum of change to a thoroughly-tested methodology.

While positioning accuracy of the prototype system is not yet at the sub-voxel level desired, the sources of these errors are thought to be apparent. The 3D printed materials utilized in the construction of this device are very useful to rapidly create a mechanism for initial analysis. However upon disassembly, plastic deformation of the pivot locations of the parallelogram linkage were observed and are believed to have added to system inaccuracies. In addition, large transmission distances on the two belt drive axes may also be associated with targeting inaccuracies. These arguments are supported by the joint encoder-level accuracy shown, along with the demonstrated accuracy of the fiducial registration system used. Initial trials of the system when constructed of high performance materials will most likely be targeted at STN DBS electrode placement. The reduced trauma, procedure time, cost, and targeting errors associated with performing neural stereotactic procedures under live MRI guidance will make stereotactic procedures available to a wider range of patients, as well as improving patient outcomes.

Chapter 5

Conclusions

The primary contributions of this dissertation relate to enabling the use of direct, live MR imaging to guide and assist interventional procedures. These are the two focus areas: creation both of an integrated MRI-guided development platform and of a stereotactic neural intervention system. The integrated series of modules of the development platform represent a significant advancement in the practice of creating MRI guided mechatronic devices, as well as an understanding of design requirements for creating actuated devices to operate within a diagnostic MRI. This knowledge was gained through a systematic approach to understanding, isolating, characterizing, and circumventing difficulties associated with developing MRI-guided interventional systems. These contributions have been validated on the levels of the individual modules, the total development system, and several deployed interventional devices. An overview of this work is presented below with a summary of contributions and lessons learned along the way.

5.1 Summary of Work

5.1.1 Interventional Development System Architecture

The modular development system presented has been shown to streamline the development of new devices in the rapidly expanding field of MRI-guided interventional robotics. Whereas previously, large teams with diverse engineering skill sets were required to develop and deploy a device. This integrated system has enabled the rapid development and deployment of a device by as few as a single individual. Furthermore, it has been shown through the presentation of the work presented in this dissertation that when used, this system allows all of the development and research efforts to be put toward a researcher's primary contributions, since supporting infrastructure has already been stabilized. While there are no fewer than four devices currently utilizing this system in the Automation and Interventional Medicine Laboratory, other laboratories such as those in the LCSR at Johns Hopkins University and the Wyss Institute at Harvard University are also currently leveraging this system to maximize the effectiveness of their research. Some examples of projects in addition to the ones already shown can be seen in Fig. [5.1](#).

5.1.1.1 Piezoelectric Actuator Driver

The multimodal piezoelectric actuator has demonstrated image compatibility better than available industry devices while under operation — not just for one actuator, but for every actuator it currently supports. In addition to being the only published method, to our knowledge, for driving Piezo LEGS, Nanomotion, and PCB motors within an MRI without contributing more than 2% SNR loss, it can

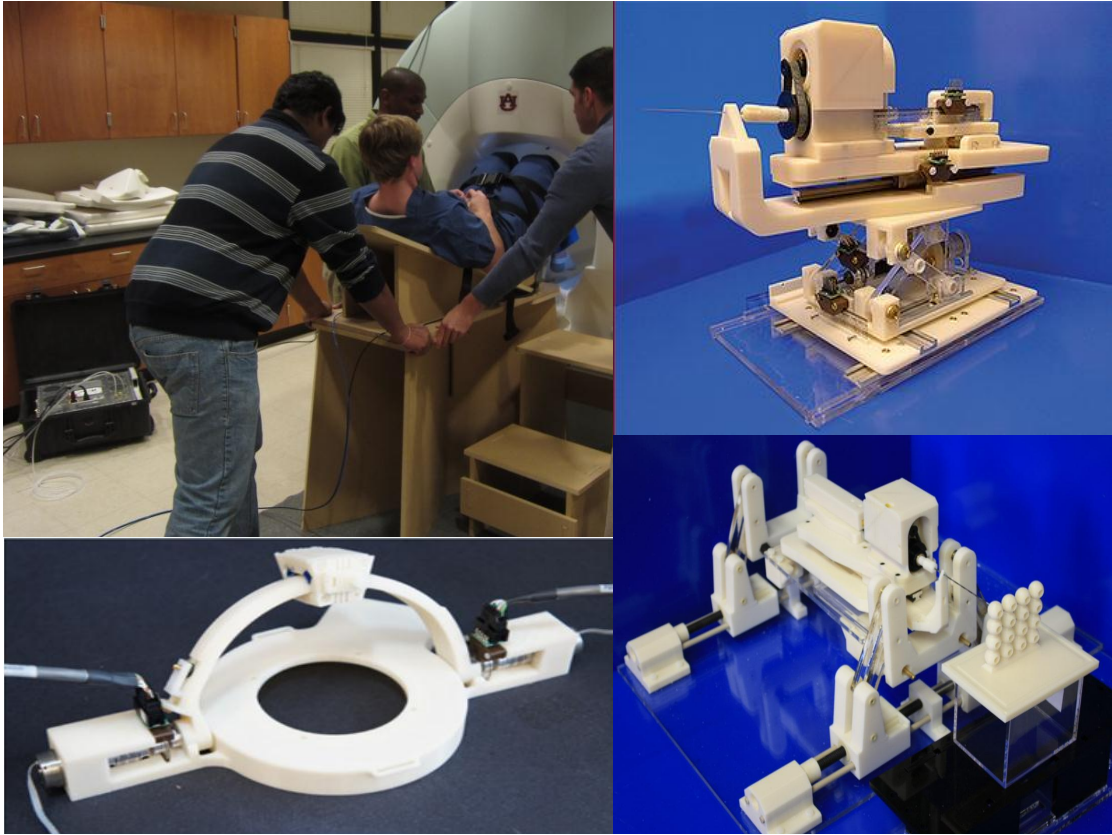


FIGURE 5.1: Upper left: Neuromuscular damage investigation device at warrior research center at Auburn University. Top right: Percutaneous prostate intervention device developed by Su *et. al.* at the AIM lab in Worcester Polytechnic Institute. Bottom right: Needle driver angulation stage developed by Xiaohan *et. al.* at the AIM Lab in Worcester Polytechnic Institute. Bottom right: Neural intervention device developed by Wu *et. al.* at the Wyss Institute in Harvard University [97]

operate each of these devices without any hardware modification, and seamlessly integrates with the modular development platform. This is currently the only system capable of driving all of these actuators from a single piece of hardware, regardless of MRI compatibility. This allows users to develop a mechanism based on any of these actuators, which have a wide range of operational requirements, but still utilize a single primary control system to operate them. Finally, this unit is capable of integrating advanced control methods, including haptic feedback and board-level encoder-to-encoder control, thus offering the ability to introduce much more advanced operation and control techniques in the future such as coordinated motion,

microstepping, haptics and teleoperation.

5.1.1.2 Switching Regulator Guidelines

Despite obvious benefits in terms of weight, reliability, and efficiency, switching regulators for use in an MRI environment have not been typically pursued due to their inherent tendency to produce noise within the range easily detected by scanners.

While the original power supply design described in 2.4.4 currently needs to be refined for stability and robustness, the design principles used to construct this device have been validated through qualitative analysis of the initial prototype. Further strengthening the validity of the design methods of this power supply is the successful deployment of a subsequent power supply system created by modifying COTS power supplies to comply with the original design requirements. As the development of more capable and complex MRI-compatible electronics progresses, the ability to utilize switching regulators instead of only linear regulators or battery-operated power supplies will greatly reduce the size, cost, weight, and power consumption of these devices.

5.1.1.3 E.M.I. Management Practices

A modular method has been presented for enclosing and supporting electronic equipment within the scanner room, which effectively allows electronic packages with high frequency, low amplitude noise to be present in the scanner room without causing image degradation. This unit integrates the majority of the infrastructure of the scanner

room controller in a single robust device, and represents the culmination of several discrete areas of investigation. The power supply system within this box is the final expression of the methods developed for constructing high efficiency switching regulators capable of operating within the scanner without interfering with image quality. In addition this device expresses the serpentine waveguide penetration concepts as a tool-less bulkhead penetration. This penetration allows equipment within the unit to be reconfigured easily without requiring machining or tooling. Finally, the fiber optic communication system coupled with the backplane signal aggregator ties the remaining equipment within the case together in a robust and reconfigurable manner. The sum of all of these disparate parts allows the unit to be easily and reliably reconfigured, transported and deployed.

5.1.2 Piezoelectric Actuator Analysis and Characterization Hardware and Methods

High precision position control of piezoelectric motors is well established and is the basis for the operation of a majority of our current devices; however, the logical extension of advanced robotic systems is toward more complicated forms of control, including motion and force control. In addition to the complex operating principles of PZAs, there is difficulty in directly observing and analyzing PZAs response to stimuli. The presented observational methods and experimental equipment developed allows users to leverage the functionality of a modular system to rapidly collect and analyze PZA operating characteristics and apply this ability to developing and characterizing more effective motor control methods. While this equipment and methods have not yet produced finalized original control methods,

the ability to directly correlate sensor information with motor driver output allows for the rapid analysis of motor stimuli. This capability extends the development platform beyond the simple act of device creation and into the realm of advanced control development and validation.

5.1.3 Stereotactic Neural Intervention System

The goal of creating an image-guided stereotactic neural intervention system was to improve patient outcomes by means of increasing placement accuracy through the use of direct MR imaging for guidance and confirmation and by reducing procedure time through circumventing secondary registration techniques. The AIM lab has created and refined this system through iterative revisions and demonstrated an effective registration technique. In addition, the AIM lab has validated the total system accuracy using both optical bench-top experimentation and MR image-guided experimentation as well as qualitatively demonstrating the possibility to greatly reduce procedure times with our proposed workflow. The construction and testing of this system has demonstrated the viability of the modular MRI-guided robot concept.

5.2 Impact and Future Work

5.2.1 MRI-Guided Development System

The field of MRI-compatible robotics has been expanding for several years as more and more publications demonstrate the value in

enabling direct imaging for guidance and confirmation during interventional procedures. Understandably, as this field has developed, there has been an inclination toward directly developing interventional systems targeting specific procedures and focusing on the clinical benefits. The modular development platform has enabled future researchers to focus on new clinical applications by using a common infrastructure, reducing the resources required to move from concept to prototype.

The presented development system allows support requirements to be reduced to a single person making a single contribution. In other words, the system lets researchers focus on their core research areas rather than impeding development with repeating infrastructure construction. This maximizes the benefit gained from research funding and will leverage more rapid and effective development of MRI-guided devices. Moreover, this dramatic reduction in requirements to develop and deploy an MRI-guided device will greatly expand the population of laboratories and researchers capable of entering the field of MRI-guided devices.

Future work in the development of this system, which is already underway, includes the development of new hardware and software modules, as well as the application of the motor characterization capabilities to develop new control methods.

5.2.2 Neural Intervention System

Though the specific clinical motivation of the interventional device presented is DBS electrode placement, at its core the device is a stereotactic neural intervention unit. It has been demonstrated that

potential improvements over traditional procedures with nonexistent or limited intraoperative imaging capabilities include more accurate placement, fewer repeated procedures, and large savings on procedure time, patient trauma, and costs. This is accomplished through *in situ* live image guidance. These reductions in risk can logically be extended to other types of procedures, which can be targeted in the future. Other uses of this device currently being targeted by the AIM Lab include, but are not limited to, MR image guided conformal thermal ablation, ICH evacuation, and gene therapy. In addition to the support of an expanded repertoire of interventional procedures, the capabilities of the neural mechanism itself are being expanded, with automated needle driver submodules, integrated head coils, and automatic linkage optimization procedures already in progress.

5.3 Dissertation Contributions

The major contributions of this dissertation are as follows:

1. Developed an integrated, MRI-guided device development platform which has been shown to enable a single individual with a narrow area of expertise to develop and deploy an MRI-guided device.
2. Shown the feasibility of and potential process improvements from integrating live image guidance with stereotactic neural interventions. Future related work is informed by the success of the current device and the functionality of the development system.

3. Demonstrated the viability of the modular development platform through the creation of an MRI-guided stereotactic neurosurgery system.
4. Refined the operating procedures of a wide variety of styles of piezoelectric actuation and clearly demonstrated the feasibility of utilizing piezoelectric actuation for intervention during MRI without causing unacceptable image interference under a variety of imaging modalities.

5.4 Lessons Learned

The most important lesson learned from this experience is *know your resources*. There is a large difference between something being possible and something being practical. The decision to start developing a variety of piezoelectrically actuated interventional devices at the creation of the Automation and Interventional Medicine laboratory was driven by the thought that the pneumatic control system — developed for percutaneous prostate biopsy developed by Fischer *et al.* at Johns Hopkins University— would easily be reproducible and could be adapted to operate piezoelectric actuators. While this ultimately turned out to be *possible*, the work involved in adapting the system to drive complex electromechanical actuation in lieu of pneumatic actuation turned out to be the driving force behind the bulk of this dissertation. Unfortunately, each layer of infrastructure supporting piezoelectric actuation within this system revealed another host of problems, to the point that it became apparent that an MRI-compatible electronic support infrastructure was an area of research in itself which needed to be investigated. It is hoped that the shift in

focus of this research, from the advanced characterization and development of stereotactic neural intervention equipment to a dual track of development of MRI-compatible electronic infrastructure and deployment of an initial stereotactic neural intervention platform, will highlight the fact that every development process needs to begin with a complete and honest assessment of technology and resources available, including a catalog of your own capabilities and the capabilities of the people you are working with. To put this in systems engineering terms:

“An operational deficiency does not equate to a technological opportunity.”

Appendix A

Characteristics of Electrical Requirements for Driving Piezoelectric Actuators

This appendix serves to present requirements of electronic signals used to drive piezoelectric actuators, which were used in part to derive requirements for the piezoelectric actuator driver. Some of this waveform information was obtained from the manufacturer of said actuators, and some was obtained experimentally. Digital versions of these driving waveforms and the files used to load them on to the driving electronics package are located in the supplemental DVD.

A.1 Quasistatic Actuators

The Piezlegs quasistatic actuator is designed to operate at a driving frequency of between 750 Hz and 3 kHz, on four synchronized channels operating between 0 and 48 volts. Others such as Merry *et. al.* have operated these motors at frequencies down to 50 Hz

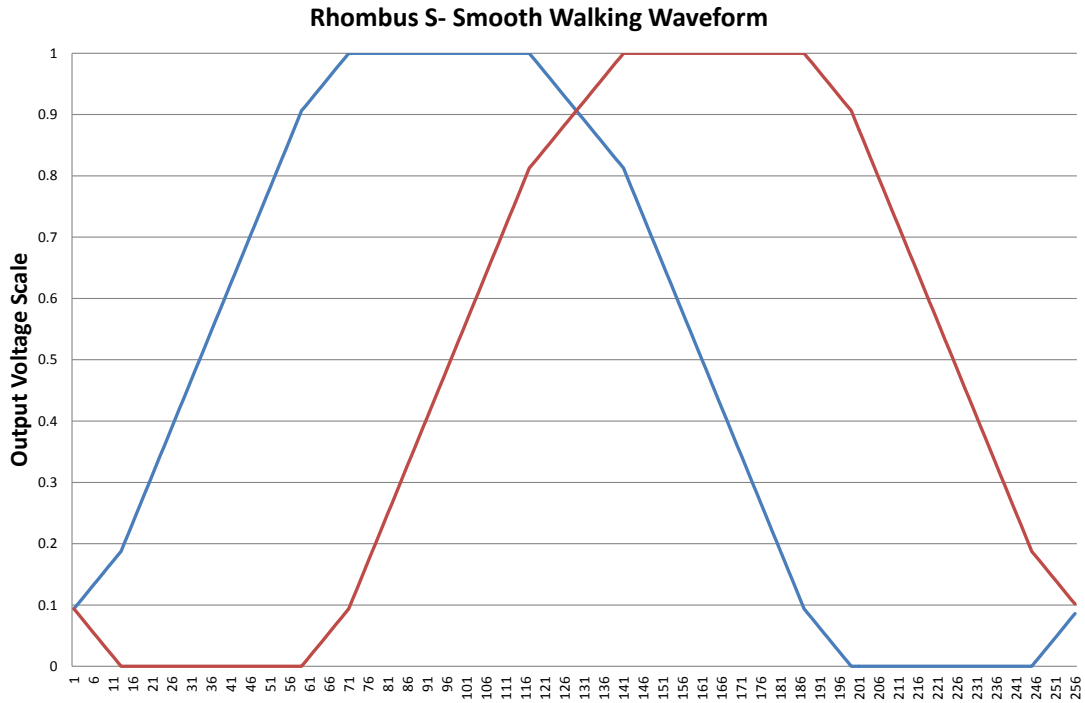


FIGURE A.1: Rhombus S shaped waveform optimized for speed.

and up to 12 kHz, though the results of which were relatively unstable. Contrasted with harmonic actuators, quasistatic actuators are often driven with waveforms with complicated shapes, designed to optimize certain aspects of motor operation such as speed, force, or noise. All of the following waveforms are expressed in this system as 2,012 point, 12 bit waveforms.

A.2 Harmonic Actuators

In contrast to quasistatic actuators, most harmonic PZAs use only two phased sinusoidal driving wave forms and a ground, as can be seen in Fig. A.5. Though these motors use similar driving signals, control of the motors is executed in very different manners.

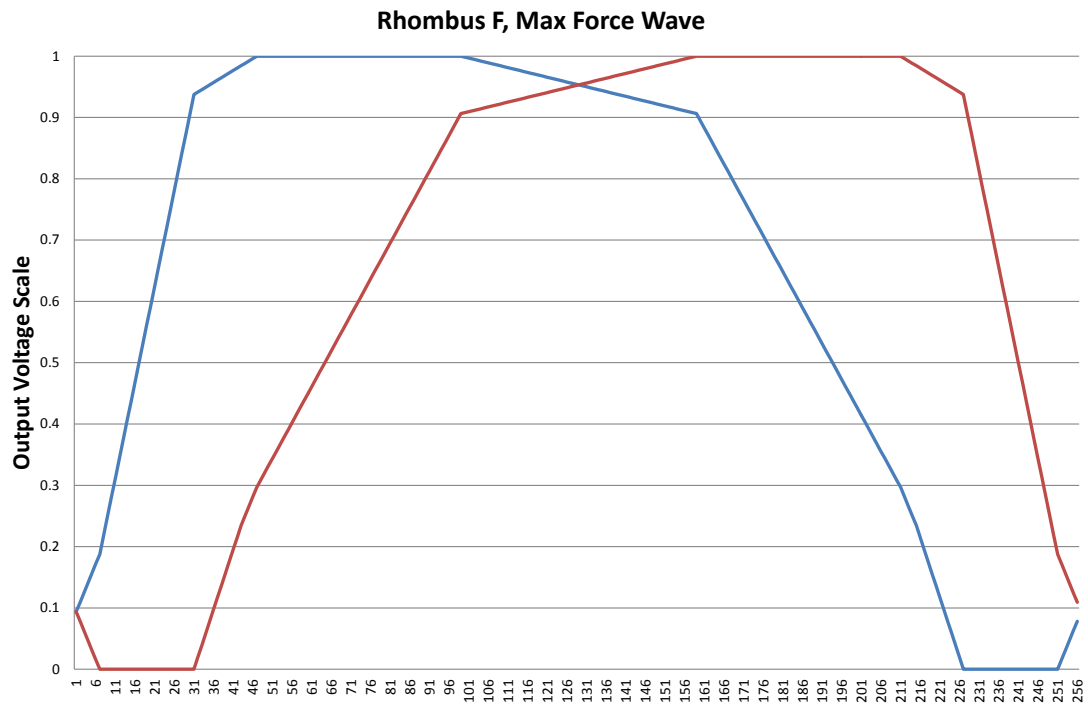


FIGURE A.2: Waveform optimized to generate maximum force, though requires complicated driving circuitry. This is the most commonly utilized waveform for high performance applications.

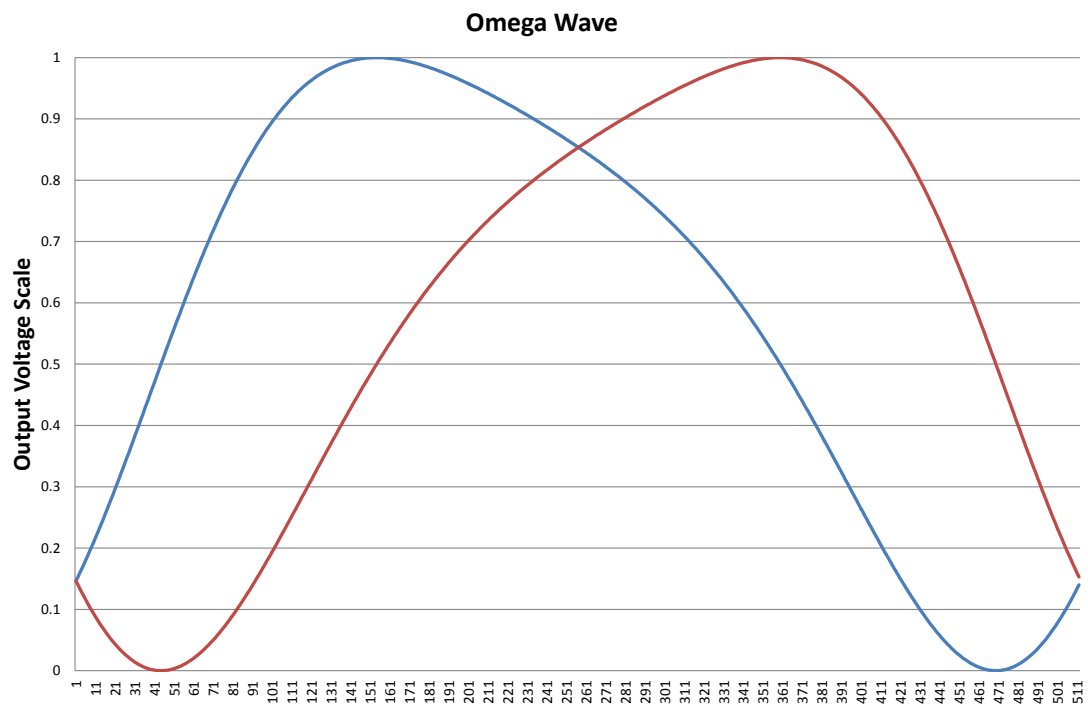


FIGURE A.3: Waveform optimized for smooth walking. Note the rounded corners on the wave making it inherently more suitable for use in an MRI environment due to the lower frequency components.

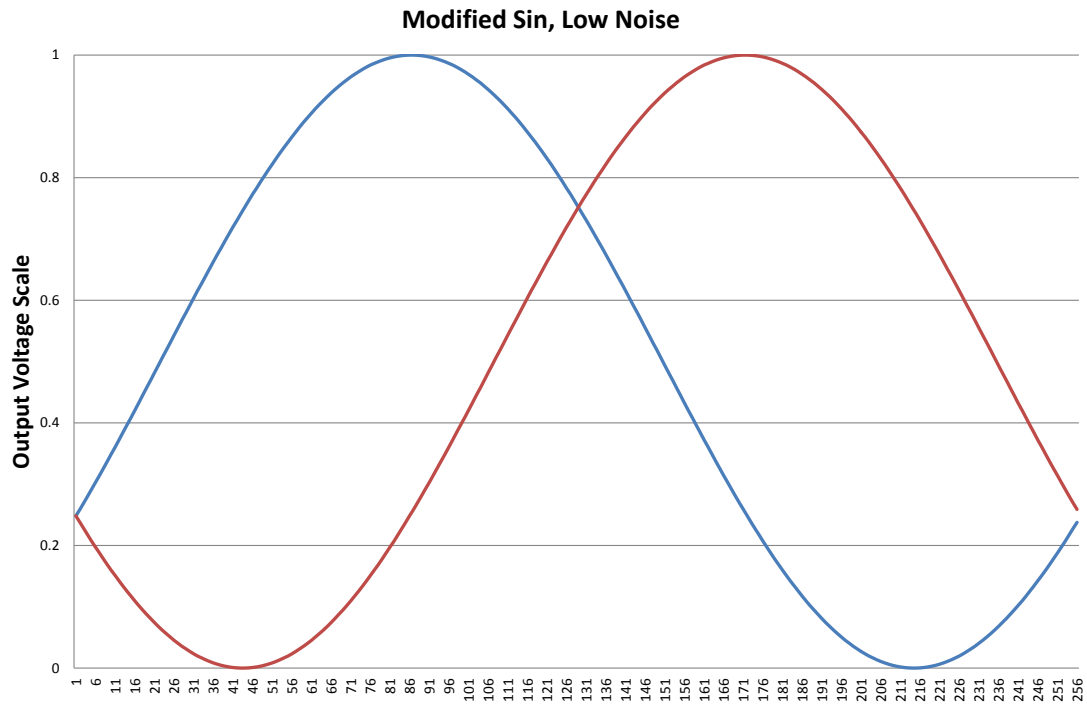


FIGURE A.4: Modified sine wave driving signal for operating PiezoLEGS actuators with low noise. The frequency range and structure of the motor makes it produce a loud shrill noise when under operation and this modified sine wave reduces that noise.

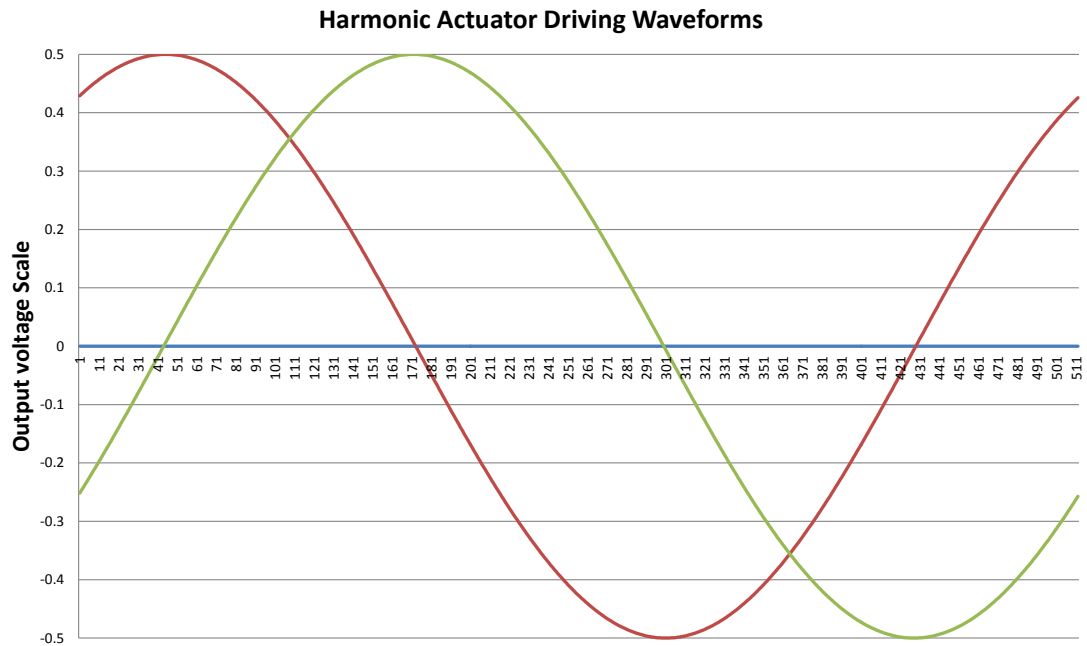


FIGURE A.5: Driving waveforms for most harmonic actuators, though control is executed in various manners.

Bibliography

- [1] A. Krieger, S.-E. Song, N. B. Cho, I. Iordachita, P. Guion, G. Fitchinger, and L. L. Whitcomb, “Development and evaluation of an actuated MRI-compatible robotic system for MRI-guided prostate intervention,” *International Conference on Robotics and Automation*, vol. 16, pp. 1066–1073, 2010.
- [2] G. Fischer, I. Iordachita, C. Csoma, J. Tokuda, S. DiMaio, C. Tempany, N. Hata, and G. Fitchinger, “MRI-compatible pneumatic robot for transperineal prostate needle placement,” *Transactions on Mechatronics*, vol. 13, pp. 295–305, 2008.
- [3] J. Tokuda, G. S. Fischer, C. Csoma, S. P. DiMaio, D. G. Gobbi, G. Fichtinger, C. M. Tempany, and N. Hata, “Software strategy for robotic transperineal prostate therapy in closed-bore MRI,” *International Conference on Medical Image Computing and Computer Assisted Intervention*, vol. 11, pp. 701–709, Sept. 2008.
- [4] J. Tokuda, G. S. Fischer, S. P. DiMaio, D. G. Gobbi, C. Csoma, P. W. Mewes, G. Fichtinger, C. M. Tempany, and N. Hata, “Integrated navigation and control software system for MRI-guided robotic prostate interventions,” *Computerized Medical Imaging and Graphics*, vol. 34, no. 1, pp. 3 – 8, 2010.

- [5] H. Su, W. Shang, K. Harrington, A. Camilo, G. Cole, J. Tokuda, N. Hata, C. Tempany, and G. S. Fischer, “A networked modular hardware and software system for MRI-guided robotic prostate interventions,” in *SPIE*, pp. 83161Z–83161Z–8, 2012.
- [6] W. Shang and G. S. Fischer, “A high accuracy multi-image registration method for tracking MRI-guided robots,” in *SPIE Medical Imaging*, February 2012.
- [7] A. Hinsche and R. Smith, “Image-guided surgery,” *Current Orthopaedics*, vol. 15, no. 4, pp. 296 – 303, 2001.
- [8] V. Horsley and R. Clarke, “The structure and functions of the cerebellum examined by a new method,” *Brain*, vol. 31, pp. 45–124, 1908.
- [9] P. Ross, H. Ashamalla, and S. Rafla, “Advances in stereotactic radiosurgery and stereotactic radiation therapy,” *Radiation Therapist*, vol. 20, no. 1, pp. 57–72, 2011.
- [10] H. Elhawary, Z. Tse, A. Hamed, M. Rea, and B. D. M. Lamperth, “The case for MR-compatible robotics: a review of the state of the art,” *The International Journal of Medical robotics and Computer Assisted Surgery*, vol. 4, pp. 105–113, 2008.
- [11] R. Gassert, E. Burdet, and K. Chinzei, “Opportunities and challenges in MR-compatible robotics,” *Engineering in Medicine and Biology*, vol. 3, pp. 15–22, 2008.
- [12] K. Masamune, E. Kobayashi, Y. Masutani, M. Suzuki, T. Dohi, H. Iseki, and K. Takakura, “Development of an MRI-compatible needle insertion manipulator for stereotactic neurosurgery,” *J Image Guid Surg*, vol. 1, no. 4, pp. 242–248, 1995.

- [13] K. Chinzei, N. Hata, F. A. Jolesz, and R. Kikinis, “Surgical assist robot for the active navigation in the intraoperative MRI: hardware design issues,” in *Proc. IEEE/RSJ Int. Conf. Intelligent Robots and Systems (IROS 2000)*, vol. 1, pp. 727–732, 2000.
- [14] N. Tsekos, A. Khanicheh, E. Christoforou, and C. Mavroidis, “Magnetic resonance-compatible robotic and mechatronics systems for image-guided interventions and rehabilitation: A review study,” *Annual Review of Biomedical Engineering*, vol. 9, pp. 351–387, 2007.
- [15] D. Stoianovici, D. Song, D. Petrisor, D. Ursu, D. Mazilu, M. Muntener, M. Mutener, M. Schar, and A. Patriciu, “MRI stealth robot for prostate interventions,” *Minim Invasive Ther Allied Technol*, vol. 16, no. 4, pp. 241–248, 2007.
- [16] A. Krieger, I. Iordachita, S.-E. Song, N. Cho, P. Guion, G. Fichtinger, and L. Whitcomb, “Development and preliminary evaluation of an actuated MRI-compatible robotic device for MRI-guided prostate intervention,” in *Robotics and Automation (ICRA), 2010 IEEE International Conference on*, pp. 1066–1073, May 2010.
- [17] F. Carpi, A. Khanicheh, C. Mavroidis, and D. De Rossi, “MRI compatibility of silicone-made contractile dielectric elastomer actuators,” *Mechatronics, IEEE/ASME Transactions on*, vol. 13, pp. 370–374, june 2008.
- [18] R. Gassert, R. Moser, E. Burdet, and H. Bleuler, “MRI/fMRI-compatible robotic system with force feedback for interaction with human motion,” *IEEE Trans Mech*, vol. 11, pp. 216–224, April 2006.

- [19] Y. Kwoh, J. Hou, E. Jonckheere, and S. Hayati, "A robot with improved absolute positioning accuracy for CT guided stereotactic brain surgery," *IEEE J BME*, vol. 35, no. 2, pp. 153–160, 1988.
- [20] A. Feldon, J. Vagner, A. Hinz, H. Fisher, S. Pfeiderer, J. R. Reichenback, and W. Kaiser, "ROBITOM-robot for biopsy and therapy of the mamma," *Biomedical Technology*, vol. 47, pp. 2–5, 2002.
- [21] E. Hemple, H. Fischer, L. Gumb, T. Hohn, H. Krause, U. Voges, H. Breitwieser, B. Gutmann, J. Durke, M. Bock, and A. Melzer, "An MRI-compatible surgical robot for precise radiological interventions," *Computer Assisted Surgery*, vol. 8, pp. 180–191, 2003.
- [22] D. Stoianovici, L. Whitcomb, J. Anderson, R. Taylor, and L. Kavoussi, "A modular surgical robotic system for image guided percutaneous procedures," *International Conference on Medical Image Computing and Computer Assisted Intervention*, vol. 1496, pp. 404–410, 1998.
- [23] K. Chinzei and K. Miller, "MRI guided surgical robot," in *Australian Conference on Robotics and Automation*, pp. 50–55, 2001.
- [24] S. DimAio, S. Pieper, K. Chinzei, N. Hata, S. Haker, D. Kacher, G. Fitchinger, C. Tempny, and R. Kikinis, "Robot-assisted percutaneous intervention in open-MRI," *Computer Aid*, vol. 1, pp. 15–24, 2007.
- [25] A. Krieger, I. Iordachita, P. Guion, A. Singh, A. Kaushal, C. Menard, P. Pinto, K. Camphausen, G. Fitchinger, and

- L. Whitcomb, "An MRI-compatible robotic system with hybrid tracking for MRI-guided prostate intervention," *Transactions on Biomedical Engineering*, vol. 58, pp. 3049–3061, 2011.
- [26] D. Beyersdorff, A. Winkel, B. Hamm, S. Lenk, S. Loening, and M. Taupitz, "MR imaging-guided prostate biopsy with a closed MR unit at 1.5 t: Initial results," *Radiology*, vol. 234, pp. 576–581, 2005.
- [27] S.-E. Song, N. B. Cho, G. Fischer, N. Hata, C. Tempany, G. Fitchinger, and I. Iordachita, "Development of a pneumatic robot for MRI-guided transperineal prostate biopsy and brachytherapy: New approaches," *IEEE International Conference on Robotics and Automation*, vol. 2010, pp. 2580–2586, 2010.
- [28] H. Su, M. Zervas, G. Cole, C. Furlong, and G. Fischer, "Real-time MRI-guided needle placement robot with integrated fiber optic force sensing," in *IEEE ICRA 2011 International Conference on Robotics and Automation, Shanghai, China*, pp. 1583–1588, 2011.
- [29] H. Su, D. Cardona, W. Shang, A. Camilo, G. Cole, D. Rucker, R. Webster, and G. Fischer, "A MRI-guided concentric tube continuum robot with piezoelectric actuation: A feasibility study," in *Robotics and Automation (ICRA), 2012 IEEE International Conference on*, pp. 1939–1945, may 2012.
- [30] H. Su, W. Shang, G. Cole, K. Harrington, and G. Fischer, "Haptic system design for MRI-guided needle based prostate brachytherapy," in *Haptics Symposium, IEEE*, pp. 483–488, 2010.

- [31] R. Kokes, K. Lister, R. Gullapalli, B. Zhang, A. MacMillan, H. Richard, and J. Desai, "Towards a teleoperated needle driver robot with haptic feedback for RFA of breast tumors under continuous MRI," *Medical Image Analysis*, vol. 13, pp. 445–455, 2009.
- [32] G. S. Fischer, A. Krieger, I. I. Iordachita, C. Csoma, L. L. Whitcomb, and G. Fichtinger, "MRI compatibility of robot actuation techniques – a comparative study," *Int Conf Med Image Comput Comput Assist Interv*, Sept. 2008.
- [33] D. Stoianovici, A. Patriciu, D. Petrisor, D. Mazilu, and L. Kavoussi, "A new type of motor: Pneumatic step motor," *Transactions on Mechatronics*, vol. 12, pp. 98–107, February 2007.
- [34] H. Elhawary, A. Zivanovic, M. Rea, Z. T. H. Tse, D. McRobbie, I. Young, M. Paley, B. Davies, and M. Lamprth, "A MR compatible mechatronic system to facilitate magic angle experiments in vivo.," *Med Image Comput Comput Assist Interv Int Conf Med Image Comput Comput Assist Interv*, vol. 10, no. Pt 2, pp. 604–611, 2007.
- [35] T. Suzuki, H. Liao, E. Kobayashi, and I. Sakuma, "Ultrasonic motor driving method for EMI-free image in MR image-guided surgical robotic systems," in *International Conference on Intelligent Robotic Systems*, 2007.
- [36] E. Taillant, J.-C. A. Vilchis, C. Allegrini, I. Bricault, and P. Cinquin, "CT and MR compatible light puncture robot: Architectural design and first experiments," in *International Conference on Medical Image Computing and Computer Assisted Intervention*, 2004.

- [37] A. Melzer, B. Gutmann, T. Remmele, R. Wolf, A. Lukoscheck, M. Bock, H. Bardenheuer, and H. Fischer, “Innomotion for percutaneous image-guided interventions,” *Engineering in Medicine and Biology Magazine, IEEE*, vol. 27, pp. 66–73, may-june 2008.
- [38] R. Gassert, R. Moser, E. Burdet, and H. Bleuler, “MRI/fMRI-compatible robotic system with force feedback for interaction with human motion,” *Transactions on Mechatronics*, vol. 11, pp. 216–224, 2006.
- [39] G. Ganesh, R. Gassert, E. Burdet, and H. Bleuler, “Dynamics and control of an MRI compatible master-slave system with hydrostatic transmission,” in *Proc. IEEE International Conference on Robotics and Automation ICRA '04*, vol. 2, pp. 1288–1294, Apr 26–May 1, 2004.
- [40] N. Yu, C. Hollnagel, A. Blickenstorfer, S. S. Kollias, , and R. Riener, “Comparison of MRI-compatible mechatronic systems with hydrodynamic and pneumatic actuation,” *Transactions on Mechatronics*, vol. 13, pp. 268–277, 2008.
- [41] P. Vartholomeos, M. Fruchard, A. Ferreira, and C. Mavroidis, “MRI-guided nanorobotic systems for therapeutic and diagnostic applications,” *Annual Review of Biomedical Engineering*, vol. 13, pp. 157–184, 2011.
- [42] M. Ho, A. McMillan, M. Simard, R. Gullapalli, and J. Desai, “Toward a meso-scale SMA-actuated MRI-compatible neurosurgical robot,” *Transactions on Robotics*, vol. 28, pp. 213–222, 2012.

- [43] R. Gassert, E. Burdet, and K. Chinzei, “MRI-compatible robotics: A critical tool for image-guided interventions, clinical diagnostics, and neuroscience,” *Engineering in Medicine and Biology Magazine*, vol. May/June 2008, pp. 12–15, 2008.
- [44] N. Nathoo, C. Cavusoglu, M. Vogelbaum, and G. Barnett, “In touch with robotics: Neurosurgery for the future,” *Neurosurgery*, vol. 56, pp. 421–435, 2005.
- [45] T. Haidegger, L. Kovacs, G. Fordos, Z. Benyo, and P. Kazantzides, “Future trends in robotic neurosurgery,” in *NordicBaltic Conference on Biomedical Engineering and Medical Physics*, no. 2, pp. 229–233, 2008.
- [46] R. Tasker, “One man’s recollection of 50 years of functional and stereotactic neurosurgery,” *Neurosurgery*, vol. 55, pp. 968–976, 2004.
- [47] W. Hall and C. Truwit, “Intraoperative magnetic resonance imaging,” *Acta Neurochirurgica Supplementum*, vol. 109, pp. 119–129, 2011.
- [48] T. Hartkens, D. Hill, A. Castellano-Smith, D. Hawkes, C. Maurer, A. Martin, H. Liu, and C. Truwit, “Measurement and analysis of brain deformation during neurosurgery,” *Transactions on Medical Imaging*, vol. 22, pp. 82–92, 2003.
- [49] A. Franzini, M. Marchetti, L. Brait, I. Milanesi, G. Messina, E. Forapani, G. Broggi, and L. Fariselli, “Deep brain stimulation and frameless stereotactic radiosurgery in the treatment of bilateral parkinsonian tremor: target selection and case report of two patients,” *Acta Neurochir*, vol. 153, pp. 1069–1075, 2011.

- [50] A. Franzini, R. Cordella, G. Messina, C. E. Marras, L. M. Romito, F. Carella, A. Albanese, M. Rizzi, N. Nardocci, G. Zorzi, E. Zekay, and G. Broggi, “Deep brain stimulation for movement disorders. considerations on 276 consecutive patient,” *Journal of Neural Transmission*, vol. 10, pp. 1497–1510, 2011.
- [51] C. Truwit, A. J. Martin, and W. A. Hall, “MRI guidance of minimally invasive cranial applications,” in *Interventional Magnetic Resonance Imaging* (T. Kahn and H. Busse, eds.), Medical Radiology, pp. 97–112, Springer Berlin Heidelberg, 2012. 10.1007/1742011446.
- [52] M. Hadani, R. Spiegelman, Z. Feldman, H. Berkenstadt, and Z. Ram, “Novel, compact, intraoperative magnetic resonance imaging-guided system for conventional neurosurgical operating rooms,” *Neurosurgery*, vol. 48, pp. 799–809, 2001.
- [53] Bennett, L. H. Wang, P. S. Donahue, and M. J., “Artifacts in magnetic resonance imaging from metals,” *Journal of Applied Physics*, vol. 79:8, pp. 4712–4714, 1996.
- [54] K. Chinzei, R. Kikinis, , and F. A. Jolesz, “MR compatibility of mechatronic devices: Design criteria,” in *MICCAI 1999*, 1999.
- [55] G. S. Fischer, *Enabling Technologies for MRI Guided Interventional Procedures*. PhD thesis, Johns Hopkins University, Baltimore, Maryland, July 2008.
- [56] H. Su, I. Iordachita, X. Yan, G. Cole, and G. Fischer, “Re-configurable MRI-guided robotic surgical manipulator: Prostate brachytherapy and neurosurgery applications,” in *Engineering*

- in Medicine and Biology Society, EMBC, 2011 Annual International Conference of the IEEE*, pp. 2111–2114, 30 2011-sept. 3 2011.
- [57] D. B. Comber, D. Cardona, R. J. Webster III, and E. J. Barth, “Sliding mode control of an mri-compatible pneumatically actuated robot,” *ASME Journal of Medical Devices*.
- [58] G. Bone and S. Ning, “Experimental comparison of position tracking control algorithms for pneumatic cylinder actuators,” *IEEE/ASME Transactions on Mechatronics*, vol. 12, pp. 557–561, Oct. 2007.
- [59] T. Acarman, C. Hatipoglu, and U. Ozguner, “A robust nonlinear controller design for a pneumatic actuator,” in *Proc. American Control Conference the 2001*, vol. 6, pp. 4490–4495 vol.6, 2001.
- [60] Y. Wang, H. Su, K. Harrington, and G. Fischer, “Sliding mode control of piezoelectric valve regulated pneumatic actuator for MRI-compatible robotic intervention,” in *ASME Dynamic Systems and Control Conference - DSCC 2010*, (Cambridge, Massachusetts, USA), 2010.
- [61] G. R. Sutherland, I. Latour, A. D. Greer, T. Fielding, G. Feil, and P. Newhook, “An image-guided magnetic resonance-compatible surgical robot.,” *Neurosurgery*, vol. 62, pp. 286–92; discussion 292–3, Feb 2008.
- [62] G. Fischer, J. Iordachita, S. DiMaio, and G. Fichtinger, “Design of a robot for transperineal prostate needle placement in MRI scanner,” in *Proc. IEEE International Conference on Mechatronics*, pp. 592–597, July 2006.

- [63] G. S. Fischer, S. P. DiMaio, I. I. Iordachita, and G. Fichtinger, “Robotic assistant for transperineal prostate interventions in 3t closed MRI,” *Int Conf Med Image Comput Comput Assist Interv*, vol. 10, no. Pt 1, pp. 425–433, 2007.
- [64] J. Tokuda and G. Fischer, “OpenIGTLink: an open network protocol for image-guided therapy environment,” *Int J Med Robot*, vol. 5, pp. 423–34, Dec. 2009.
- [65] G. Fischer, I. Iordachita, C. Csoma, J. Tokuda, S. DiMaio, C. Tempany, N. Hata, and G. Fichtinger, “MRI-compatible pneumatic robot for transperineal prostate needle placement,” *Mechatronics, IEEE/ASME Transactions on*, vol. 13, pp. 295–305, June 2008.
- [66] Y. Wang, M. Shazeeb, C. Sotak, and G. S. Fischer, “Optimization of piezoelectric motors to enhance MR compatibility for interventional devices,” in *International Society for Magnetic Resonance in Medicine, 17th Scientific Meeting and Exhibition, Proceedings*, 2009.
- [67] Y. Wang, G. Cole, H. Su, J. Pilitsis, and G. Fischer, “MRI compatibility evaluation of a piezoelectric actuator system for a neural interventional robot,” in *Engineering in Medicine and Biology Society Annual International Conference*, pp. 6072–6075, IEEE, 2009.
- [68] R. Kokes, K. Lister, R. Gullapalli, B. Zhang, A. MacMillan, H. Richard, and J. Desai, “Towards a teleoperated needle driver robot with haptic feedback for RFA of breast tumors under continuous MRI,” *Medical Image Analysis*, vol. 13, no. 3, pp. 445 – 55, 2009.

- [69] S. Mahmoud, *Electromagnetic Waveguides, Theories and Applications*. Peter Peregrinus Ltd., London, United Kingdom, 1991.
- [70] C. Westbrook, C. K. Roth, and J. Talbot, *MRI in Practice*, vol. 4. Wiley-Blackwell, 2011.
- [71] A. M. Blamire, “The technology of MRI - the next 10 years?,” *The British Journal of Radiology*, vol. 81, pp. 601–617, 2008.
- [72] A. Dumais, “Digital power improves power-supply efficiency,” August 2009.
- [73] N. E. M. A., “Determination of signal-to-noise ration (SNR) in diagnostic magnetic resonance imaging,” tech. rep., National Electrical Manufacturers Association, 2008.
- [74] H. Su, A. Camilo, G. Cole, N. Hata, C. Tempany, and G. Fischer, “High-field MRI compatible needle placement robot for prostate interventions,” in *Proceedings of MMVR18 (Medicine Meets Virtual Reality)*, (Newport Beach, California, USA), February 2011.
- [75] H. Su, G. A. Cole, and G. S. Fischer, “High-field MRI-compatible needle placement robots for prostate interventions: Pneumatic and piezoelectric approaches,” in *Advances in Robotics and Virtual Reality* (T. Gulrez and A. E. Hassanien, eds.), vol. 26 of *Intelligent Systems Reference Library*, pp. 3–32, Springer Berlin Heidelberg, 2012.
- [76] H. Su, K. Harrington, G. Cole, Y. Wang, and G. Fischer, “Modular needle steering driver for MRI-guided transperineal prostate intervention,” in *IEEE International Conference on Robotics and Automation, Workshop on Snakes, Worms and*

- Catheters: Continuum and Serpentine Robots for Minimally Invasive Surgery*, (Anchorage, AK, USA), May 2010.
- [77] K. Uchino, “Piezoelectric ultrasonic motors: overview,” *Smart Materials and Structures*, vol. 7, no. 3, p. 273, 1998.
- [78] J.-F. Collard, C. Vloebergh, B. Dehez, and P. Fisette, “Multi-body modelling of a travelling wave linear piezomotor,” in *Multi-body Dynamics 2009* (W. Arczewski, Fraczek, ed.), (Warsaw Poland), ECCOMAS, June-July 2009.
- [79] M. Goldfarb and N. Celanovic, “Modeling piezoelectric stack actuators for control of micromanipulation,” in *International Conference of Robotics and Automation*, pp. 69–80, IEEE, IEEE, April 1996.
- [80] K. Spanner, “Surve of the various operating principles of ultrasonic piezomotors,” in *ACTUATOR 2006*, 2006.
- [81] F. Szufnarowski and A. Schneider, “Force control of a piezoelectric actuator based on a statistical system model and dynamic compensation,” *Mechanism and Machine Theory*, vol. 46, pp. 1507–1521, May 2011.
- [82] F. Szufnarowski and A. Schneider, “Two-dimensional dynamics of a quasi-static legged piezoelectric actuator,” *Smart Materials and Structures*, vol. 21, no. 5, p. 055007, 2012.
- [83] R. Merry, M. Uyanik, R. van de Molengraft, M. Steinbuch, R. Koops, and M. van Veghel, “Modeling and compensation of asymmetric hysteresis in a piezo actuated metrological AFM,” in *American Control Conference, 2009. ACC '09.*, pp. 967–972, june 2009.

- [84] R. J. E. Merry, *Performance-driven control of nano-motion systems*. Dissertation, Technische Universiteit Eindhoven, November 2009.
- [85] Z. Tse, H. Elhawary, M. Rea, I. Young, B. Davis, and M. Lamperth, “A haptic unit designed for magnetic-resonance-guided biopsy,” *Proceedings of the Institution of Mechanical Engineers, Part H (Journal of Engineering in Medicine)*, vol. 223, no. H2, pp. 159 – 72, 2009.
- [86] M. Arafa, O. Aldraihem, and A. Baz, “Modeling and characterization of a linear piezomotor,” *Journal of Intelligent Material Systems and Structures*, vol. 20, pp. 1913–1922, November 2009.
- [87] P. corporation, *Piezo LEGS Linear 6N*. Piezomotor Corporation, Uppsala Sweden.
- [88] A. Velten, E. Lawson, A. Bardagjy, M. Bawendi, and R. Raskar, “Slow art with a trillion frames per second camera,” in *ACM SIGGRAPH 2011 Posters*, SIGGRAPH ’11, (New York, NY, USA), pp. 13:1–13:1, ACM, 2011.
- [89] G. Cole, K. Harrington, H. Su, A. Camilo, J. Pilitsis, and G. Fischer, “Closed-loop actuated surgical system utilizing real-time in-situ MRI guidance,” in *12th International Symposium on Experimental Robotics - ISER 2010*, (New Delhi and Agra, India), 2010.
- [90] P. Starr, A. Martin, J. Ostrem, P. Talke, N. Levesque, and P. Larson, “Subthalamic nucleus deep brain stimulator placement using high-field interventional magnetic resonance imaging and a skull-mounted aiming device: technique and application accuracy,” *Journal of Neurosurgery*, vol. 112, pp. 479–490, 2010.

- [91] S. M. III, B. Ford, P. Senatus, L. Winfield, Y. Du, S. Pullman, Q. Yu, S. Frucht, G. McKhann, and R. Goodman, "Subthalamic stimulation for parkinson disease: determination of electrode location necessary for clinical efficacy," *Neurosurg Focus*, vol. 19, 2005.
- [92] R. Taylor, J. Funda, B. Eldridge, S. Gomory, K. Gruben, D. LaRose, M. Talamini, L. Kavoussi, and J. Anderson, "A telerobotic assistant for laparoscopic surgery," *IEEE Engineering in Medicine and Biology*, vol. 14, no. 3, pp. 279–288, 1995.
- [93] P. Ferroli, A. Franzini, C. Marras, E. Maccagnano, L. D'Incerti, and G. Broggi, "A simple method to assess accuracy of deep brain stimulation electrode placement: Pre-operative stereotactic CT + postoperative MR image fusion," *Stereotactic and Functional Neurosurgery*, vol. 82, pp. 14–19, 2004.
- [94] R. H. Taylor, P. Jensen, L. L. Whitcomb, A. Barnes, R. Kumar, D. Stoianovici, P. Gupta, Z. Wang, E. Dejuan, and L. Kavoussi, "A steady-hand robotic system for microsurgical augmentation," *The International Journal of Robotics Research*, vol. 18, no. 12, pp. 1201–1210, 1999.
- [95] Y. Ma, I. Dobrev, W. Shang, H. Su, S. R. Janga, and G. S. Fischer, "Chic: Cylindrical helix imaging coordinate registration fiducial for mri-guided interventions," in *Engineering in Medicine and Biology Society (EMBC), 2012 Annual International Conference of the IEEE*, pp. 2808–2812, IEEE, 2012.
- [96] G. R. Sutherland, P. B. McBeth, and D. F. Louw, "Neuroarm: an MR compatible robot for microsurgery," *International Congress Series*, vol. 1256, no. 0, pp. 504 – 508, 2003.

-
- [97] F. Wu, “Multi-probe robotic poposition for cryoablation in mri,” Master’s thesis, Massachusetts Institute of Technology, 2012.

Gregory Cole

25 Grace Lane ♦ Ossining, NY 10562 ♦ (508) 410-9450 ♦ greg.colerobotics@gmail.com

PROFESSIONAL EXPERIENCE

Philips Research North America, Member of Research Staff (2012 –present)

Work with a small team to construct, test and expand upon novel interventional devices. Research includes mechanical analysis, industrial design for manufacturing, ease-of-use, integration of diagnostic and therapeutic devices and pre-clinical testing.

Automation and Interventional Medicine Laboratory, Worcester Polytechnic Institute, Worcester, MA 2008 – Present
[Founded in 1865, WPI is one of the nation's first engineering and technology universities. The AIM laboratory focuses on the research of medical robotics to guide surgical procedures.]

George I. Alden Fellow / Research Assistant (2009 – 2012)

Work collaboratively with numerous members of laboratory team involved in the research and development of medical robotics. Participate in managing the daily operations of lab as well as ongoing research projects and experiments. Manage the manufacturing pipeline, which includes PCB printing and assembly, sheet metal fabrication, and purchasing. Supervise and mentor 2 staff engineers and grad students.

- Developed modular MRI compatible surgical system, which is the lab's core technology.
- Designed comprehensive modular system from concept to manufacturing publication.
- Worked with legal counsel to write patent applications for a robotic stereotactic neural intervention system.

Laboratory Manager (2008 – 2009)

Selected by AIM lab professor to build the AIM research lab, which involved purchasing lab equipment and lab furniture and designing layout of lab. Conducted cutting-edge research, led multiple projects, and managed the daily lab operations.

- Manufactured several devices to support research operations, including power supplies, equipment carriers, MRI test equipment, circuits, and linkages for investigation into mapping non-robotic surgical procedures to robotic procedures.
- Contributed to the development and manufacture of a cooling system for a laser cutter as well as various pieces of equipment used for introduction to robotics courses.

Neuron Robotics, LLC, Somerville, MA

2009 – 2010

[Start-up company that designs hardware and software for robotics projects and teaching tools for educators to implement their own robotics and engineering courses.]

Vice President

Hired to design packaging and housings for company's electronics and serve as the organization's mechanical engineer. Built business relationships and negotiated production pipeline for initial run of company's first product.

- Aided in negotiation of company's first contract worth \$50,000.

Johns Hopkins University, Baltimore, MD

2010

Visiting Student

Conducted research in the development of a new type of actuation system for a miniature medical device.

EDUCATION & PROFESSIONAL DEVELOPMENT

Worcester Polytechnic Institute, Worcester, MA

Fall 2012

Ph.D., Robotics Engineering, 3.78 G.P.A.

Worcester Polytechnic Institute, Worcester, MA

2009

M.S., Mechanical Engineering, 3.86 G.P.A.

Worcester Polytechnic Institute, Worcester, MA

2009

B.S., Mechanical Engineering, Graduated with Honors, 3.63 G.P.A.

Certified in FDA Regulatory Practices

OSHA 10-hour Safety Program

Continued...

AFFILIATIONS

Institute of Electrical and Electronics Engineers
American Society of Mechanical Engineers
American Institute of Aeronautics and Astronautics
Rho Beta Epsilon Robotics Honors Society
Sigma Xi, Scientific Honors Society

AWARDS & RECOGNITION

NSF Grassroots Fellowship (for travel during ICRA Conference), 2010
Graduate Research Appreciation Day Competition, First Place (for Neurosurgery Robot), 2010
First Place (for Modular MRI Compatible Surgical System), Innovation Presentation Competition, 2010
Judges Award, Robotics Innovation Competition and Conference, 2010
One of 2 George I. Alden Fellowship Recipients, Worcester Polytechnic Institute (One-year Salary and 20 Credits of Tuition in Recognition of Excellence), 2010
Second Place (for Neurosurgery Robot), Graduate Research Appreciation Day Competition, 2009
First Place (for Project Scimitar), Electronic Product Development Competition, 2007

TECHNICAL SUMMARY

Electronic Development: Analogue Circuit Design, DC-DC Converter Design, Amplifier and Signal Generator Design, Digital Circuit Design, PCB Layout, 2-6 layer Altium Designer, Eagle Cad, NI Multisim, LT Spice, Design for Manufacture, Production Pipelining (Set up overseas production for Neuron Robotics Diyo, and local Manufacturing for AIM Labs Piezo driver), and RF Shielding

Mechanical Development Software: Pro-Engineer, SolidWorks, AutoCAD, MATLAB, MathCAD, Working Model, and Norton Cam Suite

Mechanical Development Skills: Linkage Design and Analysis, Design for Manufacturability (design for CNC, rapid prototype, laser cutter), Rapid Prototyping Techniques, Thermal Analysis, Thermodynamic System Design, Fluid Mechanics, Thermal Engine Design, and Simulation

Controls Design: Kalman Filtering and PID Design

Systems Engineering: Task Specification, Kossiakoff Systems Engineering Approach, Needs Analysis, Requirements Analysis, Functional Allocation, Project Management, and Management of Technical Development Team

PUBLICATIONS

Cole, G., H. Su, G. Li, S. Weijian, K. Harrington, A. Camilo, J.G. Pilitsis, G.S. Fisher. "Robotic System for MRI-Guided Stereotactic Surgery." *Transactions on Biomedical Engineering*. February 2012.

Cole, G.A., K. Harrington, H. Su, A. Camilo, J.G. Pilitsis J.G., Fischer. "Closed-Loop Actuated Surgical System Utilizing In-Situ Real-Time MRI Guidance." (book chapter) *Springer Tracts in Advanced Robotics*, eds. Khatib, O. V. Kumar, G. Sukhatme, Springer-Verlag. 2011.

PRESENTATIONS AND CONFERENCE PAPERS

Cole, G.A. "AIM Lab Modular MRI Compatible Surgical Robotics Development Systems." WPI Robotics Engineering Colloquium Series. November 21, 2011. Worcester, MA.

Continued...

Su, H., **G.A. Cole**, N. Hatam C.M. Tempany, G.S. Fischer. "Real-time MRI-Guided Transperineal Needle Placement Prostate Interventions with Piezoelectrically Actuated Robotic Assistance," Radiological Society of North America 97th Scientific Assembly and Annual Meeting. November 2011. Chicago, IL.

Cole, G.A. "Introduction to Robotics." Worcester Polytechnic Institute. October 2011. Worcester, MA.

Fischer, G.S., **G.A. Cole**, H. Su. "Approaches to Creating and Controlling Motion in MRI." Proceedings of the 33rd Annual International Conference of the IEEE Engineering in Medicine and Biology Society. August 2011. Boston, MA.

Su, H., I. Iordachita, X. Yan, **G.A. Cole**, G.S. Fischer. "Reconfigurable MRI-Guided Robotic Surgical Manipulator: Prostate Brachytherapy and Neurosurgery Applications." Proceedings of the 33rd Annual International Conference of the IEEE Engineering in Medicine and Biology Society. August 2011. Boston, MA.

Su, H., M. Zervas M., **G.A. Cole**, C. Furlong, G.S. Fischer. "Real-time MRI-Guided Needle Placement Robot with Integrated Fiber Optic Force Sensing." IEEE ICRA 2011 International Conference on Robotics and Automation. May 2011. Shanghai, China.

Su, H., A. Camilo, **G.A. Cole**, C.M. Tempany, N. Hata, G.S. Fischer. "High-Field MRI-Compatible Needle Placement Robot for Prostate Interventions." Proceedings of Medicine Meets Virtual Reality. February 2011. Newport Beach, CA.

Cole, G., K. Harrington, H. Su, A. Camilo, J. Pilitsis, G.S. Fischer. "Closed-Loop Actuated Surgical System Utilizing Real-Time In-Situ MRI Guidance." 12th International Symposium on Experimental Robotics. December 2010. New Delhi, India.

Cole, G.A., and G.S. Fischer. "MRI Compatible Surgical Systems: Analysis of Actuator Compatibility Methodologies and System Effectiveness, Robotics Science and Systems, Workshop on Enabling Technologies for Image-Guided Interventional Procedures." June 2010.

Su, H., K. Harrington, **G.A. Cole**, Y. Wang, G.S. Fischer. "Modular Needle Steering Driver for MRI-Guided Transperineal Prostate Intervention." IEEE International Conference on Robotics and Automation, Workshop on Snakes, Worms and Catheters: Continuum and Serpentine Robots for Minimally Invasive Surgery. May 2010. Anchorage, AK.

Su, H., W. Shang, **G.A. Cole**, K. Harrington, G.S. Fischer. "Haptic System Design for MRI-Guided Needle Based Prostate Brachytherapy." Haptics Symposium - Haptics 2010. March 2010. Waltham, MA.

Su, H., W. Shang, **G.A. Cole**, K. Harrington, G.S. Fischer. "Design of a Haptic Device for MRI-Guided Prostate Needle Brachytherapy." IEEE Haptics Symposium. March 2010. Boston, MA.

Su, H., K. Harrington, **G.A. Cole**, G.S. Fischer. "Active Needle Steering for Percutaneous Prostate Intervention in High-field MRI, 2010 Robotics." Science and Systems Conference, Workshop on Enabling Technologies for Image-Guided Robotic Interventional Procedures. 2010. Zaragoza, Spain.

Wang, Y., **G.A. Cole**, H. Su, J.G. Pilitis, G.S. Fischer. "MRI Compatibility Evaluation of a Piezoelectric Actuator System for a Neural Interventional Robot." 31st Annual International Conference of the IEEE Engineering in Medicine and Biology Society. September 2009. Minneapolis, MN.

Cole, G.A. "MRI Compatible Surgical Robotic Methodologies." Johns Hopkins University Laboratories. August 2009. Baltimore, MD.

Cole, G., J. Pilitsis, G.S. Fischer. "Design of Robotic System for MRI-Guided Deep Brain Stimulation Electrode Placement." International Conference on Robotics and Automation 2009. May 2009. Kobe, Japan.

Cole, G. "MRI Compatible Stereotactic Neural Surgery Device." National Institute of Advanced Industrial Science and Technology. May 2009. Tsukuba, Japan.

Wang, Y., **Cole G.**, Su H., Fischer G. "MRI Compatibility Evaluation of a Piezoelectric Actuator System for a Neural Interventional Robot." Engineering in Medicine and Biology Conference, 2009.

Cole, G., and J. Van De Ven. "Design of a Variable Radius Piston Profile Generating Algorithm." ASME International Mechanical Engineering Congress & Exposition. 2009.

Van De Ven, J. and **G.A. Cole**. "Designs Towards a Liquid Piston Stirling Engine." International Energy Conversion Engineering Conference. 2008.